Editor

Prof. George J. Tsekouras

Image Analysis Inspired by Physical Electro-Magnetic Fields

Image Analysis Inspired by Physical Electro-Magnetic Fields

by Dr. Xiaodong Zhuang and Prof. Nikos Mastorakis

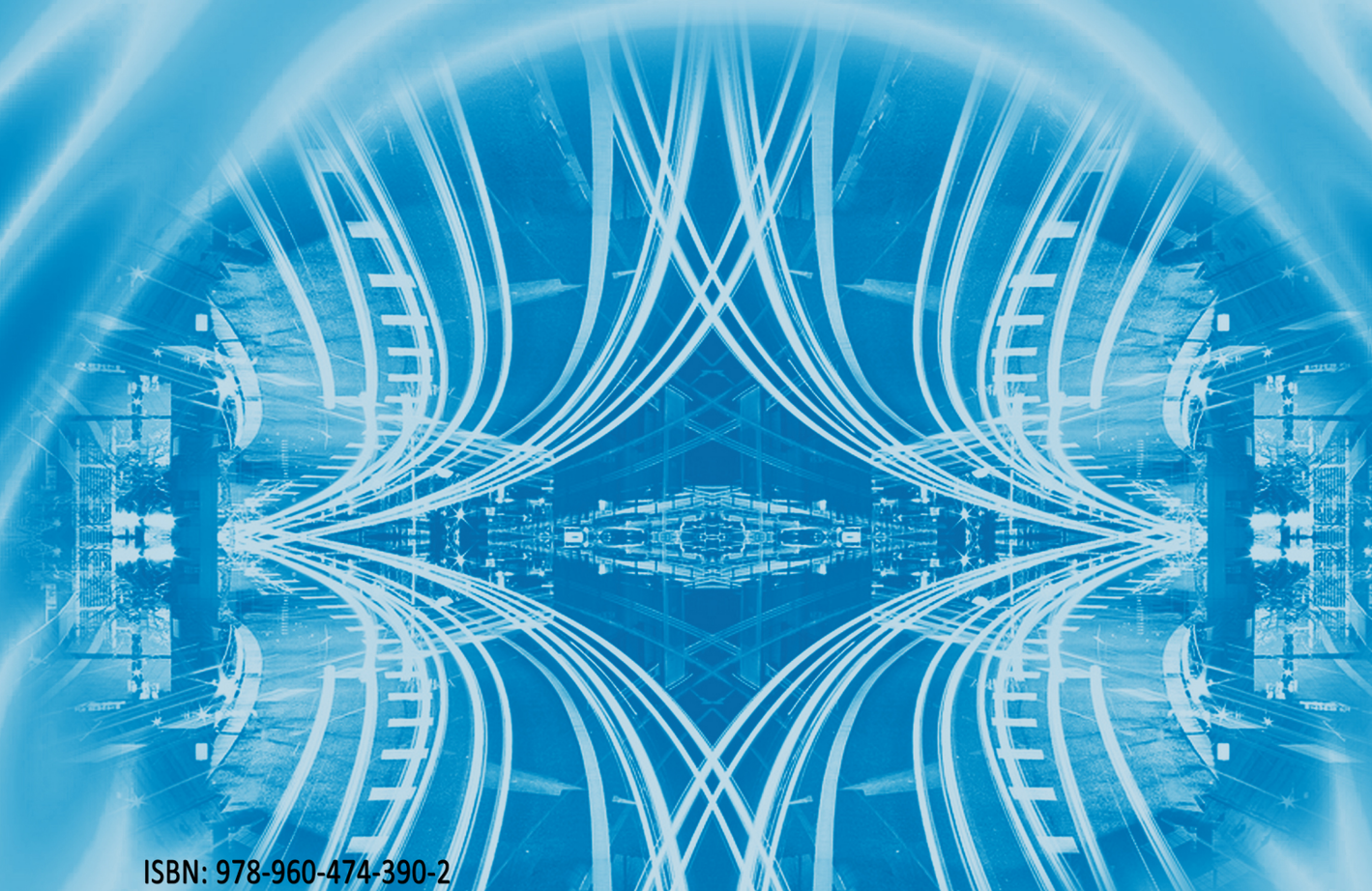

ISBN: 978-960-474-390-2

Image Analysis Inspired by Physical Electro-Magnetic Fields

Editor

Prof. George J. Tsekouras
Military Institutes of University Education (ASEI)
Hellenic Naval Academy
Terma Hatzikyriakou 18539
Piraeus, Greece

Authors

Dr. Xiaodong Zhuang
Prof. Nikos Mastorakis

Published by WSEAS Press
www.wseas.org

ISBN: 978-960-474-390-2

Image Analysis Inspired by Physical Electro-Magnetic Fields

Published by WSEAS Press
www.wseas.org

All papers of the present volume were peer reviewed by two independent reviewers. Acceptance was granted when both reviewers' recommendations were positive.
See also: http://www.worldses.org/review/index.html

ISBN: 978-960-474-390-2

World Scientific and Engineering Academy and Society

Preface

Nature has enormous power and intelligence behind its common daily appearance, and it is generous. The development of human society relies on natural resources in every area (both material and spiritual). We learn in it and from it, virtually as part of it. Nature-inspired systems and methods have a long history in human science and technology. For example, in the area of computer science, the recent well-known ones include the artificial neural network, genetic algorithm and swarm intelligence, which solve hard problems by imitating mechanisms in nature. Nature-inspired methods are also being quickly developed and applied in other areas. In this book, we just try to pick up a drop from the sea of nature's intelligence, and apply it in a specific area. We hope that it may inspire the readers' interest of nature's intelligence when exploring in their own areas of science and technology.

Traditional image processing methods usually take images as data sets or mathematical functions. In our idea of nature-inspired methods, images are more like the imitation of certain natural entities (such as electric charges, currents, etc.) simulated in computer. The evolutions of such virtual entities can be simulated according to corresponding natural laws and the simulation result can be studied for possible utilization in practical image processing tasks. Nowadays, nature-inspired methods in image processing have attracted more and more attention and research efforts. Physics and biology are the two main sources from which most of such methods have derived. Related work has achieved promising results in practical tasks, which indicate that it is a direction potentially leading to breakthroughs of new image analysis techniques. Methods inspired by physical electro-magnetic field make up a branch of this field, which have been successfully applied in the practical applications including: recognition of human ear, face and gait; extraction of corner, edge, and shape skeleton in images. The existing methods inspired by electro-magnetic theory generally belong to two categories: analysis of the virtual field generated by the image (such as the "force field transform") and deforming a shape or curve under the virtual force field generated by the image (such as the "active counter model").

The beginning of the research introduced in this book was in 2006, after we read a paper about "force field energy functionals for image feature extraction" (David J. Hurley, Mark S. Nixon, John N. Carter, 2002). This paper inspired our strong interest of natural analogies in image processing. Since then, we have been exploring in the area of nature-inspired image analysis for years and have published a series of papers about our original methods and results. These methods are mainly inspired by the theory of electro-magnetic field, which reveal the structure properties of the image by electro-magnetics inspired transforms. In these transforms, the formulas in electro-magnetic theory are adjusted to more generalized forms in order to suit practical image analysis tasks, and some novel viewpoints which take the image as a virtual field are presented. Several types of methods have been proposed from different aspects of field theory (vector field, scalar potential field, and field source distribution), which indicates that the physics inspired virtual field is a novel way of designing new effective image transforms.

Nature-inspired methodology itself means continuous exploration in the rich resource of the intelligence shown by nature. Therefore, this book does not mean the final conclusion of the authors' on-going work. Further promising results in both theory and practice are expected and we hope our research attempts shown in the book may inspire new ideas of others, which will surely be much more valuable than the book itself.

Dr. Xiaodong Zhuang
Automation & Engineering College
Qingdao University
Qingdao, 266071 China

Prof. Dr. Nikos E. Mastorakis
Technical University of Sofia, Bulgaria and
Military Institutes of University Education, Hellenic Naval Academy, Greece

Acknowledgements

The research introduced in this book is supported by WSEAS on the research topic of "Advanced Image Processing Techniques". We are sincerely grateful to the WSEAS friends for their years of warm support in our research cooperation; we would like to say that the book is the fruit of our years of cooperation research efforts. And we heartily appreciate those who helped us through hard times in research by their warm encouragement and friendly expectation to us.

The Authors

Table of Contents

1 Review

In the development of digital image processing methods, the analogy of natural systems has become an important way of inspiring new effective algorithms. Nature-inspired methodology for image processing has attracted lots of research interest and efforts. Currently, this multidisciplinary research topic covers several important science fields including physics, biology, etc. Moreover, it has gradually been forming a new branch in image processing with continuously increasing research work on it.

Nature-inspired algorithms process the image by imitating the mechanism of some nature system, in which the image is taken as part of the system and the processing result is produced by computer simulation of the system. Therefore, the advantages of many natural laws suitable for processing tasks can be exploited in such simulation, which may bring more satisfactory processing results. Physics and biology are the two main scientific fields related to nature-inspired algorithms in image processing. For example, the physical laws that have been exploited in image processing include: electro-statics, magneto-statics, gravity, water flow, heat flow, light ray propagation, fire propagation, water-filling and water shed, anisotropic diffusion, deforming structure, etc. On the other hand, the biological systems that have been imitated in image processing include: ant colony, fish school, social spider, and even bacterial foraging, bacteriorhodopsin, etc. The book first gives a literature review about the nature-inspired methodology in image processing in the following section.

1.1 Literature review

Physics-inspired methods form a main branch of nature-inspired approaches. There are considerable researchers keeping continuous work on physics-inspired methods in image processing. The group of Professor Mark S. Nixon has developed new ways to extract features based on notional use of physical paradigms, including the analogies of gravitational force, water flow and heat[1]. David J. Hurley, Mark S. Nixon and John N. Carter developed a novel force field transformation for image feature extraction in which the image is treated as an array of Gaussian attractors that act as the source of a force field[2,3,4]. The novel force field transformation and potential well extraction technique lead to a compact characteristic vector offering immunity to initialization, rotation, scale, and noise. Their method has been successfully applied in biometrics for identification. Xin U. Liu and Mark S. Nixon presented a new general framework for shape extraction based on the paradigm of water flow, which embodied the fluidity of water and hence can detect complex shapes[5,6,7,8]. The method has been applied medical image segmentation such as the detection of vessel boundaries in retinal images. Alastair H. Cummings recreated the water flow method and extending it to use two new forces - surface tension and viscosity, which was successfully applied in feature extraction[9]. Cem Direkoglu and Mark S. Nixon introduced a novel evolution-based segmentation algorithm by using the heat flow analogy, to gain practical advantage in shape extraction and image segmentation[10,11,12,13]. In Cem Direkoglu' thesis, he investigated the physical heat flow analogy both for low-level and high-level feature extraction, which was applied in moving-edge detection, shape extraction and silhouette object feature extraction. Alastair H. Cummings, Mark S. Nixon and John N. Carter presented a novel ear enrolment technique using the image ray transform, based upon an analogy to light rays[14]. Alastair H. Cummings, et al also proposed a transform using an analogy to light rays for the detection of circular and tubular features[15].

Other researchers have also proposed physics-inspired methods for image processing with various points of view. The electro-static field has attracted much attention in this direction. Andrei C. Jalba, et al proposed a physically motivated deformable model for shape recovery and segmentation[16]. The model, referred to as the charged-particle model (CPM), is inspired by classical electrodynamics and is based on a simulation of charged particles moving in an electrostatic field. Kenong Wu and Martin D. Levine proposed an approach to 3D part segmentation by simulating the electrical charge density

over the object surface and locating surface points which exhibit local charge density minima[17]. Andrei C. Jalba and Jos B. T. M. Roerdink also proposed a geometrically adaptive method for surface reconstruction from noisy and sparse point clouds based on generalized Coulomb potentials[18]. N. Ahuja and J. Chuang used a potential field model for efficient derivation of the medial axis transform of a 2D polygonal region[19]. Jen-Hi Chuang, et al also generalized the potential-based skeletonization approach for 2D medial axis transform (MAT) to three dimensions[20]. Liu Qing, et al proposed an algorithm for image resolution enhancement based on the balance principle of static electric field, where the interpolation function is adjusted automatically by the electrical potential differences of the adjoining pixels and its energy zone to self-adaptively magnify the image[21]. Magneto-static field has also been imitated in image feature extraction. Bin Luo, A. D. J. Cross and E. R. Hancock proposed a new feature representation based on a magneto-static analogy, in which a vector potential was computed by appealing to an analogy in which the Canny edge-map is regarded as an elementary current density[22].

Besides the electro-static and magneto-static fields, other physical laws have also been exploited in image processing including: heat equation, anisotropic diffusion, fire propagation, fluid dynamics, physical particles, water-filling and watershed. Benjamin B. Kimia and Kaleem Siddiqi proposed a geometric smoothing method based on local curvature for shapes and images, which imitated the heat equation and anisotropic diffusion[23]. Xinhua Ji and Jufu Feng proposed a novel thinning algorithm based on a time-reversed heat conduction model, in which the image is viewed as a thermal conductor and the thinning task is then considered as an inverse process of heat conduction[24]. Siddharth Manay and Anthony Yezzi utilized an anisotropic diffusion model, which named the anti-geometric heat flow, for adaptive threshold of bimodal images and for segmentation of more general grayscale images[25]. Blum H. proposed the grassfire transform, in which growth from a boundary generates a description of an object that is centered on the space it includes[26]. The method simulated the process of "setting fire" to the borders of an image region to yield descriptors such as the region's skeleton or medial axis. Chwen-Jye Sze, et al proposed a discrete image flux conduction equation based on the concept of heat conduction theory, which was effectively applied to the selective image smoothing problem[27]. M. Bertalmio, et al introduced a class of automated methods for digital inpainting, which is inspired by classical fluid dynamics to propagate isophote lines continuously from the exterior into the region to be inpainted[28]. Zhao Yi proposed a novel image registration technique based on the physical behavior of particles[29]. Xiang Sean Zhou, et al presented a new approach named "Water-Filling Algorithm" for image feature extraction, which was a simulation of "flooding of connected canal systems (connected edges)"[30]. Another important method is the watershed algorithm. H. Digabel and C. Lantuejoul introduced the watershed transformation as a morphological tool[31]. Beucher S. and Lantuejoul C. used the watershed method in contour detection[32]. Vincent L. and Soille P. introduced an efficient and completely new implementation of watersheds[33].

Biology is another important source where novel processing methods have been derived from. Much of the research work has especially been carried out to exploit the biological swarms to derive novel image processing algorithms, such as the ant colony, fish school, social spider and bacteria. The artificial ant colony is a hot topic in this area. Chialvo D. R. and Millonas M. M. investigated via analysis and numerical simulation the formation of trails and networks in a collection of artificial ants, which was compared with the neural processes associated with the construction of cognitive maps in the hippocampus[34]. Vitorino Ramos and Filipe Almeida presented an extended model to deal with digital image habitats of artificial ants, which has potential application in pattern recognition[35]. Xiaodong Zhuang and Nikos E. Mastorakis applied artificial ant colony in image processing for feature extraction with the proposed perceptual graph[36]. S. Ali Etemad and Tony White presented a technique inspired by swarm methodologies such as ant colony algorithms for processing simple and complicated images[37]. Peng Huang, et al presented a novel segmentation algorithm based on the artificial ant colonies[38]. Piergiorgio Cerello, et al presented the Channeler Ant Model (CAM) based on the natural ant capabilities of dealing with 3-D environments through self-organization and

emergent behaviours, which was already in use for the automated detection of nodules in lung Computed Tomographies[39]. Yan Chen-yang, et al presented an artificial ant colony model for digital image edge detection base on the model which was first introduced by D. R. Chialvo et al, and later extend by V. Ramos et al[40]. Yudong Zhang and Lenan Wu proposed a novel method based on the artificial bee colony and the Rossler attractor for the estimation of human face pose in single images[41]. Alirezae Rezaee applied the ant colony system for edge detections, in which the edge of images can be considered as food for ants[42]. Huizhi Cao, et al presented a segmentation algorithm, which uses a biologically inspired paradigm known as artificial ant colonies[43]. Chad George and James Wolfer presented a hybrid algorithm inspired by ant colony and particle swarm technology to count an inventory of tubular steel bar stock from digital images[44].

The artificial ant colony has also been studied for artistic creation. A group led by Monmarche appears to be the first to actually use the term "ant painting" to describe the abstract images made by virtual ants that roam over a toroidal canvas[45]. In Gary Greenfield's paper, the author strived to show how designing ways to make ant paintings becomes an artistic pursuit[46].

The study of bacteria has been exploited in image processing. Sambarta Dasgupta, et al presented an algorithm for the automatic detection of circular shapes from complicated and noisy images, which is based on a swarm-intelligence technique named the Bacterial Foraging Optimization (BFO)[47]. Om Prakash Verma, et al proposed a new approach for edge detection using a combination of bacterial foraging algorithm (BFA) and probabilistic derivative technique[48]. Jianhua Yang and Guangyu Wang employed the differential response of the bacteriorhodopsin film to fabricate a 2D ON-center ganglion cell receptive field, which was characterized as a zero-cross filtering and was successfully used to detect the edge of an image[49]. Liu Dan, et al proposed an Artificial Bacilli Model for curve extraction in images based on real bacillus and Artificial Life theory[50].

Other biological swarm systems have also been studied for possible use in image processing. Chu Xiao-Li, et al proposed a method of image edge detection based on artificial fish swarm algorithm (AFSA) with chaos differential evolution algorithm (CDEA)[51]. Hao He and Yanqiu Chen used artificial life for image segmentation in their paper, where each pixel was associated with a life and evolved until the equilibrium was reached[52]. Christine Bourjot, et al presented an approach to region detection inspired by social spiders, which is based on a behavioral model determined by the simulation of collective weaving[53,54]. Jeff Jones, et al studied the interactions between simple agents and their image environment, which was then applied in image processing[55]. Charles E. White II, et al studied a swarm-based algorithm for color image segmentation[56]. W. Fledelius and B. H. Mayoh proposed a method for applying swarm theory to medical image analysis, in which nature serves as the inspiration for the swarms with agents consisting of termites, bloodhounds and children playing[57].

1.2 Overview of the book

In electro-static field and magneto-static field, the field and its source are two indivisible parts of a physical system. The field is derived from the source, and it naturally reflects the characters of the source distribution. On the other hand, the source may be mathematically inverted from the field. Therefore, the field and its source can be regarded as two domains of a special transform, and either of them can represent the characters of the other.

Images can be regarded as a kind of two-dimensional physical distribution (for the still images) or three-dimensional distribution (for the video image sequences). Image transform is the basic technique in image analysis, which finds a clearer and more convenient representation in the transform domain for better analyses. The natural transforms implied in the theory of physical electro-magnetic field just satisfy the need of the transform and feature extraction in image analysis. Moreover, the mathematical forms of electro-magnetic formulas have a unique advantage of the balance between local and global analysis, which is needed in many practical tasks.

In recent years, there have been increasing research efforts in nature inspired methods for image analysis. Promising results have been obtained in edge detection, corner detection, shape skeletonization, ear recognition, etc. Existing research focuses on scalar potential field, but the work on vector field transform is rare. The direct application of the formulas of physical fields is common, but there is much less work of adjusting and altering the forms of physical formulas to suit practical applications better. Moreover, most of the existing work in this area takes the image as the source and produces its virtual field, but the inverse transform from the image as a field to its virtual source is not investigated in previous research work. In this book, the authors try to widen the research of physical field inspired methods in image analysis by presenting several electro-magnetism inspired methods of vector field, relative field, and source-reverse transforms.

This book is based on the authors' original work in the area of physics-inspired methods for image analysis, which provide a new kind of natural representation of image structure imitating the electro-magnetic field. In this book, three virtual vector field transforms (diffusing vector field, curling vector field, compressing vector field) are presented based on the electro-static or magneto-static analogy. A scalar virtual potential field (relative potential field) is also proposed for image analysis. Besides, two different virtual source-reverse methods (potential source reverse, curling source reverse) are proposed imitating the physical fields derived from the static charges and static current distribution. The edge vector field is presented, and the virtual magnetic field generate by it is also investigated. In the above work, the basic properties of the virtual fields are analyzed and experimentally investigated, and their applications in image analysis are also studied by experiments. The experimental results indicate the impressive research value of electro-magnetism inspired methods in image analysis. There is also a novel idea underlying several virtual field methods in the book, which is named the "relative" field. It is an extension of the original definition of the physical fields by introducing the pixel difference into the definition. The authors' original work has proved the effectiveness of the "relative" field idea in the relative potential field, the diffusing vector field, the curling vector field, and the compressing vector field.

The organization of the book is as following:

In Chapter 2, several electro-statics inspired methods are presented, including the relative potential field, diffusing vector field, and the compressing vector field. The potential source-reverse inspired by electro-statics is also discussed in this chapter.

In Chapter 3, the magneto-statics inspired methods are discussed, including the virtual edge current and the curling vector field. The curling source-reverse for grayscale images is also studied in this chapter.

In Chapter 4, the extension of the "relative field" methods from single image processing to image sequence analysis is discussed. The extension of the 2D relative potential field to 3D relative potential for image sequences is studied as a case study.

In Chapter 5, the extension of the "relative field" methods from grayscale image processing to color image is discussed. The extension of the grayscale relative potential to color relative potential is investigated as a case study.

Chapter 6 is the summary of the book, where the authors would like to discuss some interesting topics about the methods in the book, and also some possible future work.

2 Electro-Statics Inspired Methods

Image transform is an important way for feature extraction and analysis[58-63]. Most currently applied transforms change the signal form between the time or space domain and the parameter domain (or transform domain), such as the mathematically reversible transforms including Fourier transform (transform between the time or space domain and the frequency domain) and the Wavelet transform (transform between the time or space domain and the time-scale or space-scale domain)[64-68]. Novel image transform has become an important branch of image processing development[59-63].

In recent years, physics-inspired methodology has attracted more and more interest of researchers, which exhibits promising ability of effective feature extraction and analysis[3,17,19,22,69-74]. The fundamental principle underlying the methods inspired by physical fields is the transform from one form of the field to another, so that the feature of interest can be revealed[3,4,69,73,74]. The distribution of the field is determined by the field source distribution. Therefore, the field can reflect the structure feature of the source. Based on the imitation of the physical field, the digital images can be taken as virtual field source, and the field generated by the image also represents the image's structure feature, which can provide a novel way of image transform and analysis.

The physical electro-static field is an irrotational field (i.e. the curl of the field intensity is zero). The electro-static potential and field intensity have some unique characteristics which may be exploited in image transform and analysis. In this chapter, several novel methods of image field transform are proposed, which are inspired by three different aspects of physical electro-static field. These aspects include electro-static potential, electro-static force, and the divergence of the electro-static force as its field source. In these methods, the mathematical form of electro-static field is extended to a definition of "relative field" for image analysis, which introduces the measurement of pixel difference into the virtual field definition.

2.1 The relative potential field inspired by physical electro-static field

In physics, the electro-static potential field is determined by the source (i.e. the charge distribution)[75-78]. Therefore, the potential field can reflect some characteristics of the source. This relationship between the field and its source can be exploited in image transform, in which the image is regarded as the source (i.e. the pixels are regarded as discrete charges) and the virtual field generated by the source may reveal important features of the image. The attraction of the methods inspired by physical field is the possibility of a natural representation of image structure or image components without artificially set parameters such as the thresholds in image segmentation.

In this section, a scalar field transform for digital images is presented inspired by the physical electro-static potential. First, the definition of physical electro-static potential is reviewed. The formula of the physical electro-static potential generated by a charge q is as following[75-78]:

$$V = \frac{1}{4\pi\varepsilon} \cdot \frac{q}{r} \tag{2-1}$$

where V is the electro-static potential at a space point. q is the charge quantity. r is the distance between the charge and the space point. ε is a physical constant.

For the charge distribution ρ in the space, the potential field generated by ρ is given as following[75-78]:

$$V = \frac{1}{4\pi\varepsilon} \int_V \frac{\rho \cdot d\tau}{r} \tag{2-2}$$

where V is the electro-static potential at a space point. The integral in Equation (2-2) is for the whole region where the charge distribution ρ exists.

Many image processing techniques involves local operations in the image (i.e. local image features are extracted and analyzed)[79-81]. Local image features usually have the form of a binary function $h(x,y)$ defined on the two-dimensional image plane. On the other hand, the analysis of the image also requires consideration of each image point's neighbouring area in order to get practically useful results. For example, in some self-adaptive segmentation methods, local features are extracted and then the segmentation threshold for each point is determined adaptively according to its neighbouring area. It is indicated that both local and global analyses are needed in image processing[82-87].

Generally speaking, neighbouring points have stronger relevance than remote points in an image, i.e. the closer the distance, the stronger the relevance. In many image processing tasks, it is necessary to consider the balance between the strong local relevance of closely adjacent points in a small local area, and the weaker relevance of remote points in a large "background" area. A mathematical model is needed for the representation of the above local-global relevance between image points.

Equation (2-2) indicates that the potential of a charge q on a space point (i.e. the impact of q on that point) is in direct proportion to the reciprocal of the distance r. The mathematical form of the distance reciprocal in Equation (2-2) can inspire the representation of the local-global relevance between image points. For a point p in the space, the near charge distribution in the small local area has greater impact on p's potential than remote charge distribution. On the other hand, no matter how far the distance is, remote charge distribution still has relatively weak impact on p's potential. Moreover, the accumulation of the weak impacts of wide-range remote charge distribution can not be neglected. The above characteristic of the distance reciprocal form in Equation (2-2) is quite suitable for the requirement of image analysis that both local and global relevance between image points should be considered.

2.1.1 The relative potential field of gray-scale images

The electro-static potential has a suitable mathematical form to model the local-global relevance of image points. In this section, a general form of virtual potential field is proposed with the electro-static analogy. For image analysis, not only the distance between two image points but also the relationship between their gray-scale should be considered. Therefore, a general continuous form of gray-scale image virtual potential field is proposed as:

$$V_c^k(x,y) = A \cdot \int_a \int_b \frac{f(g(a,b),g(x,y))}{r_{(a,b)\to(x,y)}^k} da \cdot db \tag{2-3}$$

where $V_c^k(x,y)$ is the continuous image potential value on point (x,y). A is a predefined constant value. g is the gray-scale value of image points. f is a function defined according to specific image processing tasks, which represents the relationship between the gray-scale values of point (x,y) and (a,b). r is the distance between (x,y) and (a,b). k is a constant that affect the reciprocal's decreasing rate with the increasing distance r. The double integral in Equation (2-3) is on the two-dimensional image plane. For a specific processing task, the function f and the constants A, k should be pre-defined according to the specific processing task.

For digital images, the general discrete form of image virtual potential field is proposed as the discrete form of Equation (2-3):

$$V_d^k(x,y) = A \cdot \sum_{\substack{j=0 \\ (j\neq y \text{ or } i\neq x)}}^{H-1} \sum_{i=0}^{W-1} \frac{f(g(i,j), g(x,y))}{r_{(i,j)\to(x,y)}^k} \tag{2-4}$$

where $V_d^k(x,y)$ is the discrete image potential on point (x,y). A is a predefined constant value. H and W are the height and width of the digital image respectively. g is the gray-scale value of image points. f is a function defined according to specific image processing tasks, which represents the relationship between the gray-scale values of point (x,y) and (i,j). r is the distance between (x,y) and (i,j). k is a constant that affect the reciprocal's decreasing rate with the increasing distance r.

For some important image processing tasks such as segmentation and edge detection, the difference between pixel gray-scale values are the factor of major consideration. In this section the relative potential is proposed for gray-scale images based on the general form of discrete image potential, where the function $f(g(i,j), g(x,y))$ is specialized as the difference between the gray-scale values of the two image points (x,y) and (i,j):

$$V_R^k(x,y) = A \cdot \sum_{\substack{j=0 \\ (j\neq y \text{ or } i\neq x)}}^{H-1} \sum_{i=0}^{W-1} \frac{g(i,j) - g(x,y)}{r_{(i,j)\to(x,y)}^k} \tag{2-5}$$

where $V_R^k(x,y)$ is the relative potential of the digital image on point (x,y). A is a predefined constant value. H and W are the height and width of the digital image respectively. g is the gray-scale value of image points. r is the distance between (x,y) and (i,j). k is a constant that affect the reciprocal's decreasing rate with the increasing distance r.

Compared with the mathematic form of the electro-static potential, the proposed relative potential has two major differences. One is the replacement of the discrete charge with the gray-scale difference, which can make the relative potential represents the difference of one image point between others. The other is the k-th power of the distance r. Thus the adjustment of k can change the decreasing rate of the relevance between image points with the increasing distance r.

2.1.2 The property of the relative potential field

In Equation (2-5), the relevance between two image points with distance r is represented quantitatively by the reciprocal of r^k. The value of relative potential is virtually the weighted sum of the gray-scale difference between the image point on (x,y) and all other points, and the weight is the factor of relevance, i.e. the reciprocal of r^k. To investigate the properties of the relative potential field, experiments are carried out for a series of simple test images with the size of 128×128. When computing the relative potential values, the constant k in Equation (2-5) is pre-defined as k=1. Fig. 2-1 To Fig. 2-3 show the results for some typical test images.

Fig. 2-1(a) to Fig. 2-3(a) are the original test images. Fig. 2-1(b) to Fig. 2-3(b) are the relative potential value distributions of the corresponding test images, where larger gray-scale represents larger relative potential. Fig. 2-1(c) to Fig. 2-3(c) record the sign of each relative potential value, where white points represent positive values and black points represent negative values. The results shown in Fig. 2-1(c) to Fig. 2-3(c) indicate that the sign of the relative potential values will reverse across the boundary of two adjacent regions, which may be exploited in the segmentation of different regions in the image.

(a) The image *Test*1

(b) The relative potential value distributions

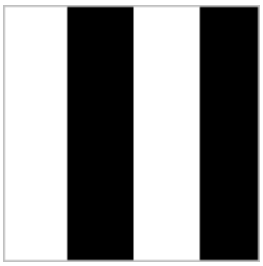

(c) The sign of each relative potential value

Fig. 2-1 The relative potential field of image *Test*1

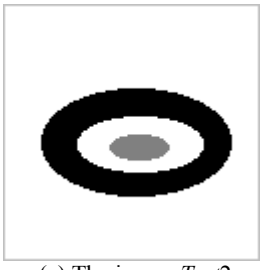

(a) The image *Test*2

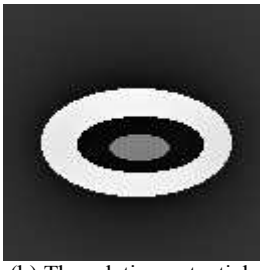

(b) The relative potential value distributions

(c) The sign of each relative potential value

Fig. 2-2 The relative potential field of image *Test*2

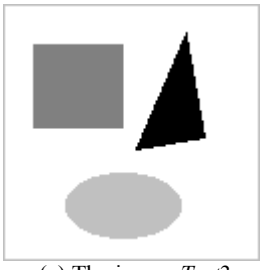

(a) The image *Test*3

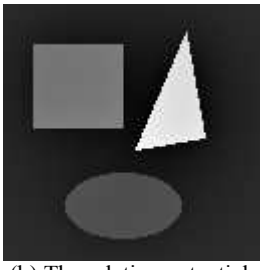

(b) The relative potential value distributions

(c) The sign of each relative potential value

Fig. 2-3 The relative potential field of image *Test*3

According to the definition of the virtual relative potential in Equation (2-5), the relative potential value of a point p is mainly affected by its local neighboring area. The local neighboring area consists of two classes of points. One class has those in the same region of p (i.e. with homogeneous gray-scale of p), and the other has those in the different region. For simple test images, the gray-scale difference in the same region is zero. Thus the relative potential of p is mainly affected by the gray-scale difference between p's region and its adjacent regions. Suppose A and B are two adjacent regions shown in Fig. 2-4. p_a and p_b are two border points at different border sides. p_a is in region A and p_b is in region B. g_a and g_b are the gray-scale values of region A and B respectively. According to the above discussion, the sign of p_a 's relative potential is determined by g_b - g_a, while the sign of p_b 's relative potential is determined by g_a - g_b. Thus the signs of p_a and p_b are opposite. This is why the sign of the relative potential will reverse across the region border. This property of the relative potential field can be exploited in image analysis.

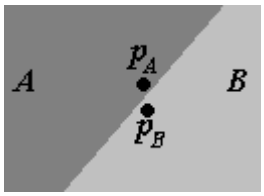

Fig. 2-4 p_a and p_b on different sides of the region border

On the other hand, the experimental results of some other test images indicate that the sign reverse of relative potential is not only across region borders but also possible within a region. Fig. 2-5 shows such a case, where the sign reverse occurs in the middle region of the three in the image. This is because within a region the near points in the neighbouring area have the same gray-scale, and the accumulation of weak affects from wide range of remote image points will have effect on the relative potential value. Thus sign reverse may occur within some region. Therefore, it is indicated by the experimental results that the sign of relative potential will reverse across the region borders, and there is also possible sign reverse within a region.

(a) The image *Test*4 (b) The relative potential value distributions (c) The sign of each relative potential value

Fig. 2-5 The relative potential of image *Test*4

2.1.3 Image segmentation based on the relative potential field

In the experimental results of the test images, it is shown that the sign of relative potential values are opposite in the two different adjacent regions. This can provide the basis of region division in images. In this section, a method of image region division in the relative potential field is proposed as following:

***Step*1**: Calculate the relative potential field for the gray-scale image;

***Step*2**: Obtain the sign distribution of the relative potential field;

***Step*3**: Group the adjacent points with the same sign of relative potential into connected regions. In the region grouping process, the adjacent pixels of the 4-connection (i.e. the upper, lower, left and right pixels) for an image point p is investigated. If any of the four adjacent pixels has the same sign of relative potential as p, it is grouped into the region which p belongs to. The obtained connected regions are the result of region segmentation for the image.

The obtained set of connected regions is the result of region division for the gray-scale image.

Fig. 2-6 to Fig. 2-8 are the region division results according to Fig. 2-1(c) to Fig. 2-3(c), where different regions are represented by different gray-scale values.

Fig. 2-6 The region segmentation result according to Fig. 2-1(c)

Fig. 2-7 The region segmentation result according to Fig. 2-2(c)

Fig. 2-8 The region segmentation result according to Fig. 2-3(c)

Real world images consist of much more complex region components than the simple test images. To investigate the effect of the above region division method on real world images, experiments are carried out for a series of typical real world images. The experimental results are shown in Fig. 2-9 to Fig. 2-12.

(a) The broadcaster image

(b) The visualization of the relative potential field with k=1

(c) The visualization of the relative potential field with k=2

(d) The visualization of the relative potential field with k=3

(e) The sign distribution of the relative potential in (b)

(f) The sign distribution of the relative potential in (c)

(g) The sign distribution of the relative potential in (d)

(h) The region division result for (e)

(i) The region division result for (f)

(j) The region division result for (g)

Fig. 2-9 The relative potential field and region division results for the broadcaster image

(a) The house image

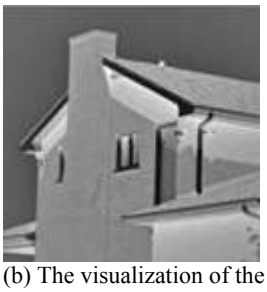

(b) The visualization of the relative potential field with k=1

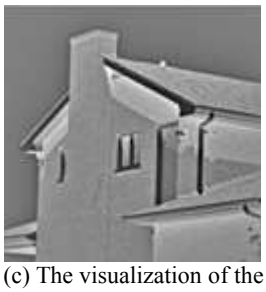

(c) The visualization of the relative potential field with k=2

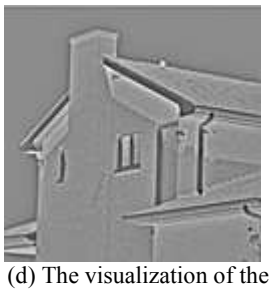

(d) The visualization of the relative potential field with k=3

(e) The sign distribution of the relative potential in (b)

(f) The sign distribution of the relative potential in (c)

(g) The sign distribution of the relative potential in (d)

(h) The region division result for (e)

(i) The region division result for (f)

(j) The region division result for (g)

Fig. 2-10 The relative potential field and region division results for the house image

(a) The peppers image

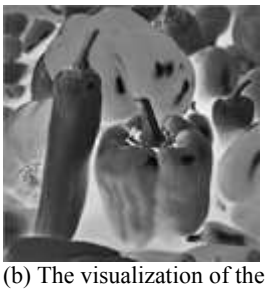

(b) The visualization of the relative potential field with k=1

(c) The visualization of the relative potential field with k=2

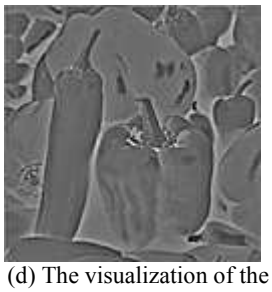

(d) The visualization of the relative potential field with k=3

(e) The sign distribution of the relative potential in (b)

(f) The sign distribution of the relative potential in (c)

(g) The sign distribution of the relative potential in (d)

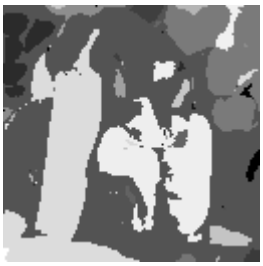

(h) The region division result for (e)

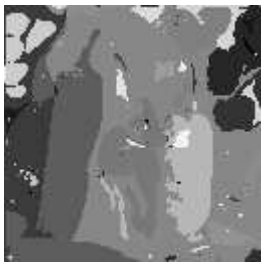

(i) The region division result for (f)

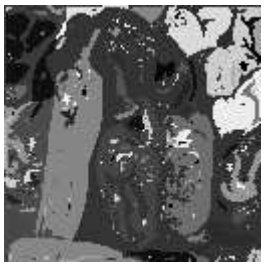

(j) The region division result for (g)

Fig. 2-11 The relative potential field and region division results for the peppers image

(a) The cameraman image

(b) The visualization of the relative potential field with k=1

(c) The visualization of the relative potential field with k=2

(d) The visualization of the relative potential field with k=3


(e) The sign distribution of the relative potential in (b)


(f) The sign distribution of the relative potential in (c)


(g) The sign distribution of the relative potential in (d)

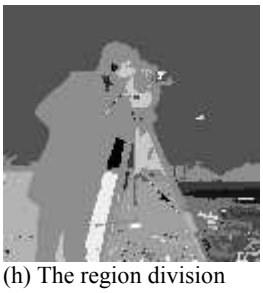
(h) The region division result for (e)


(i) The region division result for (f)

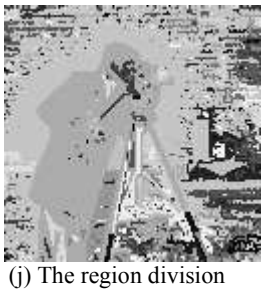
(j) The region division result for (g)

Fig. 2-12 The relative potential field and region division results for the cameraman image

Fig. 2-9(a) to Fig. 2-12(a) show the original images of the broadcaster, house, peppers and cameraman respectively. In the experiments, to investigate the influence of constant k (i.e. the relevance decreasing rate with increasing distance r) on image region division, relative potential field is calculated with k=1, 2 and 3 respectively. In the experiments, the results of relative potential field are visualized as gray-scale pictures. Fig. 2-9(b) to Fig. 2-12(b) show the results of relative potential field visualization with k=1 in Equation (2-5), where larger gray-scale values correspond to larger relative potential values. Fig. 2-9(c) to Fig. 2-12(c) show the results of relative potential field visualization with k=2 in Equation (2-5). Fig. 2-9(d) to Fig. 2-12(d) show the results of relative potential field visualization with k=3 in Equation (2-5).

To investigate the sign distribution of the relative potential field, the sign of relative potential on each point is recorded in the experiment. Fig. 2-9(e) to Fig. 2-12(e) show the sign distribution of the relative potential in Fig. 2-9(b) to Fig. 2-12(b) respectively, where white points represent positive values and black points represent negative values. Fig. 2-9(f) to Fig. 2-12(f) show the sign distribution of the relative potential in Fig. 2-9(c) to Fig. 2-12(c) respectively. Fig. 2-9(g) to Fig. 2-12(g) show the sign distribution of the relative potential in Fig. 2-9(d) to Fig. 2-12(d) respectively.

The region division is carried out based on the sign distribution of the relative potential field. Fig. 2-9(h) to Fig. 2-12(h) show the region division results for Fig. 2-9(e) to Fig. 2-12(e) respectively, where different regions are represented by different gray-scale values. Fig. 2-9(i) to Fig. 2-12(i) show the region division results for Fig. 2-9(f) to Fig. 2-12(f) respectively. Fig. 2-9(j) to Fig. 2-12(j) show the region division results for Fig. 2-9(g) to Fig. 2-12(g) respectively. The region division results show that for real world images the region division method may obtain large amount of region elements of the image.

Table 2-1 shows the region numbers obtained by the region division method for the real world images with the constant k=1, 2, and 3 respectively. Table 2-1 indicates that larger value of k can obtain more detailed region division result, because larger value of k causes faster decreasing rate of the relevance between image points with the increasing distance r.

Table 2-1 The number of regions obtained with different value of *k*

	The number of regions obtained by the region division based on the sign distribution of the relative potential field		
	***k*=1**	***k*=2**	***k*=3**
broadcaster image	19	39	659
house image	85	268	946
peppers image	72	122	371
cameraman image	161	298	795

The region division results of real world images consist of large amount of region elements due to their complexity. To obtain practically useful segmentation result, a region merging method is proposed for the region division results of real world images based on the gray-scale similarity of adjacent regions. First, an expected number of remaining regions is given (usually by trail). Then the following steps are carried out to merge regions until the expected region number is reached:

***Step*1**: For each region in the image, calculate its average gray-scale value.

***Step*2**: Find the pair of neighboring regions with the least difference of the average gray-scale, and merge them into one region.

***Step*3**: If current region number is larger than the expected region number, return to ***Step*1**; otherwise, end the merging process.

The region merging results for the real world images are shown in Fig. 2-13 to Fig. 2-16, where different regions are represented by different gray-scale. Fig. 2-13(a) to Fig. 2-16(a) show the merging results of Fig. 2-9(h) to Fig. 2-12(h) respectively. Fig. 2-13(b) to Fig. 2-16(b) show the merging results of Fig. 2-9(i) to Fig. 2-12(i) respectively. Fig. 2-13(c) to Fig. 2-16(c) show the merging results of Fig. 2-9(j) to Fig. 2-12(j) respectively. The merging results indicate that larger value of *k* makes more detailed region division, and correspondingly the merging results can be more accurate.

(a) The merging result of Fig. 2-9(h) (b) The merging result of Fig. 2-9(i) (c) The merging result of Fig. 2-9(j)

Fig. 2-13 The region merging results for the broadcaster image

(a) The merging result of Fig. 2-10(h) (b) The merging result of Fig. 2-10(i) (c) The merging result of Fig. 2-10(j)

Fig. 2-14 The region merging results for the house image


(a) The merging result of Fig. 2-11(h)

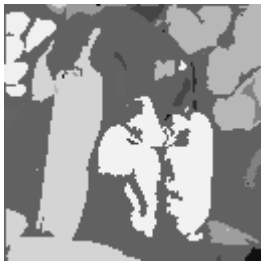
(b) The merging result of Fig. 2-11(i)

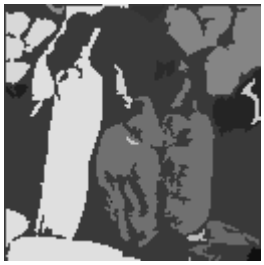
(c) The merging result of Fig. 2-11(j)

Fig. 2-15 The region merging results for the peppers image


(a) The merging result of Fig. 2-12(h)


(b) The merging result of Fig. 2-12(i)


(c) The merging result of Fig. 2-12(j)

Fig. 2-16 The region merging results for the cameraman image

Based on the above discussions, in this section a novel image segmentation method is proposed with the relative potential field. The procedure of the segmentation is as following:

***Step*1**: Calculate the relative potential field for the gray-scale image;

***Step*2**: Carry out the region division based on the sign distribution of the relative potential field;

***Step*3**: Merge the region division result to a pre-defined number of regions.

The experimental results for some other real-world images are shown in Fig. 2-17 to Fig. 2-19, including the image of boat, heart and pills. In the segmentation experiment, the value of k is pre-defined as 3. The experimental results have proved the effectiveness of the proposed segmentation method.

The mathematical form of the physical electro-static potential provides a suitable model for the representation of the local-global relevance between image points. In this section, the relative potential field is proposed with the electro-static analogy. The image structure information can be represented by the region components obtained in the region-division of the relative potential field. The experimental results indicate that the sign distribution of the relative potential field can serve as the basis for image region division, based on which an image segmentation method is proposed. As a typical "relative field" method in this book, the relative potential method will be extended for image sequence processing and color image processing in Chapter 4 and Chapter 5.


(a) the boat image


(b) the sign distribution of the relative potential

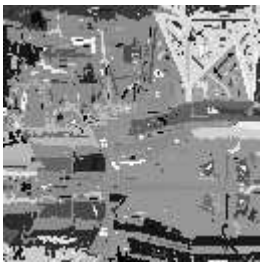

(c) the original region division result has 622 regions

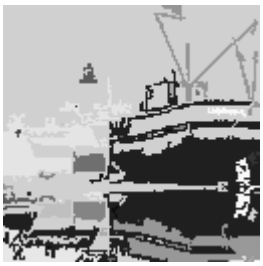

(d) the region merging result (60 regions)

Fig. 2-17 The segmentation result for the boat image

(a) the heart image

(b) the sign distribution of the relative potential

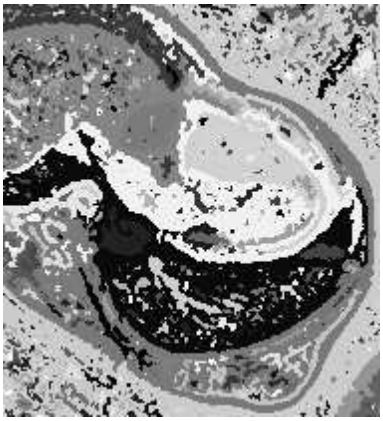

(c) the original region division result has 1207 regions

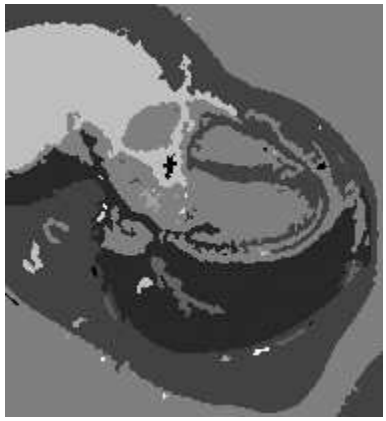

(d) the region merging result (70 regions)

Fig. 2-18 The segmentation result for the heart image

(a) the pills image

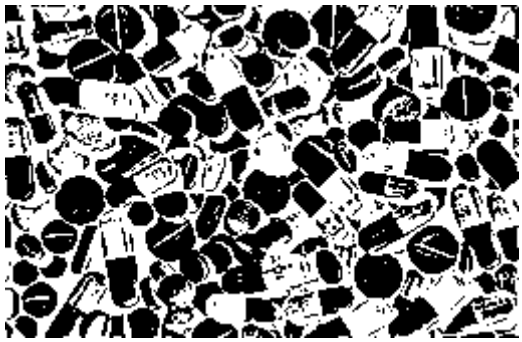

(b) the sign distribution of the relative potential

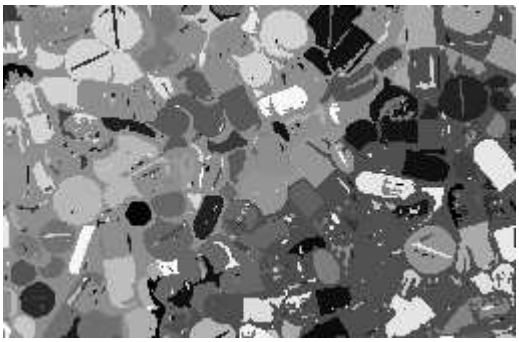

(c) the original region division result has 762 regions

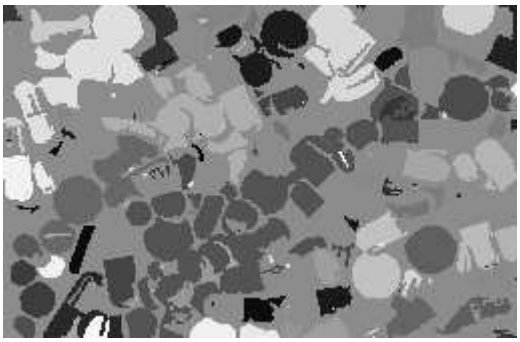

(d) the region merging result (150 regions)

Fig. 2-19 The segmentation result for the pills image

2.2 Vector field methods Inspired by electro-static field

Besides the scalar field of the electro-static potential, the vector field of field intensity (or the force field) is another basic form of the physical electro-static field. In physics, the force of two charges q_1 and q_2 is given as following[75-78]:

$$\vec{F}_{12} = \frac{1}{4\pi\varepsilon} \cdot \frac{q_1 q_2}{r_{12}^2} \cdot \frac{\vec{r}_{12}}{r_{12}} \tag{2-6}$$

where $\vec{F}_{12}$ is the force of q_1 on q_2, $\vec{r}_{12}$ is the vector from q_1 to q_2, r_{12} is the length of $\vec{r}_{12}$, $4\pi\varepsilon$ is an item of constant. Just as the electro-static potential, the definition of electro-static force can be exploited in field transform of images. In the study of image transform, vector field transformation is an attracting methodology, in which both vector length and vector direction can be exploited for feature extraction and analysis. Electro-static analogy has become a useful way for designing vector field transform of images. The force field method imitating Equation (2-6) has been proposed and applied in ear recognition by other researchers. In this book, the mathematical form of Equation (2-6) is extended to a more general definition of vector field transform for images. If two image points are regarded as two charged particles, the force vector generated by one point on the other can be defined. Of course, such definition of vector transform between two image points must be reasonable and proper in order to reflect certain image features and thus has potential applications.

In the static electric field, the magnitude of the field force is determined by the quantity of the two electric charges, and also by their distance. The direction of the field force is determined by the relative position of the two electric charges. Imitating the mathematical form of Equation (2-6), a general form of the vector from point (i,j) to point (x,y) is defined as following:

$$\vec{V}_G = \frac{f(g(i,j), g(x,y))}{r_{(i,j)\to(x,y)}^2} \cdot \frac{\vec{r}_{(i,j)\to(x,y)}}{r_{(i,j)\to(x,y)}} \tag{2-7}$$

where $f(g(i,j),g(x,y))$ is a function of the gray-scale or other image properties on the two points (i,j) and (x,y). $\vec{r}_{(i,j)\to(x,y)}$ is the radius vector from (i,j) to (x,y). In different image processing tasks, the function f should be defined according to particular requirements of the problem. Therefore, the vector field transform of the image on point (x,y) is defined as the accumulation of the vectors from all the other points to (x,y):

$$\vec{V}_G(x,y)=\sum_{\substack{j=0\\(i,j)\neq(x,y)}}^{H-1}\sum_{i=0}^{W-1}\frac{f(g(i,j),g(x,y))}{r^2_{(i,j)\to(x,y)}}\cdot\frac{\vec{r}_{(i,j)\to(x,y)}}{r_{(i,j)\to(x,y)}} \tag{2-8}$$

where H and W are the height and width of the image respectively. Different definitions of the function $f(g(i,j),g(x,y))$ produce different transform results. In this section, two vector field transforms are presented based on the general form of Equation (2-8)

2.2.1 The diffusing vector field of gray-scale images

In physics, a charged area with certain distribution of charge generates its electric field within and outside the area. In this section, a novel vector transform of gray-scale image is proposed based on an electro-static analogy, in which the image is regarded as a charged area. In the proposed transform, the form of the field force is extended by introducing the gray-scale difference between the related image points, which has the form of "relative field". With such transform definition, it is proved by the following analysis that in the generated field the vectors in a homogeneous area diffuse towards the outside of that area. Therefore, the generated field is named the "diffusing vector field".

2.2.1.1 The repulsion vector between image points

The form of electronic force formula has some characteristics as follows:

(1) The formula has the power of distance r as one of the denominator. The larger the distance between two charged particles, the smaller the force. In images, this causes a kind of local feature extraction. One image point has strong effect on the points nearby, but has little effect on distant points.

(2) The force between two charged particles is related to the electric quantity of both charged particles. In images, the effect of one image point on the other point can also be defined with relation to the intensities (i.e. gray-scale values) of the two image points. Thus certain image features may be extracted by the vector field transform.

In this section, the vector generated by one image point $g(i,j)$ on another position (x,y) is defined with direct relation to the reciprocal of the intensity difference of the two image points. The definition is proposed to generate repulsion vector between neighboring points in homogeneous areas. The repulsion vector is defined as following:

$$\vec{V}=\frac{A}{(|g(i,j)-g(x,y)|+\varepsilon)\cdot r^2_{(i,j)\to(x,y)}}\cdot\frac{\vec{r}_{(i,j)\to(x,y)}}{r_{(i,j)\to(x,y)}} \tag{2-9}$$

where $\vec{V}$ is the vector generated by image point (i,j) on position (x,y), g represents the intensity of image points, $\vec{r}_{(i,j)\to(x,y)}$ is the vector from (i,j) to (x,y), $r_{(i,j)\to(x,y)}$ is the length of $\vec{r}_{(i,j)\to(x,y)}$, ε is a pre-defined small positive value which guarantees that the above definition is still valid when $g(i,j)$ is equal to $g(x,y)$, A is a pre-defined item of constant. According to the above definition, the two components of $\vec{V}$ are as following:

$$V_x=\frac{A\cdot(x-i)}{(|g(i,j)-g(x,y)|+\varepsilon)\cdot((x-i)^2+(y-j)^2)^{3/2}} \tag{2-10}$$

$$V_y=\frac{A\cdot(y-j)}{(|g(i,j)-g(x,y)|+\varepsilon)\cdot((x-i)^2+(y-j)^2)^{3/2}} \tag{2-11}$$

where V_x and V_y are the two components on the direction of x-coordinate and y-coordinate respectively.

2.2.1.2 The diffusing vector field of images

Based on the repulsion vector, the vector field transform on each image point (x,y) can be defined for the whole image by summing up the vectors produced by all image points. The vector generated by the whole image on point (x,y) is defined as following:

$$\vec{V}(x,y) = \sum_{\substack{j=0 \\ (i,j)\neq(x,y)}}^{H-1} \sum_{i=0}^{W-1} A \cdot \frac{\vec{r}_{(i,j)\to(x,y)}}{(|g(i,j)-g(x,y)|+\varepsilon)\cdot r^3_{(i,j)\to(x,y)}} \tag{2-12}$$

where $\vec{V}(x,y)$ is the vector produced by the transform on position (x,y), W and H are the width and height of the image respectively. According to the above definition, the two components of $\vec{V}(x,y)$ are as following:

$$V_x(x,y) = \sum_{\substack{j=0 \\ (i,j)\neq(x,y)}}^{H-1} \sum_{i=0}^{W-1} \frac{A\cdot(x-i)}{(|g(i,j)-g(x,y)|+\varepsilon)\cdot r^3_{(i,j)\to(x,y)}} \tag{2-13}$$

$$V_y(x,y) = \sum_{\substack{j=0 \\ (i,j)\neq(x,y)}}^{H-1} \sum_{i=0}^{W-1} \frac{A\cdot(y-j)}{(|g(i,j)-g(x,y)|+\varepsilon)\cdot r^3_{(i,j)\to(x,y)}} \tag{2-14}$$

where $V_x(x,y)$ and $V_y(x,y)$ are the components on the direction of x-coordinate and y-coordinate respectively.

Because the effect of an image point on another decreases quickly with the increase of distance, the vector on any image point is determined by two major factors: the strong effect of a few neighboring points, and the accumulated effect of large amount of distant points. In the definition of the diffusing vector field, the smaller the gray-scale difference the relatively larger the vector length. Therefore, a diffusing vector field will appear in each homogeneous area because the strong "repulsion" between similar image points. On the other hand, at the boundary of two different areas, the vectors field at one side of the boundary will be in opposite directions of those at the other side.

To investigate the property of the proposed transform, a group of simple test images are transformed to the diffusing vector field. The algorithm is implemented by programming in *C* language. The results of some typical test images are shown as following. Three of the test images are shown in Fig. 2-20, Fig. 2-23 and Fig. 2-26. These images are of size 32×32. For a clear view, they are also shown 4 times of original size. Fig. 2-21, Fig. 2-24 and Fig. 2-27 show the length of each vector in the transformed field respectively, where larger gray-scale values correspond to larger vector length. The results are also shown 4 times of original size for a clear view. The direction of each vector in the transformed field is digitalized into 8 discrete directions for further processing. Fig. 2-22, Fig. 2-25 and Fig. 2-28 show the direction of the transformed field for each test image.

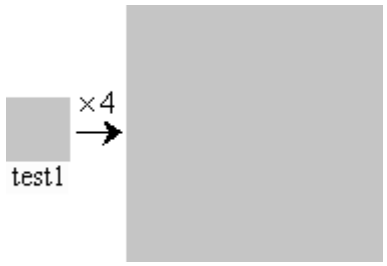

Fig. 2-20 The first image *test1* (the original image, and 4 times of original size on the right)

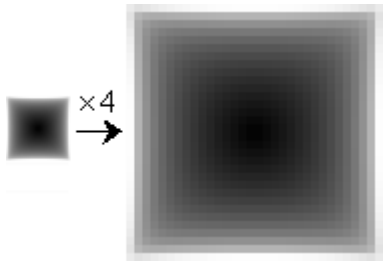

Fig. 2-21 The vector length in the transformed field of *test1* (the original image; 4 times of original size on the right)

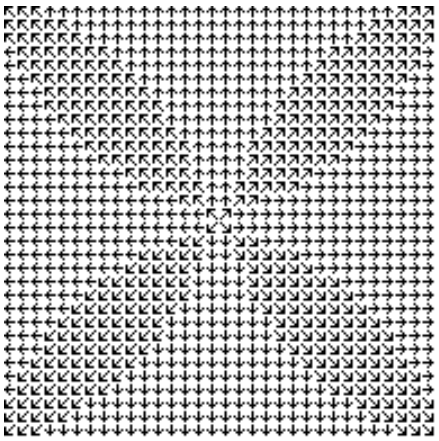

Fig. 2-22 The direction of each vector in the transformed field of *test1*

Fig. 2-23 The second image *test2* (the original image on the left, and 4 times of original size on the right)

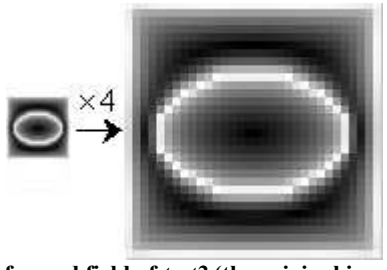

Fig. 2-24 The vector length in the transformed field of *test2* (the original image; 4 times of original size on the right)

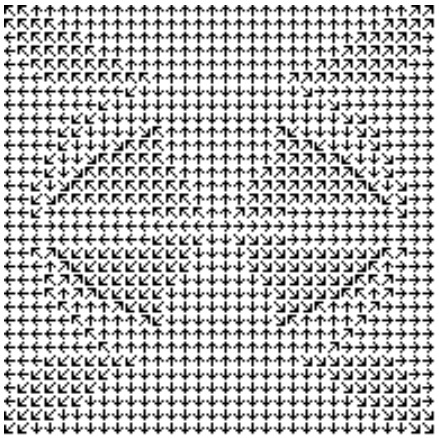

Fig. 2-25 The direction of each vector in the transformed field of *test2*

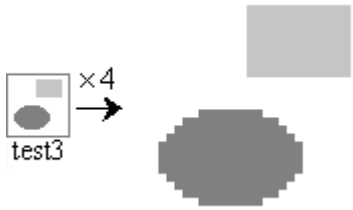

Fig. 2-26 The third image *test3* (the original image on the left, and 4 times of original size on the right)

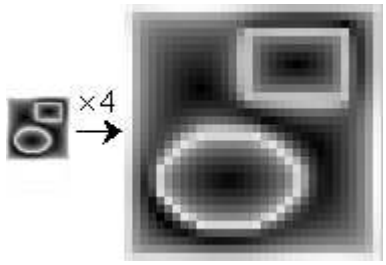

Fig. 2-27 The vector length in the transformed field of *test3* (the original image; 4 times of original size on the right)

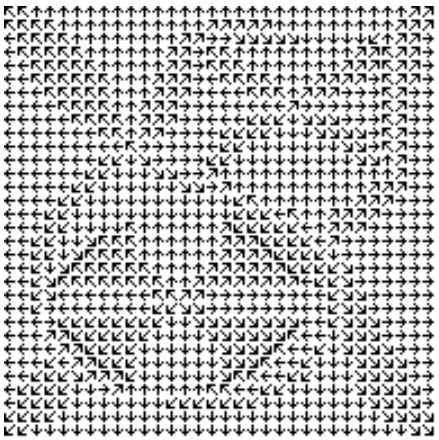

Fig. 2-28 The direction of each vector in the transformed field of *test3*

The image *test1* is an image of monotonous gray-scale, i.e. the whole image is a homogeneous area. In the transformed field of *test1*, it is obvious that the whole field is diffusing from the center of the image towards the outside. There is an ellipse area in image *test2*. In image *test3*, there are an ellipse area and a rectangle area. In their transformed fields, the fields in the homogeneous areas are diffusing outward from the center of each area. On the boundaries of the areas, it is obvious that the vectors at one side of the boundary line have opposite directions of those on the other side. The experimental results of the test images indicates that the proposed transform produce diffusing vector

field within the homogeneous areas, but generates vectors of opposite directions at the two opposite sides along the area boundary.

2.2.1.3 The primitive area in the diffusing vector field

The experimental results of the test images indicate that in the homogeneous area a diffusing vector field will be produced, and the diffusing field ends at the boundary of the homogeneous area because the vectors outside have opposite directions of those within the area along the boundary. Therefore, homogeneous areas in the image can be represented by areas with consistent diffusing vectors in the transformed field. Each diffusing vector area corresponds to an area of homogeneous image points. The area of consistent diffusing vectors extracted from the transformed field is given the name "primitive area", which can be regarded as an elementary component of an image because it is regarded as homogeneous in the transform process.

According to the definition, the image *test1* is a whole primitive area, while the image *test3* has at least two primitive areas: the ellipse, the rectangle and the background area. All the primitive areas can be extracted from the diffusing vector field, which can be exploited in further image analysis. The primitive area in the diffusing vector field forms the basis of the proposed image segmentation method. In following sections, the method of extracting primitive areas are presented and implemented on test images.

2.2.1.4 Diffusing centers in the primitive area

In each primitive area, the vector field diffuses from the center towards the outside, thus the area center becomes the source of the diffusing field. Therefore, the area centers are the begin points to extract primitive areas. Here the source of the diffusing field is defined as the diffusing center. According to the experimental results of the test images, the definition of the diffusing center is given as following: for a square area consists of four image points, if none of the vectors on these points has component of inward direction into the area, the square area is part of a diffusing center. Fig. 2-29 shows the allowed vector directions on each point in a diffusing center.

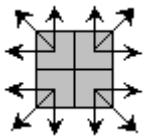

Fig. 2-29 The allowed vector directions in diffusing center

In Fig. 2-22, Fig. 2-25 and Fig. 2-28, according to the above definition the diffusing centers can be found, which are shown in Fig. 2-30, Fig. 2-31 and Fig. 2-32. The source points in the diffusing centers are indicated in gray.

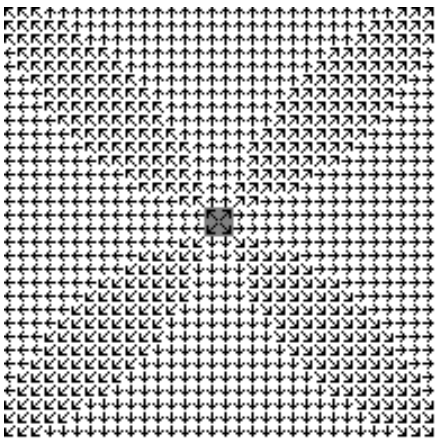

Fig. 2-30 The diffusing centers in Fig. 2-22

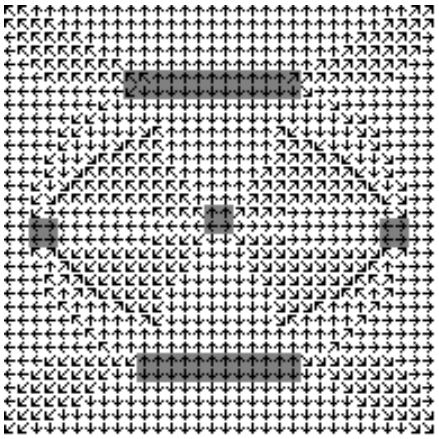

Fig. 2-31 The diffusing centers in Fig. 2-25

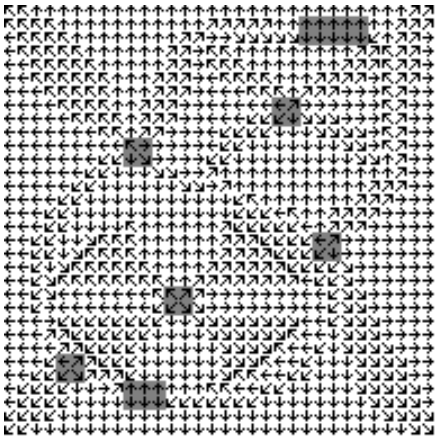

Fig. 2-32 The diffusing centers in Fig. 2-28

The image *test1* is a homogeneous area, therefore there is only one diffusing center found in Fig. 2-30. There is an area of ellipse in the image *test2*, and the diffusing center of the ellipse can be found in Fig. 2-31. Moreover, there are also four other diffusing centers found in the background area. The image *test3* has an ellipse and a rectangle. Correspondingly, in Fig. 2-32 there is one diffusing center for the ellipse, one for the rectangle, and five for the background area. It is indicated that in a large and irregular area there may be more than one diffusing center found, such as the background area.

2.2.1.5 Primitive area extraction by the area-expanding method

The primitive areas are the basic elements in the diffusing vector field, which is a kind of representation of the image structure. According to the above analysis and experimental results, in a primitive area the vectors diffusing outwards from the diffusing center (i.e. the area center). Moreover, the diffusing vectors in the primitive area end at the area boundary where opposite vectors at the outside are encountered. Therefore, the primitive area can be extracted by expanding outwards from the diffusing center along the directions of the diffusing vectors. The proposed area-expanding method to extract the primitive area is as follows:

***step*1:** Calculate the diffusing vector field of the image, and each image point now has a vector on it (the vector is discretized into 8 directions).

***step*2:** Get the diffusing center points in the diffusing vector field according to the definition in section 2.2.1.4.

***step*3:** Assign each diffusing center a unique area label (here a unique area number is given to the points in each diffusing center, while the points not in the diffusing center are left unlabeled).

***step*4:** Then a process of area-expanding in the diffusing vector field is implemented to extract the primitive areas.
For each labeled point in the image, select five of its eight neighboring points that are nearest to its vector's direction. For each of the five selected neighboring points, if it is unlabeled and its vector is not opposite to the labeled point's vector (i.e. the area boundary is not reached), it is labeled the same area number of the labeled point. On the other hand, if the neighboring point has been labeled with another area number, a principle of least gray-scale difference is applied to decide which of the two areas the point should belong to. The difference between its gray-scale and either area's average gray-scale is calculated. The point will belong to the area with less gray-scale difference. By this way, the primitive area can expand by iteration until the area boundary is reached.
The above process is repeated until the areas all stop expanding (i.e. no more unlabeled point can be given a new area number).
***step*5:** If there are still unlabeled points when the expanding of the areas stops, the principle of least gray-scale difference is applied to assign each unlabeled point an area number.
For each unlabeled point, calculate the difference between its gray-scale and the average gray-scale of its neighboring areas. Then this unlabeled point is merged into the neighboring area that is of the least difference.

The primitive areas are extracted for the test images according to the proposed area-expanding method based on the diffusing vector fields. Some of the experimental results are shown in Fig. 2-33, Fig. 2-34 and Fig. 2-35. In these three figures, the original images and the results of primitive areas extraction are shown. The results are also shown 4 times of original size for a clear view. In these figures, different primitive areas are distinguished from each other by different gray-scale values.

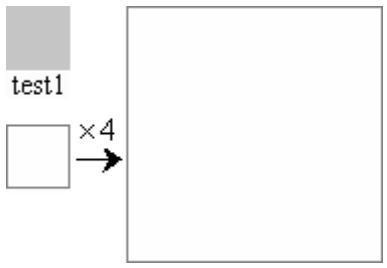

Fig. 2-33 The result of primitive area extraction for *test*1

The image *test*1 is a homogeneous area. Therefore the primitive area extracted in *test*1 is only one complete area (i.e. the image itself).

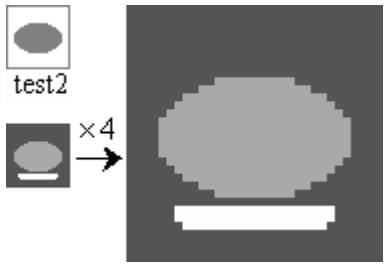

Fig. 2-34 The result of primitive area extraction for *test*2

The image *test*2 contains an ellipse, and 3 primitive areas are obtained. The ellipse is extracted as one primitive area, and there are 2 other primitive areas extracted in the background area of *test*2.

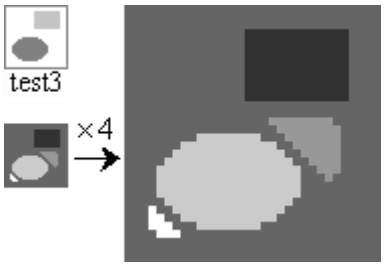

Fig. 2-35 The result of primitive area extraction for *test*3

The image *test*3 contains an ellipse and a rectangle, and 5 primitive areas are obtained. The ellipse and rectangle in ellipse and rectangle are extracted as two primitive areas, and there are 3 other primitive areas extracted in the background area of *test*3.

The experimental results for the test images show that the object areas can be extracted as primitive areas such as the ellipse in *test*2 and the ellipse and rectangle in *test*3. On the other hand, the number of primitive areas may be less than the number of diffusing center extracted. This is because two or more diffusing center may merge into one area in ***step*4** in the proposed area-expanding method.

2.2.1.6 Gray-scale image segmentation based on the primitive area extraction

Compared with the test images, practical images obtained in the real world are more complex and contains much more objects. The boundaries between areas in these images are not as clear and distinguishable as in the test images. In the experiments, the primitive areas are also extracted for the pepper image, the cameraman image and the house image. These images are of the size 128×128. The experimental results show that there are a large number of primitive areas extracted from the practical images. There are 341 primitive areas in the pepper image, 305 in the cameraman image and 263 in the house image. This is because the complexity of these real world images.

The primitive area serves as a kind of representation of image structure. To implement meaningful image segmentation, area merging must be done to get more practically useful result. An area merging method is proposed to combine primitive areas based on the least gray-scale difference principle. First an expected number of remaining areas after merging is given. Then the following steps are carried out to merge areas until the expected area number is reached:

***step*1:** For each area in the image, calculate its average gray-scale.

***step*2:** Find the pair of neighboring areas with least average gray-scale difference, and merge them into one area.

***step*3:** If current area number is larger than the final area number, return to ***step*1**; otherwise, end the merging process.

The original image of the pepper image, the cameraman image and the house image are shown in Fig. 2-36, Fig. 2-38 and Fig. 2-40. The result of merging primitive area is shown in Fig. 2-37, Fig. 2-39 and Fig. 2-41 respectively, where different areas are distinguished from each other by different gray-scale values. Fig. 2-37 shows the result of merging 341 primitive areas into 20 areas for the peppers image. Fig. 2-39 shows the result of merging 305 primitive areas into 12 areas for the cameraman image. Fig. 2-41 shows the result of merging 263 primitive areas into 20 areas. The experimental results indicate that the primitive area merging method can effectively implement image segmentation, and the main objects in the images can be successfully extracted by the proposed method.

Fig. 2-36 The image of peppers for the peppers image (20 areas remained)

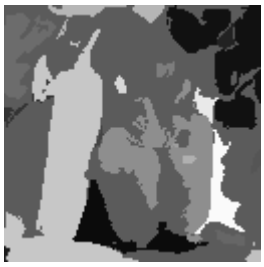

Fig. 2-37 The primitive area merging result

Fig. 2-38 The image of cameraman for the cameraman image (12 areas remained)

Fig. 2-39 The primitive area merging result

Fig. 2-40 The image of house for the house image (20 areas remained)

Fig. 2-41 The primitive area merging result

Based on the previous sections, here a novel image segmentation method based on the diffusing vector field is proposed as following:

***step*1:** Calculate the diffusing vector field of the image;

***step*2:** Get the diffusing center points;

***step*3:** Extract the primitive areas;

***step*4:** Merge the primitive areas according to the requirement of final are number.

Fig. 2-42 to Fig. 2-47 show the experimental results for some other real-world images, including the image of locomotive, heart and a satellite image.

In the diffusing vector field of images, homogeneous areas are expressed as the areas with a vector group diffusing outwards from the center. By finding the area center and expanding the area from the center, primitive areas can be extracted. Image segmentation can be implemented by merging the primitive areas. The effectiveness of the method has been indicated by the experimental results.

Fig. 2-42 The image of locomotive locomotive image (20 areas remained)

Fig. 2-43 The segmentation result for the

Fig. 2-44 The medical image of heart

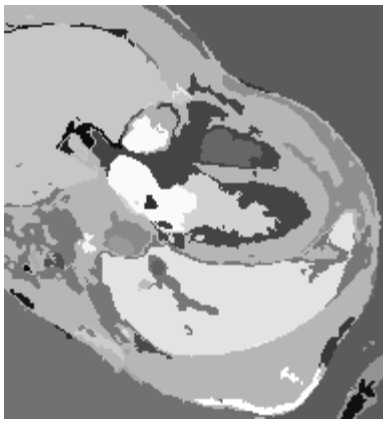

Fig. 2-45 The segmentation result for the heart image (50 areas remained)

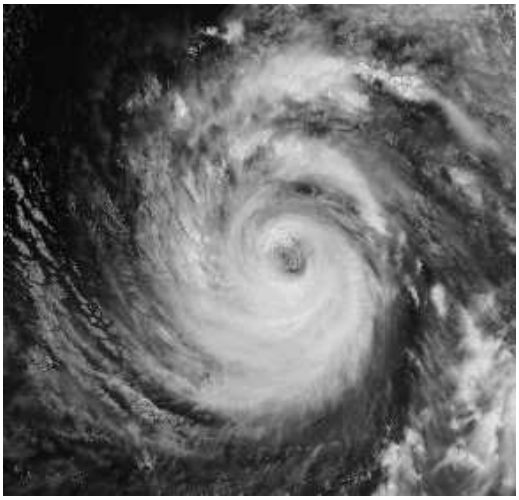

Fig. 2-46 The image of a satellite image

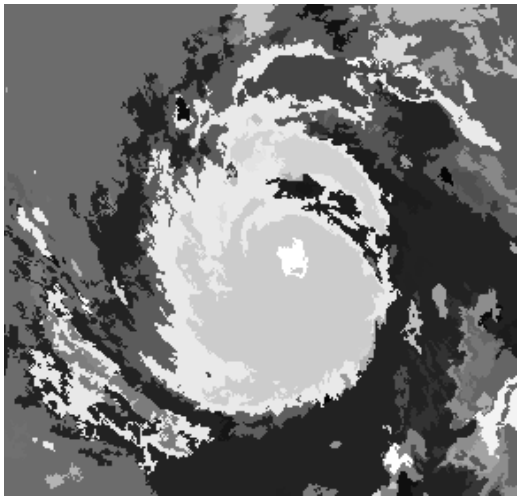

Fig. 2-47 The segmentation result for the image of the satellite image (100 areas remained)

2.2.2 The compressing vector field of gray-scale images

In this section, another image vector transform named "compressing vector field" is studied by re-define the function $f(g(i,j),g(x,y))$ in Equation (2-8). Compared with the diffusing vector field, the analysis and experimental results of the "compressing vector field" indicate that different definitions of the function $f(g(i,j),g(x,y))$ can produce different transform results and processing effects for images.

2.2.2.1 The definition of the compressing vector field

For gray-scale image segmentation, the gray-scale difference between points is small within a homogeneous region, while the gray-scale difference is relatively large between points of two different regions. This is the basis of segmentation by gray-scale difference. To reflect gray-scale difference, $f(g(i,j),g(x,y))$ in Equation (2-7) is defined as the gray-scale difference between (x,y) and (i,j):

$$\vec{V} = \frac{|\, g(i,j) - g(x,y) \,|}{r^2_{(i,j)\to(x,y)}} \cdot \frac{\vec{r}_{(i,j)\to(x,y)}}{r_{(i,j)\to(x,y)}} \tag{2-15}$$

The above vector has the form of repulsive force between image points, and it contains the information of gray-scale difference and relative position between the two points. The x and y

components of the vector are as following:

$$V_x = \frac{|g(i,j) - g(x,y)| \cdot (x-i)}{((x-i)^2 + (y-j)^2)^{3/2}}$$
$$V_y = \frac{|g(i,j) - g(x,y)| \cdot (y-j)}{((x-i)^2 + (y-j)^2)^{3/2}} \quad (2\text{-}16)$$

Based on the definition of the vector in Equation (2-15), the compressing vector field transform on point (*x,y*) is defined as the accumulation of the vectors from all the other points to (*x,y*):

$$\vec{V}(x,y) = \sum_{\substack{j=0 \\ (i,j)\neq(x,y)}}^{H-1} \sum_{i=0}^{W-1} \frac{|g(i,j) - g(x,y)|}{r^2_{(i,j)\to(x,y)}} \cdot \frac{\vec{r}_{(i,j)\to(x,y)}}{r_{(i,j)\to(x,y)}} \quad (2\text{-}17)$$

The *x* and *y* components are as following:

$$V_x(x,y) = \sum_{\substack{j=0 \\ (i,j)\neq(x,y)}}^{H-1} \sum_{i=0}^{W-1} \frac{|g(i,j) - g(x,y)| \cdot (x-i)}{((x-i)^2 + (y-j)^2)^{3/2}}$$
$$V_y(x,y) = \sum_{\substack{j=0 \\ (i,j)\neq(x,y)}}^{H-1} \sum_{i=0}^{W-1} \frac{|g(i,j) - g(x,y)| \cdot (y-j)}{((x-i)^2 + (y-j)^2)^{3/2}} \quad (2\text{-}18)$$

The repulsive vectors within a homogeneous region are relatively small because the gray-scale similarity between the points in that region. On the other hand, the repulsive vectors from the points outside that region to those within it are relatively large. Therefore, for any point in a homogeneous region, the diffusing tendency caused by the repulsive vector within the region is surpassed by the compression tendency caused by the repulsive vector from outside the region. Thus for each homogeneous region, a compressing vector field will be formed within it, which has the tendency to make the region shrink to its center. In another word, if a point in the region moves following the vectors' direction, it will finally reach the region center; if all points move in such a way, the region will finally shrink into its center points. This is the reason for the name "compressing vector field". And it is also the basis of region extraction in the compressing vector field.

2.2.2.2 Additional border force for compressing vector field in border regions

According to Equation (2-17), the vectors in the regions that are adjacent to the image border will have the diffusing tendency outward the image because there is no vector source outside the image border. In order to form a compressing vector region in those adjacent to the image border, additional border force is added, which generates repulsive vector from the image border to the image points:

$$\vec{V}_B(x,y) = \sum_{(m,n)\in Db} \frac{A}{r^2_{(m,n)\to(x,y)}} \cdot \frac{\vec{r}_{(m,n)\to(x,y)}}{r_{(m,n)\to(x,y)}} \quad (2\text{-}19)$$

where A is a pre-defined constant, D_b is the single border line surrounding the image. Therefore, the vector field transform for region extraction is proposed as following:

$$\vec{T}(x,y) = \vec{V}(x,y) + \vec{V}_B(x,y) \quad (2\text{-}20)$$

To investigate the properties of the compressing vector field with border force, experiments are carried out for a group of test images with the size 32×32. Some of the experimental results are shown from Fig. 2-48 to Fig. 2-62, including the original images and the magnitude and direction distribution of the vector field. In this section, the vector direction is discretized into eight directions. *Test1* is a homogeneous region as a whole. Fig. 2-49 shows the magnitude distribution of the vector field with border force. Fig. 2-50 shows the direction distribution, in which the border force will generate a vector field that makes each image point gather to the image's center position.

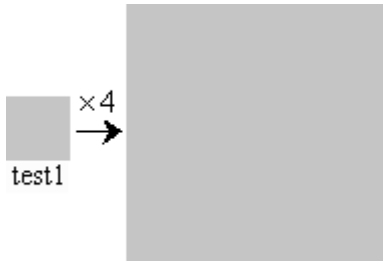

Fig. 2-48 The first image *Test1* (the original image on the left, and 4 times of original size on the right)

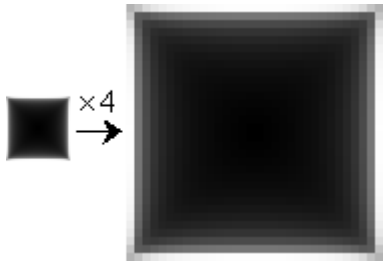

Fig. 2-49 The vector length in the compressing vector field of *Test1* with border force (4 times of original size on the right)

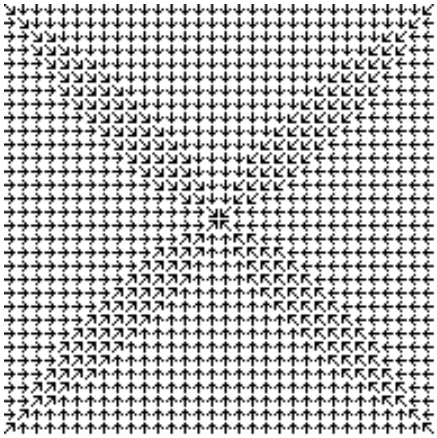

Fig. 2-50 The direction of each vector in the compressing vector field of *Test1* with border force

In the experimental results of image *Test2*, *Test3* and *Test4*, the direction distributions of the vector field without the border force are also given for comparison. Fig. 2-54, Fig. 2-58 and Fig. 2-62 show the direction distribution without the border force, while Fig. 2-53, Fig. 2-57 and Fig. 2-61 show the results with the border force. The comparison indicate the necessity of the additional border force, which makes all the homogeneous regions contain a corresponding compressing vector field regardless of their positions in the image. The compressing vectors in each homogeneous region are the basis for region segmentation.

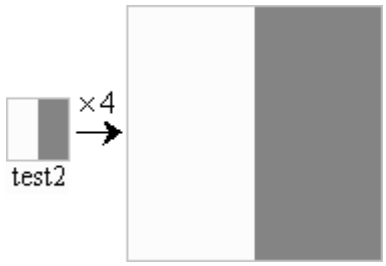

Fig. 2-51 The second image *Test2* (the original image on the left, and 4 times of original size on the right)

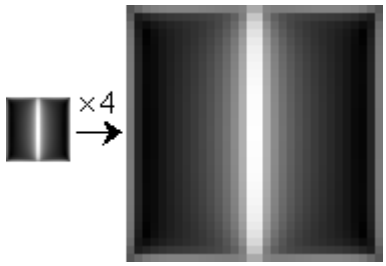

Fig. 2-52 The vector length in the compressing vector field of *Test2* with border force (4 times of original size on the right)

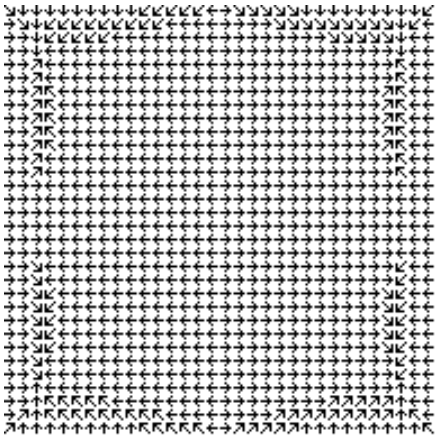

Fig. 2-53 The direction of each vector in the compressing vector field of *Test2* with border force

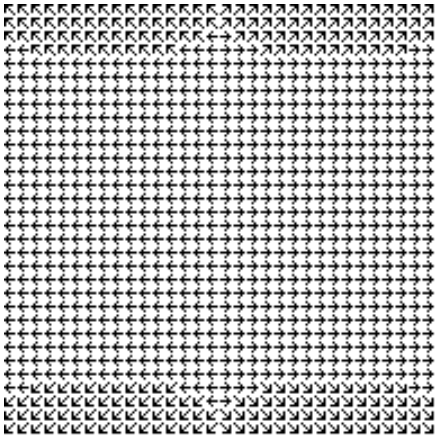

Fig. 2-54 The direction of each vector in the compressing vector field of *Test2* without border force

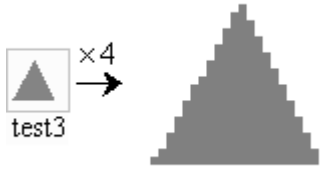

Fig. 2-55 The third image *Test3* (the original image on the left, and 4 times of original size on the right)

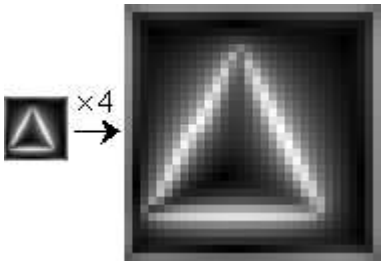

Fig. 2-56 The vector length in the compressing vector field of *Test3* with border force (4 times of original size on the right)

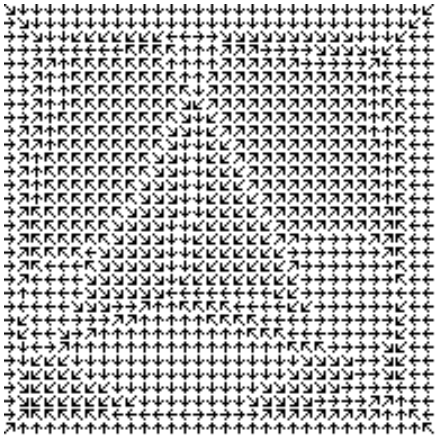

Fig. 2-57 The direction of each vector in the compressing vector field of *Test3* with border force

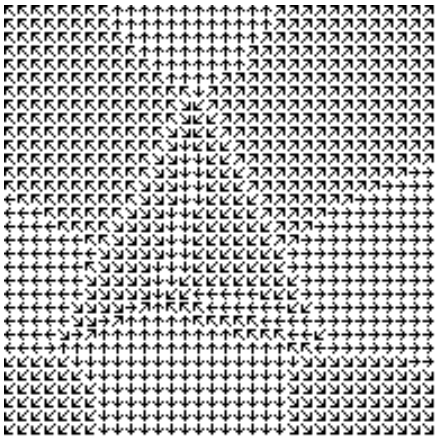

Fig. 2-58 The direction of each vector in the compressing vector field of *Test3* without border force

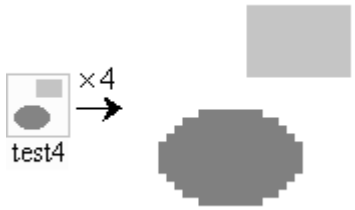

Fig. 2-59 The fourth image *Test4* (the original image on the left, and 4 times of original size on the right)

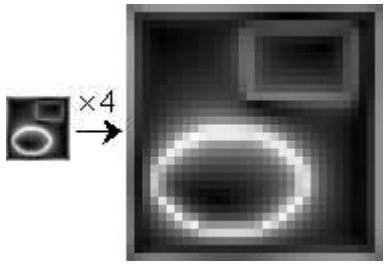

Fig. 2-60 The vector length in the compressing vector field of *Test4* with border force (4 times of original size on the right)

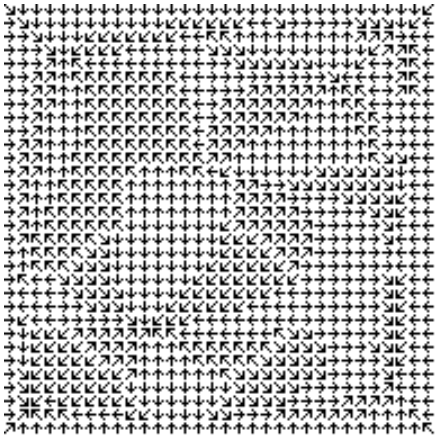

Fig. 2-61 The direction of each vector in the compressing vector field of *Test4* with border force

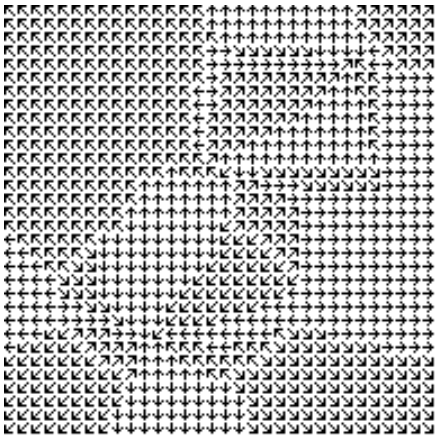

Fig. 2-62 The direction of each vector in the compressing vector field of *Test4* without border force

2.2.2.3 The extraction of region center points

The experimental results of the test images show that the compressing vectors within a homogeneous region have an overall tendency of shrinking to the region center. Therefore, if each point moves according to the vectors' directions, the homogeneous region will shrink to its center points. Thus different regions can be separated and extracted by region-shrinking. Therefore, the extraction of

center points is the first step of region extraction in the compressing vector field. The experimental results show that the center point has a unique character about its vector direction. If p_c is a center point and its vector points to p_n, p_c's vector direction is opposite to p_n's vector direction. This is the basis of center point extraction in the vector field. Fig. 2-63 shows the cases in which two vectors are of the opposite direction (supposing that **A**'s vector has the angle of zero, and it points to **B**):

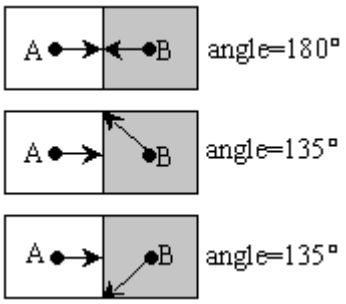

Fig. 2-63 The opposite vector directions on point A and B

If the vector of point **A** has the angle α, and **B** is the next point on **A**'s vector direction. The rotating direction can also be determined according to the angle between the two vectors on **A** and **B** as the above cases.

The center points are extracted for the test images. The experimental results are shown in Fig. 2-64 to Fig. 2-67. The center points are shown in the direction distribution of the vector field. The results indicate that there may be more than one group of center points in a homogeneous region (especially in large regions). This may cause the decomposition of a large region into smaller sub-regions in the region-shrinking process, which makes region-merging a necessary post-processing step.

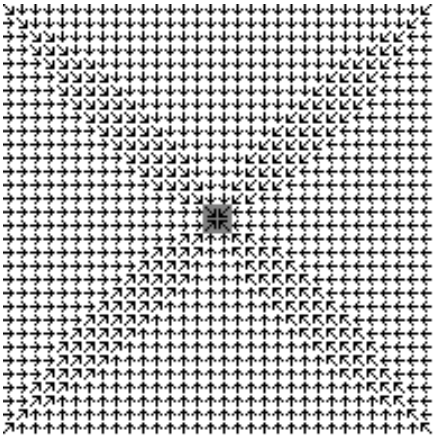

Fig. 2-64 The region center points extracted for *Test1*

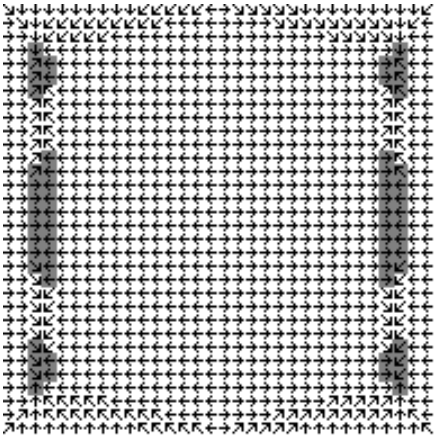

Fig. 2-65 The region center points extracted for *Test2*

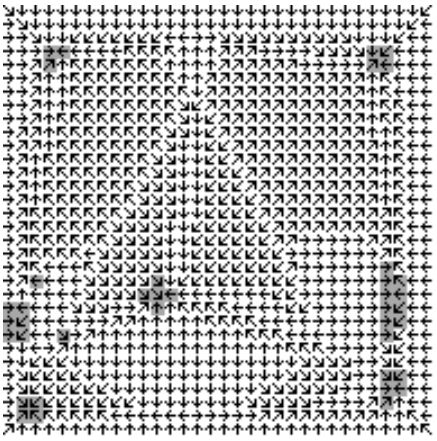

Fig. 2-66 The region center points extracted for *Test3*

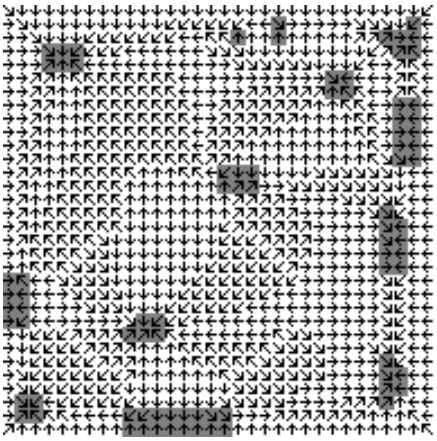

Fig. 2-67 The region center points extracted for *Test4*

2.2.2.4 The extraction of primitive regions

In the above experiments, the center points can be extracted and each group of center points corresponds to a single region in the vector field. Such regions can be taken as a kind of elements of the image, and are named the primitive regions (or primitive areas). Therefore, the primitive regions can be extracted with the center points in the compressing vector field. This process is proposed as following:

Step1: Gather adjacent center points into groups. Two neighboring center points are of the same group. Assign each group of center points a unique group number. Different group numbers represent different regions. Initially, those non-center points do not have a group number.

Step2: For each point p_i that does not have a group number, decide which group it should belong to. Take p_i as the starting point, and move to p_i's next point according to p_i's vector direction. Keep on the movement for the next point according to the vector field, until the next point has a group number n. Then p_i is assigned the same group number n. Because the directions of the vectors within a homogeneous region have the tendency of shrinking to the region center, ***Step2*** is virtually a process of region extraction by region-shrinking.

After all the image points have been assigned a group number, the region extraction is completed.

The primitive region extraction is carried out for the test images, and the experimental results are shown form Fig. 2-68 to Fig. 2-71. The experimental results show that the primitive regions can be effectively extracted by region-shrinking. Moreover, a large homogeneous region in the image may be decomposed into several primitive regions, such as the background region in Fig. 2-70 and Fig. 2-71.

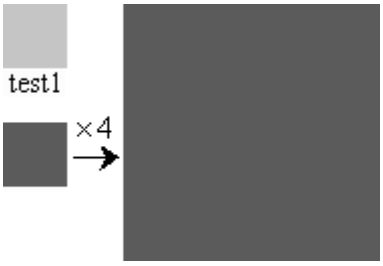

Fig. 2-68 The primitive regions extracted for *Test1*

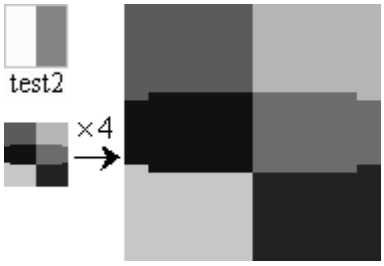

Fig. 2-69 The primitive regions extracted for *Test2*

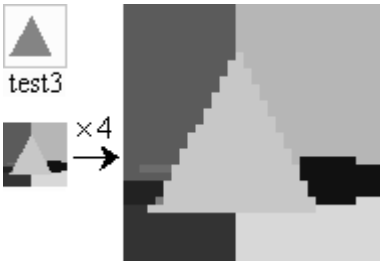

Fig. 2-70 The primitive regions extracted for *Test3*

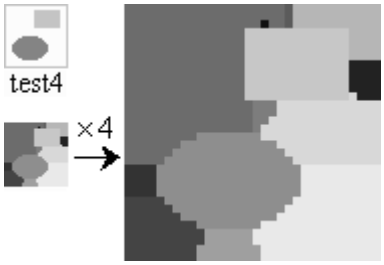

Fig. 2-71 The primitive regions extracted for *Test4*

2.2.2.5 Gray-scale image segmentation in the compressing vector field

The analysis and experimental results show that a large homogeneous region may be divided into more than one primitive region. On the other hand, the real world images are much more complex than the test images. Therefore, the real world images may have much more center points. The primitive region extraction is also carried out for a group of real world images with the size of 128×128. In the experiment results, there are 75 primitive regions in the cameraman image, 64 primitive regions in the house image, and 146 primitive regions in the heart image. To get meaningful segmentation result, the region-merging step is proposed according to a criterion of least difference of average gray-scale. First, an expected number of remaining regions after merging is given. Then the following steps are carried out to merge regions until the expected region number is reached:

Step1: For each region in the image, calculate its average gray-scale value;
Step2: Find the pair of neighboring regions with the least difference of average gray-scale, and merge them into one region;
Step3: If the current number of regions is larger than the expected value, return to ***Step1***; otherwise, end the merging process.
Based on the above sections, a method of image segmentation in the compressing vector field is proposed as following:
Step1: Calculate the image's compressing vector field;
Step2: Extract the center points;
Step3: Gather the neighboring center points into corresponding groups, and each group is assigned a group number;
Step4: Extract the primitive regions in the compressing vector field with a manner of region-shrinking;
Step5: Merge neighboring primitive regions according to the criterion of least difference of average gray-scale, and obtain the segmentation result with a pre-defined number of remaining regions.

The proposed segmentation method is applied to a group of real world images. The results of the cameraman image, the house image, and the heart image are shown in Fig. 2-72 to Fig. 2-74. The segmentation result of the cameraman image with 28 regions remained is shown in Fig. 2-72. The segmentation result of the house image with 30 regions remained is shown in Fig. 2-73. Fig. 2-74 shows the segmentation result of the heart image with 50 regions remained after merging. In the results, different regions are differentiated from each other by different gray-scale values.

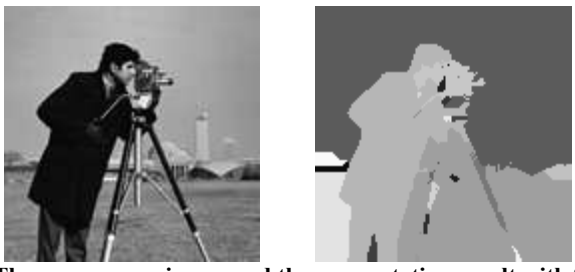

Fig. 2-72 The cameraman image and the segmentation result with 28 regions

Fig. 2-73 The house image and the segmentation result with 30 regions

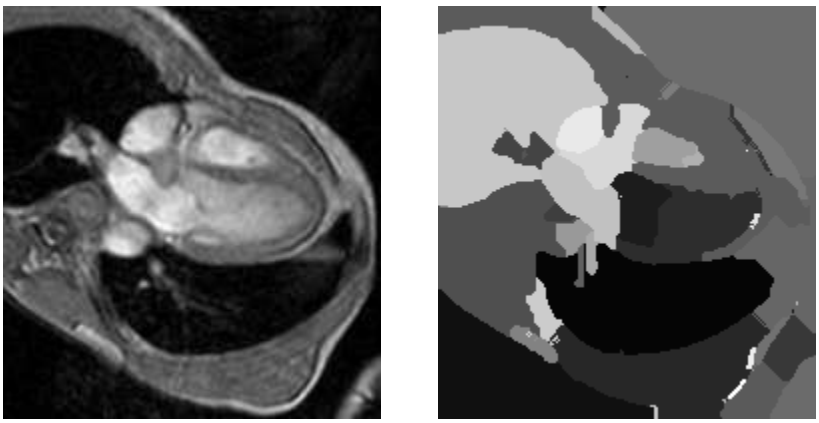

Fig. 2-74 The heart image and the segmentation result with 50 regions

The experimental results of the test images and the real world images show that the compressing vector field can represent the image structure feature, based on which effective image segmentation can be implemented.

2.3 Electro-statics inspired source reversing for gray-scale images

In physics, the field is determined by the source distribution[75-78]. This is the fundamental idea underlying the virtual field methods, which also guarantees the effectiveness of such methods. Most of the current research focuses on the virtual field generated by the image, in which the image is just taken as the field source[3,19,22,69-73]. Because the source and the field are two inseparable aspects of a physical system, the source can also serve as a compact representation of the field. In this book, to obtain novel representation and features of images, a novel image transform named "source-reverse" transform is studied by taking the image as the electro-static potential field in order to reverse the virtual source. Based on the relationship between the field and the source in physics, the virtual source by the source-reverse transform can serve as a novel representation of the image for further processing tasks.

2.3.1 The relationship between the electro-static field and the field source

In physics, the electric field intensity is virtually the inverted gradient vector of the potential [75-78]:

$$\vec{E} = -\nabla V \tag{2-21}$$

where $\vec{E}$ means the electric field intensity at a space point; V is the potential; ∇ is the Hamiltonian operator as following:

$$\nabla = \frac{\partial}{\partial x}\vec{i} + \frac{\partial}{\partial y}\vec{j} + \frac{\partial}{\partial z}\vec{k} \tag{2-22}$$

where $\vec{i}$, $\vec{j}$ and $\vec{k}$ are three base vectors in the 3D space.

Therefore, the electro-static field can be represented by either of the two equivalent forms: the form of vector field (i.e. the electric field intensity) and the form of scalar field (i.e. the electric potential). The electro-static field distribution is determined by the field source, i.e. the distribution of the charge distribution. On the other hand, the source can be reversed from the field, which is well known as the Gaussian law in differential form[75-78]:

$$div\,\vec{E} = \nabla \cdot \vec{E} = \frac{\rho}{\varepsilon_0} \tag{2-23}$$

where *div* means the divergence; ρ is the charge density at the same space point of $\vec{E}$, i.e. the distribution of the source; ε_0 is the physical constant of the vacuum permittivity. Therefore, the source distribution can be obtained by the following:

$$\rho = -\varepsilon_0 \cdot div(grad(V)) \tag{2-24}$$

where *div* and *grad* mean the divergence and gradient operation respectively. The above equation can be regarded as the reverse process from field to source. Because the source determines the distribution of the field, the distribution of the source can serve as a compact representation of the field, and

contains the field's interior structure information. Therefore, in this section a novel image transform is proposed by imitating Equation (2-24) for image structure representation and analysis.

2.3.2 The source-reverse transform for digital images

One of the ultimate goals of intelligent computer vision systems is automatic recognition of the objects in the scene. Generally speaking, different objects occupy different regions in the image. Therefore, besides the image itself, an efficient representation of image structure is important for further analysis and recognition. In this section, a novel image transform is presented based on the relationship between the field and the source, which takes the image as the field and reverse the source distribution. The properties of the source reverse transform are investigated experimentally and can be applied in further analysis and processing.

The Gauss's law in the electro-static field is for a continuous field in the space. However, the digital image is discrete on the 2D plane. Therefore, discrete operator should be used to obtain the gradient and divergence of the digital image as a potential field. Imitating the field source reverse in electro-static field, the source-reverse transform for an image $g(x,y)$ is as following:

$$F(x,y) = -div_d(grad_d\ (g(x,y))) \tag{2-25}$$

where $F(x,y)$ is the virtual field source obtained by the transform; div_d and $grad_d$ are the discrete operators to get the estimation of the divergence and the gradient respectively. It is notable that the domain of $F(x,y)$ is still the two dimensional plane where the image is defined. Therefore, the spatial properties of $F(x,y)$ may have direct relationship with the image structure.

According to Equation (2-25), the source-reverse transform for an image includes two steps as following:

Step1: Estimate the virtual field intensity $\vec{E}(x,y)$ for each image point:

$$\vec{E}(x,y) = grad_d\ (g(x,y)) \tag{2-26}$$

The operator $grad_d$ can get the two components of the discrete gradient on the x and y coordinates. To obtain the gradient vector, the two partial derivatives of $g(x,y)$ should be estimated. In this section, the Sobel operator is used to estimate the two partial derivatives, i.e. the components of gradient, which is shown in Fig. 2-75.

-1	0	1
-2	0	2
-1	0	1

The template to estimate the component on x-coordinate

1	2	1
0	0	0
-1	-2	-1

The template to estimate the component on y-coordinate

Fig. 2-75 The two templates of Sobel operator to estimate the gradient

According to the above two image templates, the components of $\vec{E}(x,y)$ are estimated as following:

$$E_x(x,y)=[g(x+1,y-1)- g(x-1,y-1)]+2[g(x+1,y)- g(x-1,y)]+[g(x+1,y+1)- g(x-1,y+1)] \tag{2-27}$$

$$E_y(x,y)=[g(x-1,y-1)- g(x-1,y+1)]+2[g(x,y-1)- g(x,y+1)]+[g(x+1,y-1)- g(x+1,y+1)] \tag{2-28}$$

where $E_x(x,y)$ and $E_y(x,y)$ are the two components of the estimated virtual field intensity.

Step2: Estimate the divergence of the virtual field intensity for each image point as the virtual field source:

$$F(x,y) = -div_d(\vec{E}(x,y)) \tag{2-29}$$

For continuous vector field on the two dimensional plane, the divergence is defined as following:

$$div\,\vec{E} = \frac{\partial E_x}{\partial x} + \frac{\partial E_y}{\partial y} \tag{2-30}$$

where E_x and E_y are the two components of the vector field.
Based on Equation (2-29), the estimation of the divergence of a discrete vector field should also use the discrete operator div_d, where the two partial derivatives in Equation (2-30) are still estimated by the Sobel operator as in **Step1**.

By the above two steps, the virtual source reverse can be implemented for a digital image which is taken as a potential field, and the virtual source is estimated as the result of the proposed image transform.

2.3.3 The virtual field source as the representation of image structure

To investigate the spatial property of the proposed source-reverse transform, experiments are carried out for a group of test images and also a group of images in real world. The principle to select proper images in the experiment is that the experimental results for simple test images may distinctly show the basic characteristics of the source-reverse transform, while the transform results for images in real world with much more complexity will reveal possible and promising applications of the method.

In the experiments, the value of the source on each point is recorded. The results indicate that there are both positive and negative values in the source. To reveal the property of the source, the source values $F(x,y)$, their absolute values $|F(x,y)|$ and the sign of each value $\mathrm{sgn}(F(x,y))$ are visualized in the form of gray-scale images. An example is shown in Fig. 2-76, which is one of the simple test images. Fig. 2-77 shows the absolute value distribution of the source, where larger gray-scale corresponds to larger absolute value. Fig. 2-78 shows the sign of the value on each point, where the white points represent positive values, the black points represent the negative values and the gray points represent the zero value. The values of $F(x,y)$ is shown by Fig. 2-79 (not absolute values but values with sign), where the larger the gray-scale the larger the value.

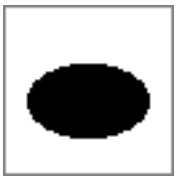

Fig. 2-76 One test image

Fig. 2-77 The distribution of the absolute values of the source

Fig. 2-78 The sign of the value on each point in the field source

Fig. 2-79 The value of each point in the field source

Fig. 2-78 shows that there are both regions of positive values and regions of negative values in the virtual field source. Fig. 2-80 and Fig. 2-81 show the borders of the positive regions and negative regions respectively, where the white points represent the border points. The experimental results show that for test images with simple objects, the borders of positive and negative regions correspond to the counters of the objects.

Fig. 2-80 The borders of the positive regions

Fig. 2-81 The borders of the negative regions

In the experimental results for simple test images, Fig. 2-78 shows that the source values in a homogeneous region are zero. Fig. 2-77, Fig. 2-78 and Fig. 2-79 show that the non-zero values in the virtual field source concentrate near the region borders. In another word, the energy in the virtual source concentrates on the borders of the homogeneous regions. This is similar to the energy concentration of the Fourier transform where the energy in the frequency domain concentrates in the area of low frequency. Moreover, Fig. 2-78 indicates that the source values on different sides of a region border are of different signs, which can be exploited in image structure representation and analysis. A group of experimental results for another test image is shown in Fig. 2-82 to Fig. 2-87, which also proves the above analysis.

Fig. 2-82 Another test image

Fig. 2-83 The distribution of the absolute values of the source

Fig. 2-84 The sign of the value on each point in the field source

Fig. 2-85 The value of each point in the field source

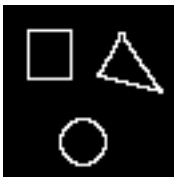

Fig. 2-86 The borders of the positive regions

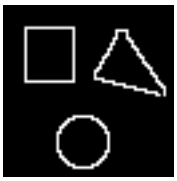

Fig. 2-87 The borders of the negative regions

In order to investigate the possible application of the source-reverse transform, experiments are also carried out for real world images. The experimental results are shown in Fig. 2-88 to Fig. 2-105 for the broadcaster image, the brain image and the house image. The experimental results for real world images also indicate the property of energy concentration and sign reverse across the region border in the virtual field source, which inspires a method of region border detection in the following section.

Fig. 2-88 The image of the broadcaster

Fig. 2-89 The distribution of the absolute values of the source

Fig. 2-90 The sign of the value on each point in the field source

Fig. 2-91 The value of each point in the field source

Fig. 2-92 The borders of the positive regions

Fig. 2-93 The borders of the negative regions

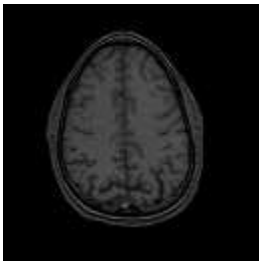

Fig. 2-94 A medical image of the brain

Fig. 2-95 The distribution of the absolute values of the source

Fig. 2-96 The sign of the value on each point in the field source

Fig. 2-97 The value of each point in the field source

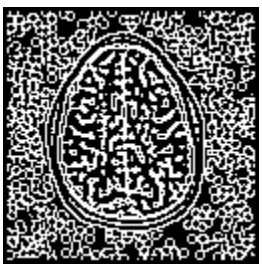

Fig. 2-98 The borders of the positive regions

Fig. 2-99 The borders of the negative regions


Fig. 2-100 The image of a house


Fig. 2-101 The distribution of the absolute values of the source


Fig. 2-102 The sign of the value on each point in the field source


Fig. 2-103 The value of each point in the field source

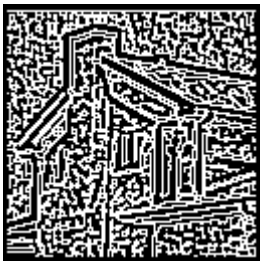
Fig. 2-104 The borders of the positive regions


Fig. 2-105 The borders of the negative regions

2.3.4 Region border detection based on the source-reverse transform

In the above experimental results, the borders of the positive and negative regions show the detail for all the regions, while minor details may not be preferred in all real world applications. Because the energy of the virtual source mainly concentrates near the border of the regions, the minor details of region borders can be eliminated with a threshold of source values (i.e. source intensity) so that the main border of interest will be preserved for further analysis. Therefore, a region border detection method is proposed based on the virtual field source as following:

Step1: Implement the source-reverse transform for the image;

Step2: Detect the points where the sign of source values reverse, i.e. find the points with different sign from neighboring points;

Step3: For the points detected in **Step2**, eliminate the points with less absolute value than the threshold.

The border detection results for real world images are shown in Fig. 2-106 to Fig. 2-111.


Fig. 2-106 The region border detected based on Fig. 2-92


Fig. 2-107 The region border detected based on Fig. 2-93

Fig. 2-108 The region border detected based on Fig. 2-98

Fig. 2-109 The region border detected based on Fig. 2-99

Fig. 2-110 The region border detected based on Fig. 2-104

Fig. 2-111 The region border detected based on Fig. 2-105

The experimental results indicate that the virtual source can be an efficient representation of image structure, based on which region border detection can be implemented.

2.3.5 The opposite transform from the virtual source to the restored image

For an image transform technique, whether it is reversible is one of the basic characteristics. Although the analysis can be carried out in the virtual source and its reversibility may not be considered for some applications, the opposite transform from the virtual source to the virtual potential field (i.e. the restored image) is discussed in this section.

For continuous electro-static field, the continuous source can be obtained by source reverse as Equation (2-24). On the other hand, the continuous potential field can also be generated by the source as following[75-78]:

$$V(x,y)=\frac{1}{4\pi\varepsilon_0}\int\frac{\rho\,dv}{r} \tag{2-31}$$

where ρ represents the charge density at a space point and r is the distance between that space point and (x,y). The integral in Equation (2-31) is carried out for the whole space where there is charge distribution. For continuous electro-static field, the transform defined by Equation (2-24) and (2-31) is reversible.

However, for digital images, the opposite transform should be implemented in a discrete form, i.e. the integral operation in Equation (2-31) should be replaced by summation as following:

$$g'(x,y)=K\cdot\sum_{j=0}^{H-1}\sum_{i=0}^{W-1}\frac{F(i,j)}{r_{(i,j)\to(x,y)}} \tag{2-32}$$

where K is a positive constant; H and W are the height and width of the image respectively. $g'(x,y)$ is the virtual potential field obtained by the opposite transform (i.e. the restored image); $F(i,j)$ is the virtual field source.

Although the transform for continuous electro-static field is theoretically reversible, the discrete source-reverse transform includes operations of discretization which will introduce some errors in the transform process. Therefore, $g'(x,y)$ is an approximation of the original image $g(x,y)$, and the source-

reverse transform for digital images is not strictly reversible. The opposite transform is implemented for real world images. The experimental results for three of the real world images are shown in Fig. 2-112 to Fig. 2-114. In each result, the left figure (a) shows the visualization of the original data of $g'(x,y)$, and the middle figure (b) shows the result of a contrast enhancement operation for $g'(x,y)$. The original image is shown in the right figure (c). The experimental results indicate that the quasi-reversible transform of source-reverse can provide an approximation of the original image by the opposite transform, which may be exploited in lossy image compression.

(a) Visualization of $f'(x,y)$ (b) Result of contrast enhancement (c) The original image

Fig. 2-112 The restored results and the original image of the peppers

(a) Visualization of $f'(x,y)$ (b) Result of contrast enhancement (c) The original image

Fig. 2-113 The restored results and the original image of the house

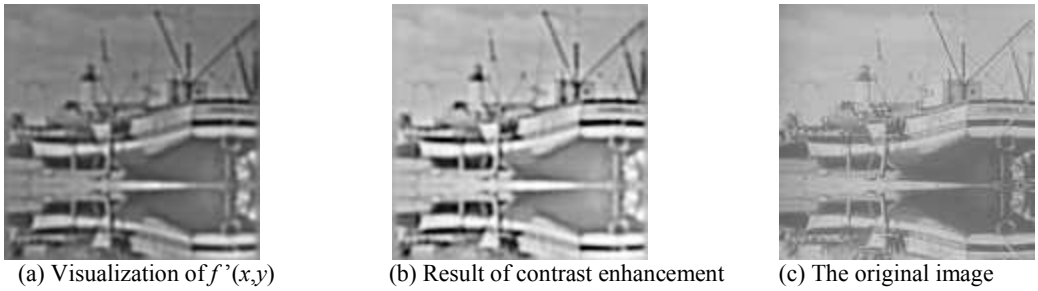

(a) Visualization of $f'(x,y)$ (b) Result of contrast enhancement (c) The original image

Fig. 2-114 The restored results and the original image of the boat

2.3.6 Data reduction of the virtual field source

The experimental results have indicated that the energy in the virtual field source concentrates near the border of the homogeneous regions, which may be exploited in lossy image compression. Because a large part of the values in the source are relatively small, experiments are carried out to investigate the effect of eliminating small source values on the restoration of the field (i.e. the image).

The experimental results are shown in Fig. 2-115 to Fig. 2-117. In the experiments, the threshold to eliminate small values in the virtual source is determined by a certain percentage of the maximum of the absolute values. For each real world image, the results show the effect of assigning 1%, 5%, 10% and 20% of the maximum absolute value to the threshold respectively. If the absolute value on a point is smaller than the threshold, that value is set to zero. Then the virtual potential field is restored

from the modified source where small source values are eliminated. The experiments show the different effect of eliminating small values in the source with increasing the threshold value. The original images are of the size 128×128. Therefore, the uncompressed virtual source has totally 16384 values. The results indicate that the subjective visual perception of the restored image is still acceptable when a large part of the values in the virtual source is reduced. But when most of the small values are eliminated, the quality of the image is unacceptable for visual perception, which is shown in (c) and (d) of each group of results. The results indicate that the source-reverse transform may have potential application in lossy image compression.

Based on the experimental results, future work will consider how to overcome the small error between the original and restored images caused by discretization in the transform process, so that the quality of the restored images will be improved. Further research will also investigate the detailed characteristics of the source-reverse transform together with its potential application in other image processing applications.

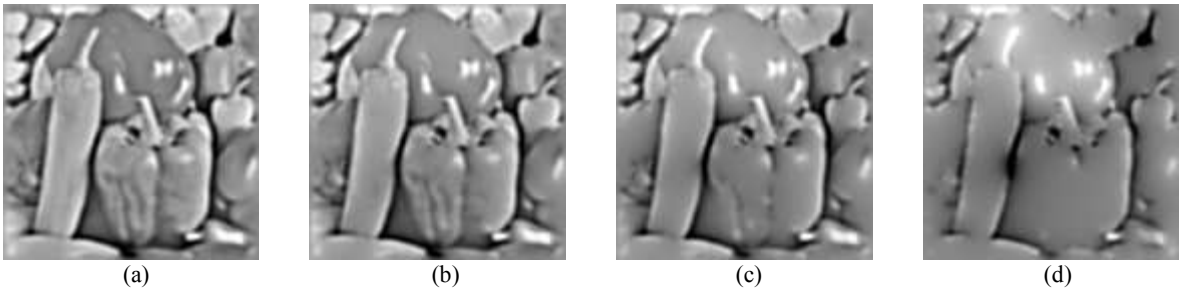

(a) (b) (c) (d)

(a) Result of restoration with the threshold defined as 1% of the maximum value; 3684 values eliminated
(b) Result of restoration with the threshold defined as 5% of the maximum value; 8969 values eliminated
(c) Result of restoration with the threshold defined as 10% of the maximum value; 11473 values eliminated
(d) Result of restoration with the threshold defined as 20% of the maximum value; 13858 values eliminated

Fig. 2-115 The effect of eliminating small source values on the restoration of the peppers image

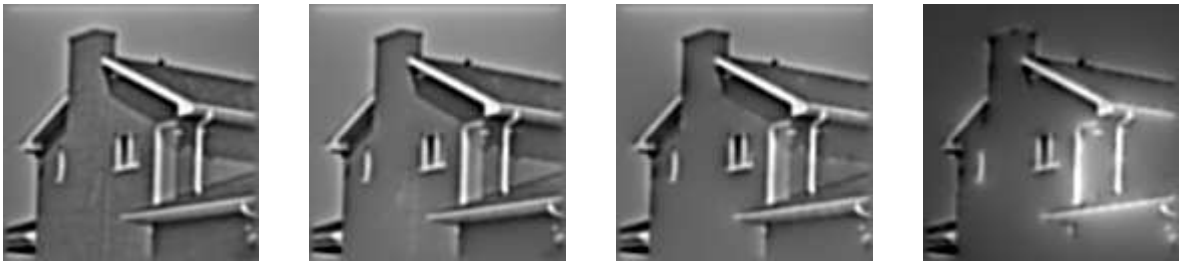

(a) (b) (c) (d)

(a) Result of restoration with the threshold defined as 1% of the maximum value; 6870 values eliminated
(b) Result of restoration with the threshold defined as 5% of the maximum value; 11347 values eliminated
(c) Result of restoration with the threshold defined as 10% of the maximum value; 12688 values eliminated
(d) Result of restoration with the threshold defined as 20% of the maximum value; 14356 values eliminated

Fig. 2-116 The effect of eliminating small source values on the restoration of the house image

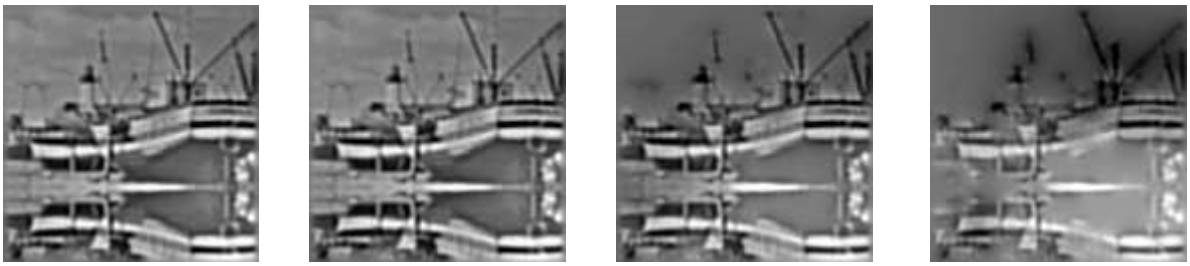

(a) (b) (c) (d)

(a) Result of restoration with the threshold defined as 1% of the maximum value; 3176 values eliminated
(b) Result of restoration with the threshold defined as 5% of the maximum value; 7526 values eliminated
(c) Result of restoration with the threshold defined as 10% of the maximum value; 9690 values eliminated
(d) Result of restoration with the threshold defined as 20% of the maximum value; 12361 values eliminated

Fig. 2-117 The effect of eliminating small source values on the restoration of the boat image

3 Magneto-Statics Inspired Methods

The electro-magnetic field in physics has a complete theoretical description (a series of laws and theorems), from which novel ideas may be borrowed for image processing and analysis. Currently, most field-inspired methods in image processing are based on the electro-static field, while those imitating the magneto-static field are much less. However, the magneto-static field has different characteristics from the electro-static field. For example, the divergence of a magneto-static field is zero. It is promising to reveal novel image features by magneto-statics inspired methods.

In this chapter, some novel image transforms are studied by taking the image as the magnetic field source. Moreover, in another proposed method the image is taken as the magneto-static field and its virtual curl source is studied. The study of magneto-statics inspired transforms shows unique transform results comparing to those inspired by electro-statics.

3.1 The virtual edge current in gray-scale images

The distinctive feature of physics-inspired methods for image analysis is a kind of natural description and representation of image structures, which may reveal novel image features for further analysis. The magnetic field generated by the stable current satisfies the Biot-Savart law[75-78], and in this section its spatial property on the 2D plane is investigated. The possible application of the magneto-static field's spatial property to region border extraction is also studied.

3.1.1 The spatial property of the magnetic field generated by stable currents

3.1.1.1 The magnetic field of the current in a straight wire and its spatial property

According to the electro-magnetic theory, the magnetic field generated by the stable current in an infinitely long straight wire is[75-78]:

$$B = \frac{\mu_0 I}{2\pi r} \tag{3-1}$$

where B is the magnitude of the magnetic induction at a space point, I is the intensity of the current, r is the distance of the space point to the straight line, μ_0 and π are two constants. The diagram of the magnetic field generated by the straight line is shown in Fig. 3-1.

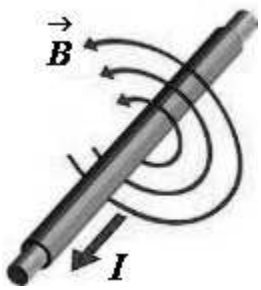

Fig. 3-1 The magnetic field generated by the straight line

In Fig. 3-1, the direction of the magnetic induction is determined by the right-hand rule: if the thumb of the right hand is pointed in the direction of the current, and the other four fingers assume a curved position, the magnetic field circling around the wire flows in the direction in which the other four fingers point[75-78]. The right-hand rule is shown in Fig. 3-2.

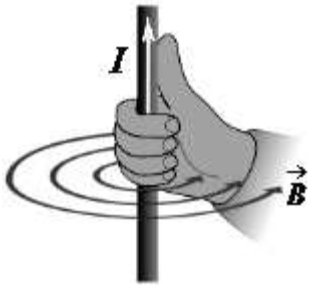

Fig. 3-2 The right-hand rule

According to the right-hand rule, the direction distribution of $\vec{B}$ can be determined on the plane where the wire lies. Fig. 3-3 shows the direction distribution of the magnetic field on the 2D plane where the straight wire lies. In Fig. 3-3 the cross represents the direction of going into the paper, and the dot represents the direction of coming out of the paper. From the viewpoint of geometry, the line divides the plane into two halves. The direction of the magnetic induction vectors in one half is just opposite to that in the other half. If the direction of I is given, based on the direction of $\vec{B}$, it can be decided on which side of the wire the point lies. Therefore, from the viewpoint of image analysis, the direction of the magnetic field can serve as a feature indicating the relative position of a point with respect to the straight wire on the plane.

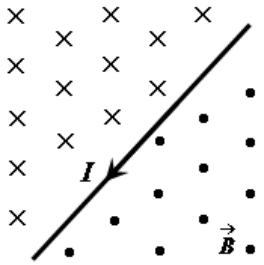

Fig. 3-3 The direction distribution of the magnetic field generated by a straight wire on a plane

3.1.1.2 The magnetic field of the current in a closed wire with arbitrary shape and its spatial property

The straight line is just a special case of curves with arbitrary shapes, and the magnetic field generated by the straight wire is a special case of those generated by general wires. A more general description of the magnetic field is given by the Biot-Savart law[75-78], where the source of the magnetic field is the current of arbitrary shapes which is composed of current elements. A current element $I\vec{dl}$ is a vector representing a very small part of the whole current, whose magnitude is the arithmetic product of I and dl (the length of a small section of the wire). The current element has the same direction as the current flow at the same point. Thus the whole magnetic field is the accumulation of those generated by all the current elements.

The magnetic field generated by a current element $I\vec{dl}$ is as following[75-78]:

$$\vec{dB} = \frac{\mu_0}{4\pi} \cdot \frac{I\vec{dl} \times \vec{r}}{r^3} \tag{3-2}$$

where $\vec{dB}$ is the magnetic induction vector at a space point, $I\vec{dl}$ is the current element, r is the distance between the space point and the current element, $\vec{r}$ is the vector from the current element to the space point, the operator $\times$ represents the cross product of the two vectors. The direction of the magnetic field also follows the right-hand rule. The magnetic field's direction distribution on the 2D

plane where the current element lies is shown in Fig. 3-4. Similar to the case of straight wire, the direction of the magnetic field reverses when crossing the line on which the current element lies.

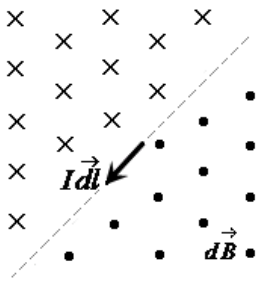

Fig. 3-4 The magnetic field's direction distribution of a current element on the 2D plane

The magnetic field generated by the current in a wire of arbitrary shape is the accumulation of the fields generated by all the current elements on the wire, which is described by the Biot-Savart law[75-78]:

$$\vec{B} = \int_D \vec{dB} = \int_D \frac{\mu_0}{4\pi} \cdot \frac{I\,\vec{dl} \times \vec{r}}{r^3} \tag{3-3}$$

where $\vec{B}$ is the magnetic induction vector at a space point generated by the whole current of arbitrary shape. D is the area where the current element exists. $\vec{dB}$ is the magnetic field generated by each current element in D.

Fig. 3-5 shows the case of a current element on a closed wire with arbitrary shape, and also its magnetic field in the small local neighboring area. The closed wire divides the plane into two parts: the inner region and the outer region of the curve. In the small local area of a current element, the magnetic field's direction reverses when crossing the local section of the curve. From the viewpoint of image analysis, the reverse of the field's direction in the local area indicates the existence of the region border (such as the curve in Fig. 3-5) Therefore, the reverse of the field direction can serve as a novel feature representing region borders in digital images, which may be exploited for further analysis.

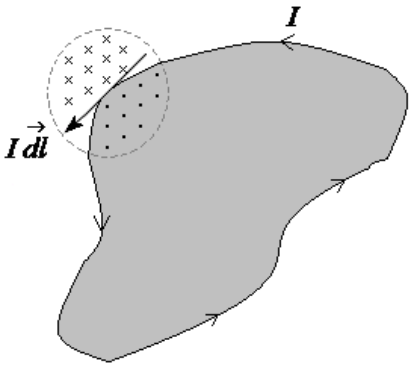

Fig. 3-5 The magnetic field distribution in the small local area of a current element on a closed wire

3.1.2 The tangent edge vector for simple image regions

The direction of the current in a wire is virtually the tangent direction of the curve at that point. On a discrete 2D plane, the discrete form of a current in a curving wire can be represented by a set of tangent vectors at each discrete point of the curve. In geometric theory, for simple regions (such as those in Fig. 3-5 and Fig. 3-6) the gradient vector on the region border is perpendicular to the border

curve. Since the direction of the curve at a point is represented by the tangent direction of the curve, the tangent vector can thus be estimated by the gradient vector in digital images.

3.1.2.1 The definition of the tangent edge vector

In this section, the tangent edge vector is proposed to represent the edge intensity and edge direction. The magnitude of a tangent edge vector $\vec{T}$ is defined as the same of the gradient vector $\vec{G}$ at that point, while its direction is perpendicular to the gradient vector:

$$T_x = G_y \tag{3-4}$$

$$T_y = -G_x \tag{3-5}$$

where T_x and T_y are the x and y components of $\vec{T}$ respectively. G_x and G_y are the x and y components of $\vec{G}$ respectively. Therefore, the magnitude of the tangent edge vector represents the edge intensity, and its direction represents that of the border curve. Fig. 3-6 shows the relationship between the gradient and tangent edge vector on the border of a simple region. Therefore, the tangent vector can be estimated by rotating the gradient vector clockwise with 90 degrees, which is shown in Fig. 3-6.

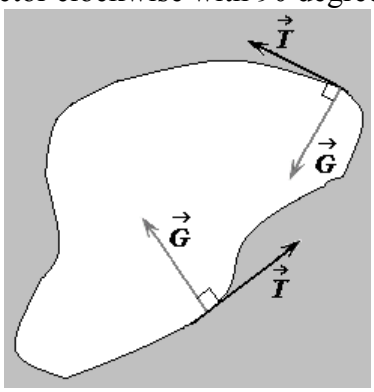

Fig. 3-6 The relationship between the tangent edge vector and the gradient vector

In this section, the Sobel operator is used to estimate the gradient vector in digital images. The two templates of the Sobel operator for gradient estimation are shown in Fig. 3-7.

-1	0	1
-2	0	2
-1	0	1

The template to estimate the gradient component on x-coordinate

1	2	1
0	0	0
-1	-2	-1

The template to estimate the gradient component on y-coordinate

Fig. 3-7 The two templates of the Sobel operator to estimate the gradient vector

According to the Sobel operator, for digital image $f(x,y)$, the two components of the gradient vector are estimated as following:

$$G_x(x,y)=[f(x+1,y-1)-f(x-1,y-1)]+2[f(x+1,y)-f(x-1,y)]+[f(x+1,y+1)-f(x-1,y+1)] \tag{3-6}$$

$$G_y(x,y)=-[f(x-1,y+1)-f(x-1,y-1)]-2[f(x,y+1)-f(x,y-1)]-[f(x+1,y+1)-f(x+1,y-1)] \tag{3-7}$$

where $G_x(x,y)$ and $G_y(x,y)$ are the two components of the gradient vector on the x and y direction respectively. Then the tangent edge vector can be estimated based on the gradient vector according to Equation (3-4) and (3-5).

3.1.2.2 The spatial property of the virtual magnetic field generated by the set of tangent edge vectors

To investigate the properties of the tangent edge vector, experiments are carried out for a group of simple test images. The original images are shown in Fig. 3-8(a) to Fig. 3-12(a). The test images are of the size 32×32, which contain simple image regions. To get a more clear view, the original images are shown in both original size and the size of 4 times larger. The tangent edge vectors are shown in Fig. 3-8(b) to Fig. 3-12(b), where the arrows indicate the directions of the tangent edge vectors and the dot indicates zero vectors.

For the simple test images in the experiments, each region has homogeneous pixels of the same gray-scale. Therefore, the gradient vectors are zero except on the points near the region border. Thus the tangent edge vectors also gather near the border curve and forms a circulating current around the region. Therefore, the tangent edge vectors make up a virtual current of a discrete form in the image. Because the physical current elements are also along the tangent direction of the wire curve, the tangent edge vector is a natural analogy to the physical current element. The experimental results shown in Fig. 3-8(b) to Fig. 3-12(b) also indicate that the tangent edge vectors form a virtual current in a discrete form along the region border, which is later defined as the virtual edge current in the following section.

To further investigate the tangent edge vector, the virtual magnetic field generated by the tangent edge vectors is calculated. Imitating the physical current element, the discrete virtual magnetic field generated by a tangent edge vector on point (i,j) is proposed as following:

$$\vec{B}_{(i,j)}(x,y)=\frac{\vec{T}(i,j)\times\vec{r}_{(i,j)\to(x,y)}}{r^3_{(i,j)\to(x,y)}} \tag{3-8}$$

where $\vec{B}_{(i,j)}(x,y)$ is the virtual magnetic induction on point $(x\ ,y)$ generated by $\vec{T}(i,j)$, and $\vec{T}(i,j)$ is the tangent edge vector on point (i,j). $\vec{r}_{(i,j)\to(x,y)}$ is the vector from (i,j) to (x,y), and $r_{(i,j)\to(x,y)}$ is the distance between (i,j) and (x,y).

Therefore, the virtual magnetic field generated by all the tangent edge vectors is defined as the accumulation of $\vec{B}_{(i,j)}(x,y)$:

$$\vec{B}(x,y)=\sum_{\substack{j=0\\(j\neq y\ \text{or}\ i\neq x)}}^{H-1}\sum_{i=0}^{W-1}\vec{B}_{(i,j)}(x,y)=\sum_{\substack{j=0\\(j\neq y\ \text{or}\ i\neq x)}}^{H-1}\sum_{i=0}^{W-1}\frac{\vec{T}(i,j)\times\vec{r}_{(i,j)\to(x,y)}}{r^3_{(i,j)\to(x,y)}} \tag{3-9}$$

where H and W represents the height and width of the digital image respectively. Because each tangent edge vector generates a magnetic field separating the image points on different sides of the local border section, the accumulation of such virtual magnetic fields generated by all the tangent edge vectors may separate the image points into two classes: those within the region and those outside the region. The experimental results of simulation are also shown in visible figures. The magnitude of each virtual magnetic field is shown in Fig. 3-8(c) to Fig. 3-12(c), where larger gray-scale values represent larger magnitude of $\vec{B}(x,y)$. The direction distribution of each virtual magnetic field is shown in Fig. 3-8(d) to Fig. 3-12(d), where the white points represent the direction of going into the paper, and the black points represent the direction of coming out of the paper. The results indicate that different adjacent regions have different directions of the virtual magnetic field, and the field direction reverses when crossing the region orders. Therefore, the direction distribution in the virtual magnetic field can serve as a promising feature for region border detection and image segmentation.

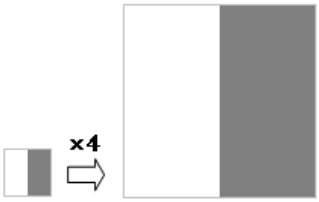

Fig. 3-8(a) The *test*1 image (4 times of original size on the right)

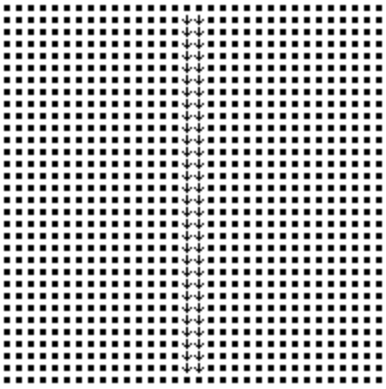

Fig. 3-8(b) The direction distribution of the tangent edge vectors

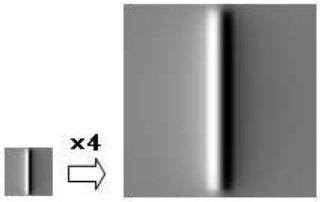

Fig. 3-8(c) The magnitude distribution of the magnetic field generated by the set of tangent edge vectors (larger gray-scale values represent larger magnitude)

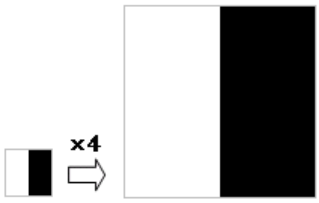

Fig. 3-8(d) The direction distribution of the magnetic field generated by the set of tangent edge vectors (the white points represent the direction of going into the paper, and the black points represent the opposite)

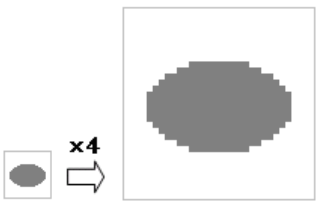

Fig. 3-9(a) The *test*2 image (4 times of original size on the right)

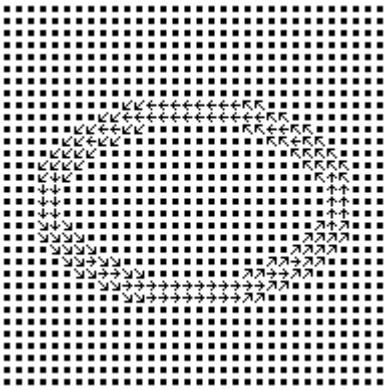

Fig. 3-9(b) The direction distribution of the tangent edge vectors

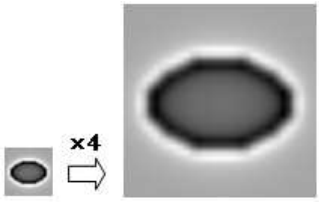

Fig. 3-9(c) The magnitude distribution of the magnetic field generated by the set of tangent edge vectors (larger gray-scale values represent larger magnitude)

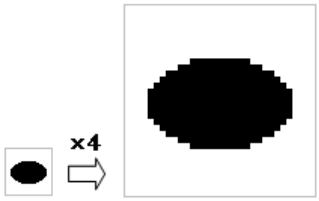

Fig. 3-9(d) The direction distribution of the magnetic field generated by the set of tangent edge vectors (the white points represent the direction of going into the paper, and the black points represent the opposite)

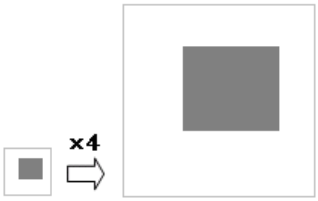

Fig. 3-10(a) The *test*3 image (4 times of original size on the right)

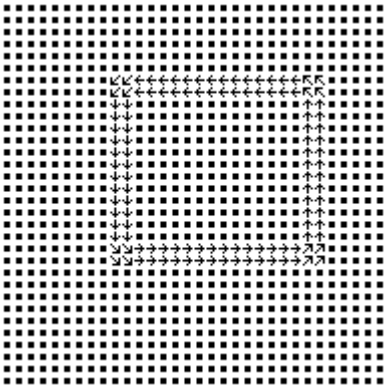

Fig. 3-10(b) The direction distribution of the tangent edge vectors

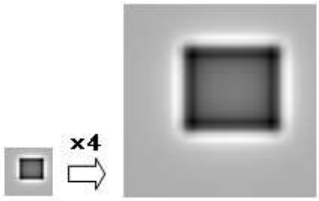

Fig. 3-10(c) The magnitude distribution of the magnetic field generated by the set of tangent edge vectors (larger gray-scale values represent larger magnitude)

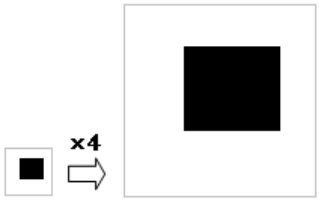

Fig. 3-10(d) The direction distribution of the magnetic field generated by the set of tangent edge vectors (the white points represent the direction of going into the paper, and the black points represent the opposite)

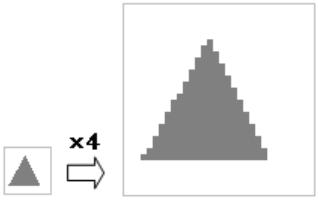

Fig. 3-11(a) The *test*4 image (4 times of original size on the right)

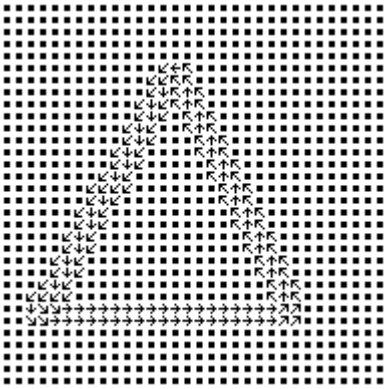

Fig. 3-11(b) The direction distribution of the tangent edge vectors

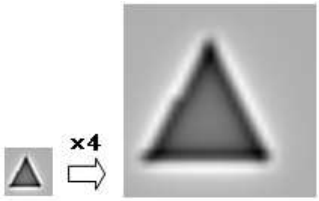

Fig. 3-11(c) The magnitude distribution of the magnetic field generated by the set of tangent edge vectors (larger gray-scale values represent larger magnitude)

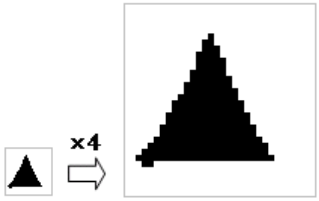

Fig. 3-11(d) The direction distribution of the magnetic field generated by the set of tangent edge vectors (the white points represent the direction of going into the paper, and the black points represent the opposite)

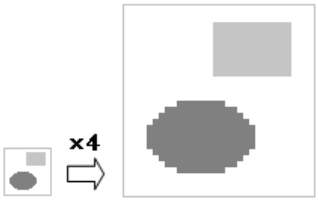

Fig. 3-12(a) The *test*5 image (4 times of original size on the right)

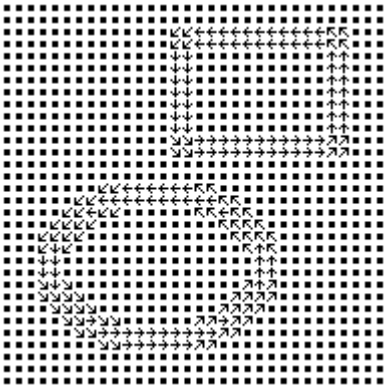

Fig. 3-12(b) The direction distribution of the tangent edge vectors

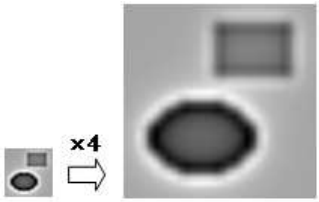

Fig. 3-12(c) The magnitude distribution of the magnetic field generated by the set of tangent edge vectors (larger gray-scale values represent larger magnitude)

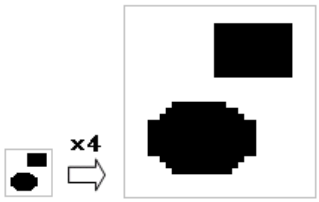

Fig. 3-12(d) The direction distribution of the magnetic field generated by the set of tangent edge vectors (the white points represent the direction of going into the paper, and the black points represent the opposite)

3.1.3 The virtual edge current in digital images

The images captured in nature (such as photos, satellite images, etc.) have rich gray-scale levels and details, and are much more complex than the simple test images. The digital image can be regarded as a function $f(x,y)$, whose arguments are the position (x,y) on the 2D plane, and the function value is the gray-scale of that image point. The isolines (contour lines) in the image $f(x,y)$ indicate possible region

borders, and in mathematics the gradient vector is perpendicular to the isoline of $f(x,y)$. Consequently, for complex natural images, the tangent edge vector represents the direction of the isoline, i.e. the direction of possible region border curve. On the other hand, since the magnitude of the tangent vector is the same as the gradient vector on that point, its magnitude also indicates the edge intensity at that point. Therefore, the definition of Equation (3-4) and (3-5) can also apply to complex natural images. For complex natural images, there may be rich gray-scale levels, and there is a tangent edge vector with some magnitude at each image point. All the tangent edge vectors make up a flow field, and the flow direction at each image point is just the same as that of the tangent edge vector. Therefore, all the tangent edge vectors in a digital image form a virtual current, where the tangent edge vector at each image point serves as the discrete current element. Such virtual current is defined as the virtual edge current, because all the tangent edge vectors are along the direction of the isoline curve (possible region borders) in the image.

To investigate the properties of the virtual edge current, the virtual magnetic field generated by the virtual edge current is calculated. Experiments are carried out for a group of natural images. The original images are shown in Fig. 3-13(a) to Fig. 3-19(a). The results of the virtual magnetic field are visualized as gray-scale images. The magnitude of each virtual magnetic field is shown in Fig. 3-13(b) to Fig. 3-19(b), where larger gray-scale values represent larger magnitude of the virtual magnetic induction $\vec{B}(x,y)$. The direction distribution of each virtual magnetic field is shown in Fig. 3-13(c) to Fig. 3-19(c), where the white points represent the direction of going into the paper, and the black points represent the direction of coming out of the paper. The experimental results indicate that for natural images the direction of the virtual magnetic field reverses when crossing region borders. Therefore, the distribution of the virtual magnetic field can serve as the basis of border detection and region segmentation.

(a) The peppers image

(b) The magnitude distribution of the virtual magnetic field generated by the edge current

(c) The directions distribution of the virtual magnetic field generated by the edge current

Fig. 3-13 The virtual magnetic field generated by the edge current for the peppers image

(a) The broadcaster image

(b) The magnitude distribution of the virtual magnetic field generated by the edge current

(c) The directions distribution of the virtual magnetic field generated by the edge current

Fig. 3-14 The virtual magnetic field generated by the edge current for the broadcaster image

(a) The boat image

(b) The magnitude distribution of the virtual magnetic field generated by the edge current

(c) The directions distribution of the virtual magnetic field generated by the edge current

Fig. 3-15 The virtual magnetic field generated by the edge current for the boat image

(a) The cameraman image

(b) The magnitude distribution of the virtual magnetic field generated by the edge current

(c) The directions distribution of the virtual magnetic field generated by the edge current

Fig. 3-16 The virtual magnetic field generated by the edge current for the cameraman image

(a) The house image

(b) The magnitude distribution of the virtual magnetic field generated by the edge current

(c) The directions distribution of the virtual magnetic field generated by the edge current

Fig. 3-17 The virtual magnetic field generated by the edge current for the house image

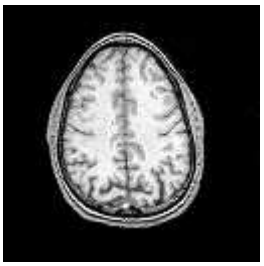

(a) The medical image of a brain

(b) The magnitude distribution of the virtual magnetic field generated by the edge current

(c) The directions distribution of the virtual magnetic field generated by the edge current

Fig. 3-18 The virtual magnetic field generated by the edge current for the brain image

(a) The medical image of a heart

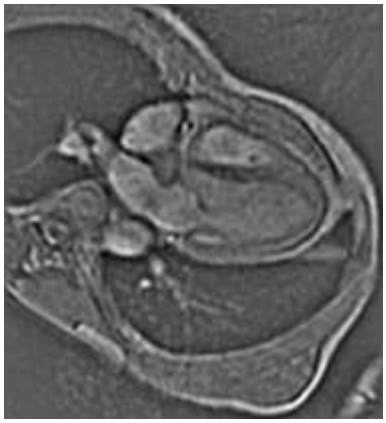

(b) The magnitude distribution of the virtual magnetic field generated by the edge current

(c) The directions distribution of the virtual magnetic field generated by the edge current

Fig. 3-19 The virtual magnetic field generated by the edge current for the heart image

Because the magnitude of the tangent edge vector is the same as the gradient vector, in Equation (3-9) the $\vec{T}$ vectors with large magnitudes have major affect on the formation of overall region borders, while those with small magnitudes can only have effect within adjacent local areas and affect the details of the local region borders. In Fig. 3-13(c) to Fig. 3-19(c), the experimental results indicate that the region borders can be detected according to the direction distribution of the virtual magnetic field generated by the virtual edge current.

3.1.4 Image segmentation based on the virtual edge current

In the experimental results for the test images, it is shown that the directions of the virtual magnetic field are opposite in two different adjacent regions. This provides a basis of region division in images. In this section, a method of image region division in the virtual magnetic field generated by the edge current is proposed as following:

***Step*1**: Calculate the tangent edge vectors to obtain the virtual edge current;
***Step*2**: Calculate the virtual magnetic field generated by the virtual edge current;
***Step*3**: Obtain the direction distribution of the virtual magnetic field;
***Step*4**: Group the adjacent points with the same direction of virtual magnetic field into connected regions. The obtained set of connected regions is the result of region division for the gray-scale image.

Real world images consist of more complex region components than simple test images. To investigate the effect of the above region division method on real world images, experiments are carried out for a group of real world images. The experimental results are shown from Fig. 3-20(b) to Fig. 3-26(b), which are the region division results of Fig. 3-13(c) to Fig. 3-19(c) respectively. In Fig. 3-20(b) to Fig. 3-26(b), different regions are represented by different gray-scale values. The results indicate that for real world images the region division method may obtain large amount of regions in the image. The numbers of regions obtained for the real world images in the experiments are shown in Table 3-1.

Table 3-1 The numbers of regions obtained for the real world images

Image	*Number of regions*
peppers	87
broadcaster	77
boat	149
cameraman	142
house	117
brain	131
heart	342

The region division results of real world images consist of large amount of regions due to the complexity of real world images. To obtain practically useful segmentation result, a region merging method is proposed based on the gray-scale similarity of adjacent regions. First, an expected number of remaining regions after merging is given (usually by trail). Then the following steps are carried out to merge regions until the expected region number is reached:

***Step*1**: For each region in the image, calculate its average gray-scale value.
***Step*2**: Find the pair of neighboring regions with the least difference of the average gray-scale, and merge them into one region.
***Step*3**: If current region number is larger than the expected region number, return to ***Step*1**; otherwise, end the merging process.

The region merging results for the real world images are shown in Fig. 3-20(c) to Fig. 3-26(c), where different regions are represented by different gray-scale. Fig. 3-20(c) to Fig. 3-26(c) show the merging results for Fig. 3-20(b) to Fig. 3-26(b) respectively.

Fig. 3-20(a)
The peppers image

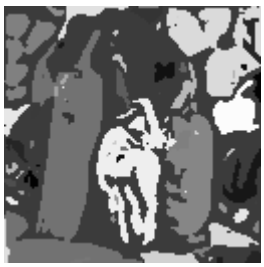

Fig. 3-20(b) The region division result based on Fig. 3-13(c)

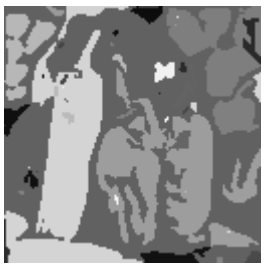

Fig. 3-20(c) The region merging result for Fig. 3-20(b) (50 regions remained)

Fig. 3-21(a)
The broadcaster Image

Fig. 3-21(b) The region division result based on Fig. 3-14(c)

Fig. 3-21(c) The region merging result for Fig. 3-21(b) (20 regions remained)

Fig. 3-22(a)
The boat image

Fig. 3-22(b) The region division result based on Fig. 3-15(c)

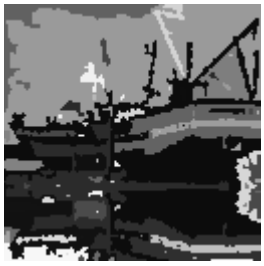

Fig. 3-22(c) The region merging result for Fig. 3-22(b) (80 regions remained)

Fig. 3-23(a)
The cameraman Image

Fig. 3-23(b) The region division result based on Fig. 3-16(c)

Fig. 3-23(c) The region merging result for Fig. 3-23(b) (20 regions remained)

Fig. 3-24(a)
The house image

Fig. 3-24(b) The region division result based on Fig. 3-17(c)

Fig. 3-24(c) The region merging result for Fig. 3-24(b) (20 regions remained)

Fig. 3-25(a) The medical image of a brain

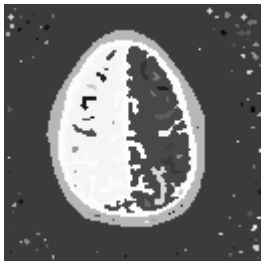

Fig. 3-25(b) The region division result based on Fig. 3-18(c)

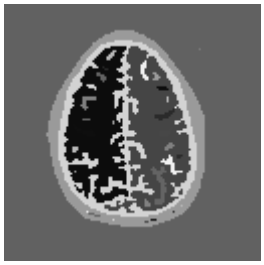

Fig. 3-25(c) The region merging result for Fig. 3-25(b) (40 regions remained)

Fig. 3-26(a) The medical image of a heart

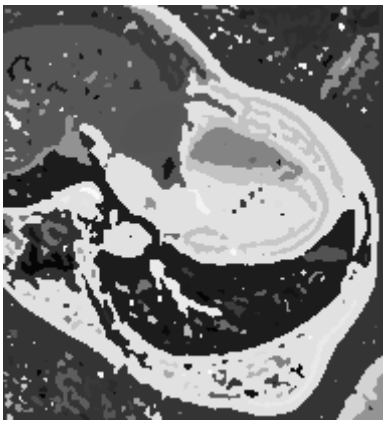

Fig. 3-26(b) The region division result based on Fig. 3-19(c)

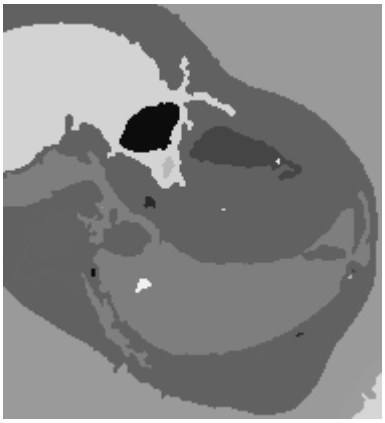

Fig. 3-26(c) The region merging result for Fig. 3-26(b) (20 regions remained)

Based on the above study, a novel image segmentation method is proposed with the virtual magnetic field generated by the virtual edge current:
***Step*1**: Calculate the tangent edge vectors in the image to form the virtual edge current;
***Step*2**: Calculate the virtual magnetic field generated by the virtual edge current;
***Step*3**: Carry out the region division based on the direction distribution of the virtual magnetic field;
***Step*4**: Merge the region division result to a pre-defined number of regions.

The experimental results have proved the effectiveness of the proposed segmentation method.

3.1.5 The influence of different edge intensity thresholds on border formation

The gradient magnitude is the intensity of gray-scale changing, which is a natural measurement of the possibility of edge existence. It can be seen from Fig. 3-13(c) to Fig. 3-19(c) that the region borders can be determined by the direction distribution of the virtual magnetic field. In the experimental results, the whole field of $\vec{B}(x, y)$ is formed by the accumulation of all the tangent edge vectors with various magnitudes. Those tangent edge vectors with relatively large magnitudes have major affect on the formation of main region borders. Experiments have been carried out to investigate the effect of different vector magnitude on the formation of region borders. In the experiments, before the calculation of the virtual magnetic field, the tangent edge vectors with magnitudes less than a pre-defined threshold are set to zero; then the virtual magnetic field is formed by the remained vectors with relatively larger magnitudes. In the experiments, the threshold is defined as a certain percent of the maximum magnitude of the tangent edge vectors. The experimental results for the broadcaster image are shown in Fig. 3-27(a) to Fig. 3-27(e). Fig. 3-27(a) to Fig. 3-27(e) show the magnitude of the obtained virtual magnetic field, where larger gray-scale values represent larger magnitude of

$\vec{B}(x, y)$. Fig. 3-27(a) to Fig. 3-27(e) also show the direction distribution of the virtual magnetic field, where the white points represent the direction of going into the paper, and the black points represent the direction of coming out of the paper. The threshold values are set as 0%, 0.05%, 0.1%, 0.2% and 0.5% of the maximum gradient magnitude in the image respectively.


the magnitude distribution


the direction distribution

Fig. 3-27(a) The magnitude distribution and direction distribution of the magnetic field generated by the virtual edge current with 0% of the maximum vector length as the threshold


the magnitude distribution


the direction distribution

Fig. 3-27(b) The magnitude distribution and direction distribution of the magnetic field generated by the virtual edge current with 0.05% of the maximum vector length as the threshold


the magnitude distribution


the direction distribution

Fig. 3-27(c) The magnitude distribution and direction distribution of the magnetic field generated by the virtual edge current with 0.1% of the maximum vector length as the threshold


the magnitude distribution


the direction distribution

Fig. 3-27(d) The magnitude distribution and direction distribution of the magnetic field generated by the virtual edge current with 0.2% of the maximum vector length as the threshold

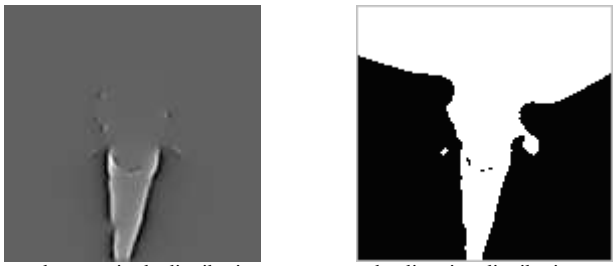

the magnitude distribution the direction distribution

Fig. 3-27(e) The magnitude distribution and direction distribution of the magnetic field generated by the virtual edge current with 0.5% of the maximum vector length as the threshold

Fig. 3-27(a) and Fig. 3-27(b) indicate that the tangent edge vectors of small magnitudes have important effect on local region details, which generates many small region borders in the direction distribution. With the threshold value increasing, small region borders become less. Fig. 3-27(c) shows a nice balance of border accuracy and the degree of detail. When the threshold becomes too large, there is obvious lost of the border accuracy, which is indicated by Fig. 3-27(d) and Fig. 3-27(e). The magnitude threshold for the tangent edge vectors can be adjusted experimentally for different requirement of detail level.

The direction distribution of the discrete magnetic field generated by the virtual edge current is experimentally proved to be a novel feature for border detection and region division, based on which image segmentation can be implemented in the virtual magnetic field. Further work will investigate the application of the virtual edge current in other image processing tasks.

3.2 The curling vector field transform of gray-scale images

The magnetic induction generated by an electric current element is defined by the Biot-Savart Law in Equation (3-2). In the physical magnetic field, the magnetic induction lines are close loops. The geometric shape of the magnetic induction lines are determined by the mathematical form of the vector field defined in Equation (3-2). In this section, the mathematical form of the magnetic field is imitated in a novel image vector transform, which is named the curling vector field.

3.2.1 The definition of the curling vector

If the image is taken as the field source, the vector field can be generated by the imitation of the magnetic field. Suppose there is an electric current element at each image point, which is at a right angle to the image plane. Then the virtual field source will generate a vector field on the image plane. Furthermore, in order to extract the image structure information, the intensity of the vector field at each point is determined by the gray-scale values of related image points. In this section, to reflect the gray-scale difference between the points in two different regions, the vector generated by point (i,j) at point (x,y) is related to the gray-scale difference between the two points:

$$\vec{V} = \frac{|g(i,j) - g(x,y)|}{r^2_{(i,j)\to(x,y)}} \cdot \frac{\vec{n}_0 \times \vec{r}_{(i,j)\to(x,y)}}{r_{(i,j)\to(x,y)}} \tag{3-10}$$

where $\vec{V}$ is the vector generated by point (i,j) on the point (x,y). $g(i,j)$ and $g(x,y)$ are the gray-scale values of the two points. n_0 is the unit vector at a right angle to the image plane. $\vec{r}_{(i,j)\to(x,y)}$ is the radius vector from (i,j) to (x,y).

The two components of V on x and y directions are:

$$V_x = \frac{|g(i,j)-g(x,y)|}{r^2_{(i,j)\to(x,y)}} \cdot \sin\theta_{(i,j)\to(x,y)} \tag{3-11}$$

$$V_y = \frac{|g(i,j)-g(x,y)|}{r^2_{(i,j)\to(x,y)}} \cdot \cos\theta_{(i,j)\to(x,y)} \tag{3-12}$$

where θ is the direction angle of the radius vector $\vec{r}_{(i,j)\to(x,y)}$.

Therefore, if two image points are of the same gray-scale, the vector generated by one point on the other is a zero vector. Only if there is gray-scale difference between two image points, non-zero vector can be generated by one point on the other. According to the above definition, the vector generated by one point on another reflects the information of their gray-scale difference and their relative position (i.e. the relative distance and direction).

3.2.2 The definition of the curling vector field transform

Based on the definition of the curling vector, the curling vector field transform is proposed as follows. The transform of image *g* on the point (*x*,*y*) is defined as the sum of the curling vectors generated by all the other image points on (*x*,*y*):

$$\vec{V}(x,y) = \sum_{\substack{j=0 \\ (j\neq y \text{ or } i\neq x)}}^{H-1}\sum_{i=0}^{W-1} \frac{|g(i,j)-g(x,y)|}{r^2_{(i,j)\to(x,y)}} \cdot \frac{\vec{n}_0 \times \vec{r}_{(i,j)\to(x,y)}}{r_{(i,j)\to(x,y)}} \tag{3-13}$$

where $\vec{V}(x,y)$ is the field vector on (*x*,*y*); *W* and *H* are the width and height of the image respectively. The two components of $\vec{V}(x,y)$ on *x* and *y* directions are:

$$V_x(x,y) = \sum_{\substack{j=0 \\ (j\neq y \text{ or } i\neq x)}}^{H-1}\sum_{i=0}^{W-1} \frac{|g(i,j)-g(x,y)|}{r^2_{(i,j)\to(x,y)}} \cdot \sin\theta_{(i,j)\to(x,y)} \tag{3-14}$$

$$V_y(x,y) = \sum_{\substack{j=0 \\ (j\neq y \text{ or } i\neq x)}}^{H-1}\sum_{i=0}^{W-1} \frac{|g(i,j)-g(x,y)|}{r^2_{(i,j)\to(x,y)}} \cdot \cos\theta_{(i,j)\to(x,y)} \tag{3-15}$$

According to the above definition, the curling vector field belongs to the kind of "relative field", which introduces the pixel difference into the field definition. The magnetic induction lines are close curves in physical magnetic field. This feature also exits in the curling vector field defined above. The curling vector transform is implemented for a group of test images to investigate the properties of the vector field. The test images are of the size 32×32. The experimental results show that the vectors inside each homogeneous region constitute a rotating whorl, which inspires the name of "curling vector field". Three representative images of the test images and the corresponding experimental results are shown in Fig. 3-28 to Fig. 3-35.

Test1 is a homogeneous area as a whole. Therefore, the vectors in the transformed field are all zero vectors.

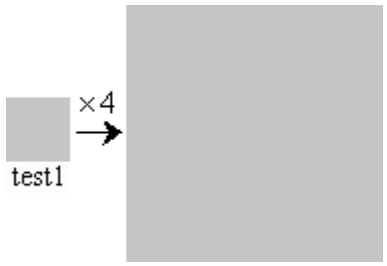

Fig. 3-28 The first image *test1* (the original image, and 4 times of original size on the right)

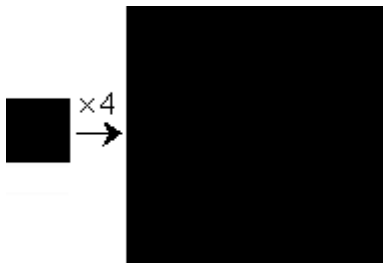

Fig.29 The vector length in the curling vector field of *test1*
(the original image; 4 times of original size on the right)

Test2 contains a rectangle region. In the vector field of *Test2*, the vectors in the rectangle region rotate clockwise, but the vectors in the background region rotate anti-clockwise.

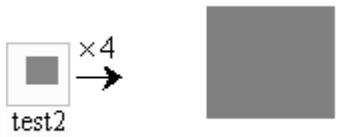

Fig. 3-30 The second image *test2* (the original image on the left, and 4 times of original size on the right)

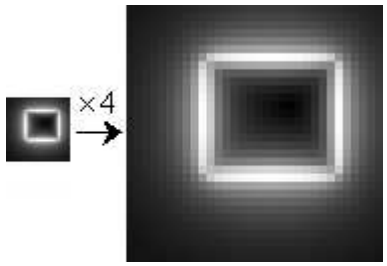

Fig. 3-31 The vector length in the curling vector field of *test2* (the original image; 4 times of original size on the right)

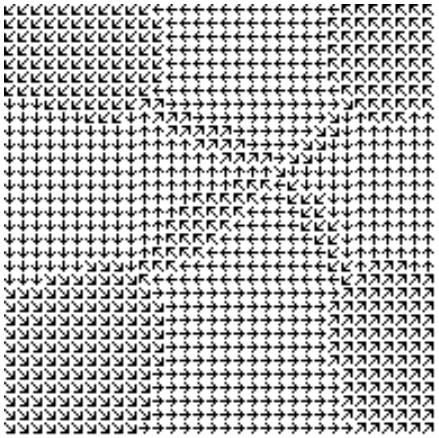

Fig. 3-32 The direction of each vector in the curling vector field of *test2*

There is a rectangle region and an ellipse region in *Test3*. In the vector field of *Test3*, the vectors in the rectangle region and the ellipse region rotate clockwise, but the vectors in the background region rotate anti-clockwise. The difference of rotating direction between the object regions and the background region is the base of segmentation in the curling vector field.

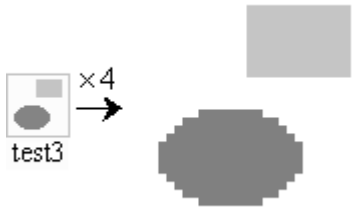

Fig. 3-33 The third image *test3* (the original image on the left, and 4 times of original size on the right)

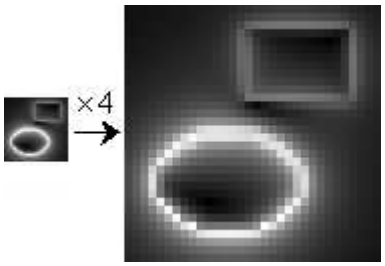

Fig. 3-34 The vector length in the curling vector field of *test3* (the original image; 4 times of original size on the right)

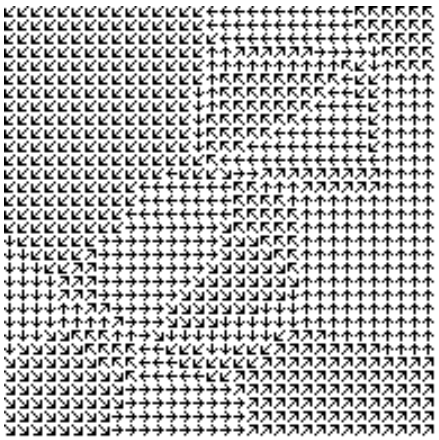

Fig. 3-35 The direction of each vector in the curling vector field of *test3*

3.2.3 Image segmentation in the curling vector field

3.2.3.1 The rotating direction and base points of rotating expansion

The experiments and analysis about the curling vector field show that the vectors inside a homogeneous region have the overall appearance of a rotating whorl. Moreover, if one region contains another, the rotating directions of them are opposite. This feature is determined by the definition of the vector field in Equation (3-13). Based on the rotating feature of the vectors inside homogeneous regions, any homogeneous region can be extracted by a kind of rotating expansion in the region. In the process of rotating expansion, the points with definite rotating directions in a region are the starting points of the expansion. The region will be extracted by continuously expanding with a form of rotating movement according to the rotating direction of the starting points. In such rotating

movement, the paths of movement will progressively cover the whole region. Thus each homogeneous region can be extracted.

Therefore, determining the rotating direction of each image point is the first step of region extraction in the curling vector field. In this section, three kinds of rotating status of an image point are given as following. First, the vector directions are discretized into eight directions. Suppose that the vector direction on point **A** has the angle of zero, and **B** is the next point on **A**'s vector direction. The rotating direction on **A** is defined according to the angle between the vectors on **A** and **B**. The clockwise rotating direction on point **A** is defined as the following two cases:

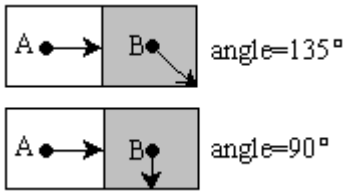

Fig. 3-36 The clockwise rotating direction on point A

The anti-clockwise rotating direction on point **A** is defined as the following two cases:

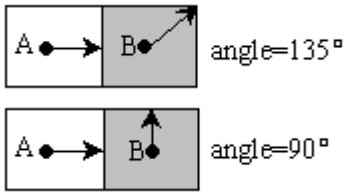

Fig. 3-37 The anti-clockwise rotating direction on point A

The uncertain rotating direction on point **A** is defined as the following four cases:

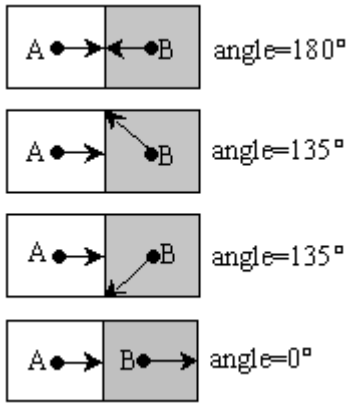

Fig. 3-38 The uncertain rotating direction on point A

If the vector on point **A** has the angle α, and **B** is the next point on **A**'s vector direction. The rotating direction can also be determined according to the angle between the two vectors on **A** and **B** as the above cases.

Therefore, the image points can be divided into two classes: one with definite rotating direction and the other with uncertain rotating direction. Those with definite rotate directions are the starting points of rotating expansion, which are named the "base points" of rotating expansion.

The base point extraction is carried out for the test images. The experimental results are shown in Fig. 3-39 to Fig. 3-42. In Fig. 3-39 and Fig. 3-42, the white points represent the anti-clockwise rotating direction, the black points represent the clockwise rotating direction, and the gray points

represent the uncertain ones. Because the vectors in the field of *Test1* are zero, there is no base extracted. Fig. 3-39 and Fig. 3-41 show the base points of *Test2* and *Test3* respectively. For a clearer view, the base points extracted are also shown in the discrete direction distribution of the vector fields as Fig. 3-40 and Fig. 3-42. The results of base point extraction indicate that these points form a kind of image structure representation, and can be the starting points for region extraction.

On the other hand, the results also indicate that there may be more than one group of base points in a single homogeneous region, especially in a large region of the image. This may cause the decomposition of a large region into smaller sub-regions in the region extraction process, and makes region-merging as a necessary post-processing step.

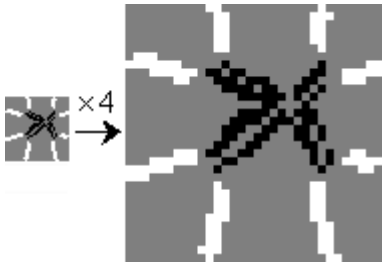

Fig. 3-39 The base points extracted for *Test2*

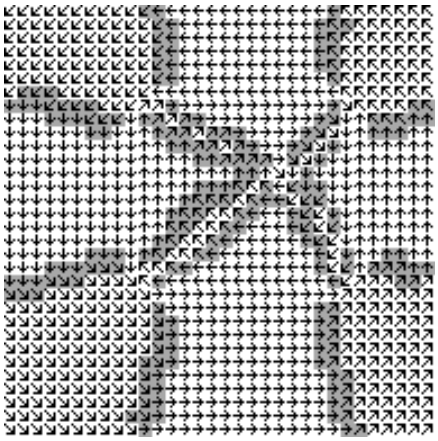

Fig. 3-40 The base points for *Test2* in the direction distribution of the vector field

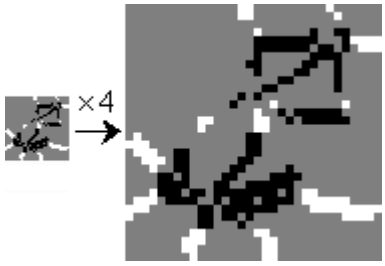

Fig. 3-41 The base points extracted for *Test3*

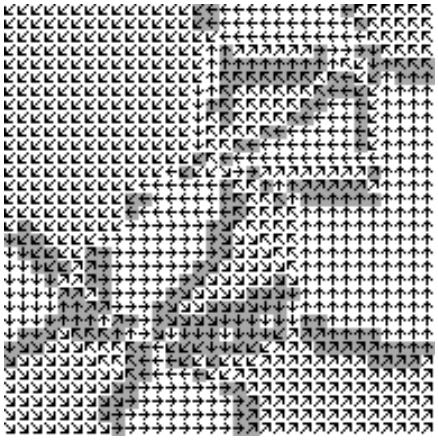

Fig. 3-42 The base points for *Test3* in the direction distribution of the vector field

3.2.3.2 Primitive region extraction in the curling vector field

In the region extraction process, each group of base points will expand to a corresponding region, which is named the "primitive region" (or "primitive area"). The primitive regions can be regarded as the elements of an image, which form a kind of representation of image structure. The primitive regions in the image can be extracted with a rotating expansion process in the curling vector field, which starts from the base points and expands according to their rotating directions. In the rotating expansion process, each group of base points will expand to a corresponding primitive region. Given the curling vector field and the base points extracted, the rotating expansion process is described as following:

***Step*1**: Gather the base points into groups. In each group, the base points are connected to each other. In another word, two neighboring base points are of the same group. Assign each group of base points

a group number. Initially, the image points with uncertain rotating direction do not belong to any group.

Step2: For each image point with a group number, carry out the rotating expansion operation. If the current point p_c belongs to a certain group, investigate the next point p_n1 on p_c's vector direction, and also investigate the next point p_n2 on p_c's rotating direction. If p_n1 or p_n2 does not belong to any group, add it to p_c's group, which is an occurrence of new classification. ***Step2*** is repeated until no new classification happens.

The results of primitive region extraction for the test images are shown in Fig. 3-43 and Fig. 3-44:

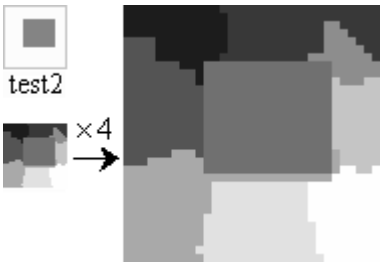

Fig. 3-43 The primitive regions extracted for *Test2*

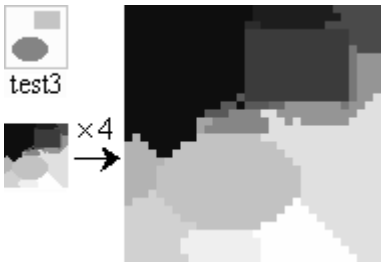

Fig. 3-44 The primitive regions extracted for *Test3*

In the experimental results of *test2* and *test3*, the object regions are extracted completely (the rectangle in *test2*, and the rectangle and circle in *test3*). Moreover, the background areas in *test2* and *test3* are split into several sub-regions. Therefore, a region may be split into several sub-regions in the rotating expansion process, especially the background region or the large object regions in real world images. In order to obtain effective segmentation result, a region-merging step is needed. The method of real world image segmentation in the curling vector field is presented in the following section.

3.2.3.3. Real world image segmentation based on the curling vector field

Experiments are also carried out for real world images to extract primitive regions. The images are of the size 128×128. The experimental results of the broadcaster image, the peppers image, the house image and the brain image are shown as follows. The experimental results indicate that the number of primitive regions is large because of the complexity of real world images. There are 274 primitive regions for the broadcaster image, 628 for the pepper image, 398 for the house image, and 423 for the brain image.

To obtain meaningful segmentation result, the region-merging step is proposed according to least gray-scale difference criterion. First, an expected number of remaining regions after merging is given. Then the following steps are carried out to merge regions until the expected region number is reached:

Step1: For each region in the image, calculate its average gray-scale value;

Step2: Find the pair of neighboring regions with the least difference of the average gray-scale, and merge them into one region;

Step3: If current region number is larger than the expected region number, return to ***Step1***; otherwise, end the merging process;

Based on the above sections, a method of image segmentation in the curling vector field transform is proposed as following:

Step1: Implement the curling vector field transform on the gray-scale image;

Step2: Judge the rotating direction of each image point, and extract the base points in the curling vector field;

Step3: Gather the neighboring base points into corresponding group, and each group is assigned a group number;

Step4: Extract the primitive regions by the rotating expansion, which starts from the base points;

Step5: Merge neighboring primitive regions according to the least average gray-scale difference criterion, and obtain the segmentation result with a pre-defined number of remaining regions.

The proposed segmentation method is applied to a group of real world images. The results of the broadcaster image, the pepper image, the house image and the brain image are shown in Fig. 3-45 to Fig. 3-52. Fig. 3-45, Fig. 3-47, Fig. 3-49 and Fig. 3-51 are the original images. Fig. 3-46 is the segmentation result of the broadcaster image with 20 regions remained after merging. Fig. 3-48 is the segmentation result of the pepper image with 40 regions remained after merging. Fig. 3-50 is the segmentation result of the house image with 50 regions remained after merging. Fig. 3-52 is the segmentation result of the brain image with 60 regions remained after merging. In Fig. 3-46, Fig. 3-48, Fig. 3-50 and Fig. 3-52, different regions are differentiated from each other by different gray-scale values.

The curling vector field has the unique feature that inside each homogeneous region the vectors have a rotating whorl pattern, which is a kind of image structure representation. This feature of the curling vector field is exploited in image segmentation. Experimental results indicate that image segmentation can be effectively implemented in the curling vector field. Further research will investigate other properties of the curling vector transform, and its application in other image processing tasks will also be studied.

Fig. 3-45 The broadcaster image (20 regions remained after merging)

Fig. 3-46 Segmentation result of the broadcaster image

Fig. 3-47 The pepper image (40 regions remained after merging)

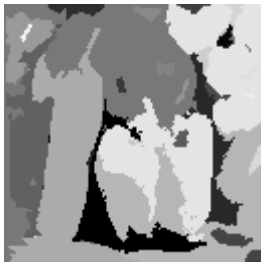

Fig. 3-48 Segmentation result of the pepper image

Fig. 3-49 The house image (50 regions remained after merging)

Fig. 3-50 Segmentation result of the house image

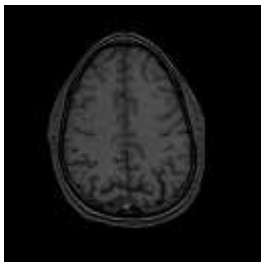

Fig. 3-51 The brain image (60 regions remained after merging)

Fig. 3-52 Segmentation result of the brain image

3.3 The curl source reversing for digital images

The magneto-static field has some unique characteristics different from the electro-static field. The field of magnetic induction has its curl as the field source, while the electro-static intensity has its divergence as the field source. It is interesting and worthwhile to take the image as the magneto-static field and study its virtual source (i.e. its curl). In this section, the curl source reversing for gray-scale images is studied. According to the following analysis and experiments, it is quite interesting that the virtual curl source has close relationship with the image gradient field.

3.3.1 The relationship between the magnetic field and its field source

In physics, moving charges generate magnetic field in the space. Thus the moving charges (i.e. the current) can be conceptually regarded as the source of the magnetic field. On the other hand, if the magnetic field is known, the field source of current density can be reversed according to the Ampere's law in differential form[75-78]:

$$\nabla \times \vec{B} = \mu_0 \cdot \vec{J} \tag{3-16}$$

where $\vec{B}$ is the magnetic induction; $\vec{J}$ is the current density (i.e. the field source distribution); μ_0 is the permeability constant; ∇ is the Hamiltonian operator:

$$\nabla = \frac{\partial}{\partial x}\vec{i} + \frac{\partial}{\partial y}\vec{j} + \frac{\partial}{\partial z}\vec{k} \tag{3-17}$$

The operator $\times$ means the cross product of two vectors. The operation of $\nabla\times$ obtains the curl of the vector field $\vec{B}$, i.e. the source distribution $\vec{J}$ has direct relationship to the curl of $\vec{B}$. Therefore, the reverse from the magnetic field to the source is as following:

$$\vec{J} = \frac{\nabla \times \vec{B}}{\mu_0} \tag{3-18}$$

Because the source reflects underlying structural feature of the field, a transform from the image to the virtual curl source is proposed for image structure representation in the next section.

3.3.2 The virtual curl source reversing

In physics, the field is determined by the source distribution. Therefore, the field source can be a compact representation of the field. It may reveal structural characteristics of the field, which can be exploited in image transform and analysis. In this section, a novel image transform is presented imitating the source reverse of the magnetic field. Because the source distribution of magnetic field is its curl, the transform is named the "curl source reverse".

The image $f(x,y)$ itself is a scalar distribution in the 2-D domain. To get the virtual curl source of the image, each image pixel is represented by a vector $\vec{I}(x,y)$, which comes outward from the 2-D plane. Moreover, the vector representing a pixel is at a right angle to the 2-D plane, and its magnitude is defined as the gray-scale value of that pixel:

$$\vec{I}(x,y) = f(x,y)\cdot\vec{k} \tag{3-19}$$

With such definition, the image $f(x,y)$ is represented by the vertical vector field $\vec{I}$. A simple example of the vector field representing a small image area of the size 3×3 is shown in Fig. 3-53.

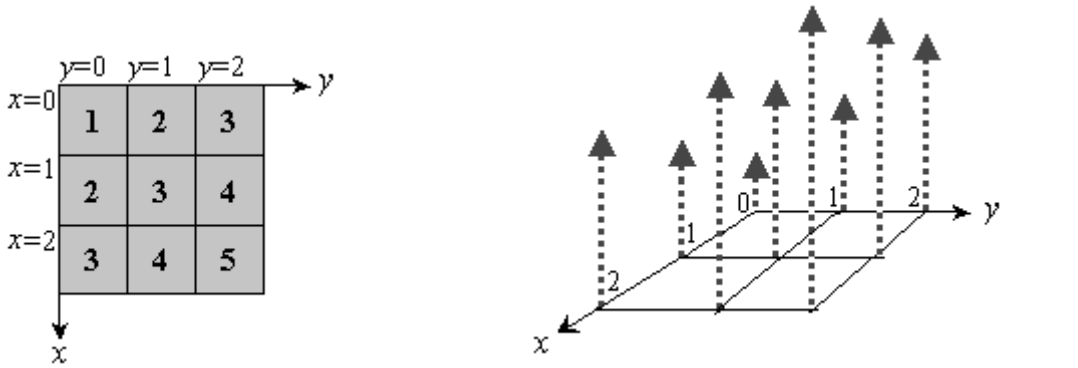

(a) The small image (b) The vertical vector field representing the small image of (a)

Fig. 3-53 A simple example of the vector field representing a small image

The curl source reverse is proposed as the reverse from the vertical field $\vec{I}$ (as virtual magnetic induction) to the virtual current density distribution (named as the virtual "curl source") imitating Equation (3-18). To achieve the curl source reverse, replace $\vec{B}$ in Equation (3-18) with $\vec{I}$:

$$\vec{C} = \nabla\times\vec{I} = \begin{vmatrix} \vec{i} & \vec{j} & \vec{k} \\ \dfrac{\partial}{\partial x} & \dfrac{\partial}{\partial y} & \dfrac{\partial}{\partial z} \\ I_x & I_y & I_z \end{vmatrix} = \left(\frac{\partial I_z}{\partial y} - \frac{\partial I_y}{\partial z}\right)\vec{i} + \left(\frac{\partial I_x}{\partial z} - \frac{\partial I_z}{\partial x}\right)\vec{j} + \left(\frac{\partial I_y}{\partial x} - \frac{\partial I_x}{\partial y}\right)\vec{k} \tag{3-20}$$

where $\vec{C}$ is the virtual curl source; $\vec{i}$, $\vec{j}$ and $\vec{k}$ are the three unit vectors on the x, y and z coordinates respectively.

It is notable that the components of $\vec{I}$ on the x-coordinate and y-coordinate are both zero because it is defined as a vertical vector field. If Equation (3-19) and (3-20) are combined, the curl source reverse is given as following:

$$\vec{C} = \begin{vmatrix} \vec{i} & \vec{j} & \vec{k} \\ \dfrac{\partial}{\partial x} & \dfrac{\partial}{\partial y} & \dfrac{\partial}{\partial z} \\ 0 & 0 & f(x,y) \end{vmatrix} = \frac{\partial f(x,y)}{\partial y}\vec{i} - \frac{\partial f(x,y)}{\partial x}\vec{j} \tag{3-21}$$

According to Equation (3-21), the result of curl source reverse is a vector field $\vec{C}(x,y)$ defined on the same 2D plane as the image itself.

Because $f(x,y)$ is a digital image, the two partial derivatives in Equation (3-21) should be estimated by discrete operators. In this section, the Sobel operator is used for the estimation. The two templates for partial derivative estimation are shown in Fig. 3-54.

-1	0	1
-2	0	2
-1	0	1

The template to estimate the derivative on x-coordinate

1	2	1
0	0	0
-1	-2	-1

The template to estimate the derivative on y-coordinate

Fig. 3-54 The two templates of Sobel operator to estimate the gradient vector

According to the Sobel operator, for the digital image $f(x,y)$, the two components of the virtual curl source are estimated as following:

$$\begin{aligned} C_x(x,y)&=[f(x\text{-}1,y\text{+}1)\text{-}f(x\text{-}1,y\text{-}1)]\text{+}2[f(x,y\text{+}1)\text{-}f(x,y\text{-}1)]\text{+}[f(x\text{+}1,y\text{+}1)\text{-}f(x\text{+}1,y\text{-}1)] \\ C_y(x,y)&=\text{-}[f(x\text{+}1,y\text{-}1)\text{-}f(x\text{-}1,y\text{-}1)]\text{-}2[f(x\text{+}1,y)\text{-}f(x\text{-}1,y)]\text{-}[f(x\text{+}1,y\text{+}1)\text{-}f(x\text{-}1,y\text{+}1)] \end{aligned} \quad (3\text{-}22)$$

Equation (3-22) defines the operation of curl source reverse for digital images. The virtual curl source for an image is defined as a discrete vector field on the image plane, whose x and y components are defined in Equation (3-22). The properties of the virtual curl source are investigated experimentally in the next section.

3.3.3 The spatial properties of the virtual curl source for digital images

Equation (3-21) indicates that for a vector in the virtual curl source, its component on the x-coordinate is the partial derivative of $f(x,y)$ with respect to y, and its component on the y-coordinate is the negative partial derivative with respect to x. On the other hand, it is well known that the gradient $\vec{G}$ of a field $f(x,y)$ also has the two partial derivatives as its components:

$$\vec{G}=\frac{\partial f(x,y)}{\partial x}\vec{i}+\frac{\partial f(x,y)}{\partial y}\vec{j} \quad (3\text{-}23)$$

It is indicated by Equation (3-21) and (3-23) that the virtual source obtained by the curl source reversing has direct relationship with the gradient field:

$$\begin{aligned} C_x(x,y) &= G_y(x,y) \\ C_y(x,y) &= -G_x(x,y) \end{aligned} \quad (3\text{-}24)$$

Therefore, on any point in the image, the vector in the virtual source has the same magnitude of the gradient vector on that point, but their directions are different. According to Equation (3-24), the vector of $\boldsymbol{C}$ is obtained by two steps: reflect the vector of $\boldsymbol{G}$ across the line with the slope of 1.0, followed by another reflection across the x-axis. In fact, it can be easily proved that the vector of $\boldsymbol{C}$ is perpendicular to the vector of $\boldsymbol{G}$ because the two vectors of $\boldsymbol{C}$ and $\boldsymbol{G}$ are orthogonal. The relationship between a vector in the curl source and its corresponding gradient vector is shown in Fig. 3-55. Because the gradient is always taken as the feature of edges in the image, the virtual source obtained by the curl source reverse will also reflect structural feature of the image.

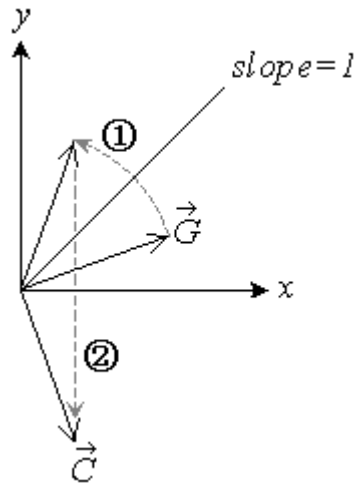

Fig. 3-55 The relationship between a vector in the curl source and its corresponding gradient vector

Experiments are carried out for a group of test images to study the basic properties of the virtual curl source. The curl source reverse is implemented by programming in C language. The test images are of the size 32×32. The experimental results are shown in Fig. 3-56 to Fig. 3-60. The figures with the label (a) in Fig. 3-56 to Fig. 3-60 are the original test images. The figures with the label (b) in Fig. 3-56 to Fig. 3-60 are the magnitude distributions of the virtual curl source. The figures with the label (c) in Fig. 3-56 to Fig. 3-60 are the direction distributions of the virtual curl source.

(a) The image *test1* (4 times of the original size on the right for a clear view)

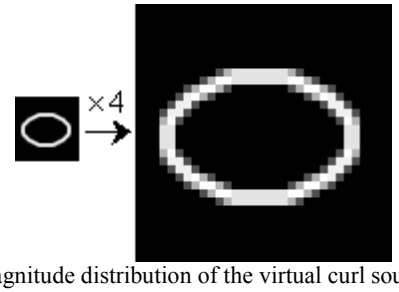

(b) The magnitude distribution of the virtual curl source of *test1*
(4 times of the original size on the right for a clear view)

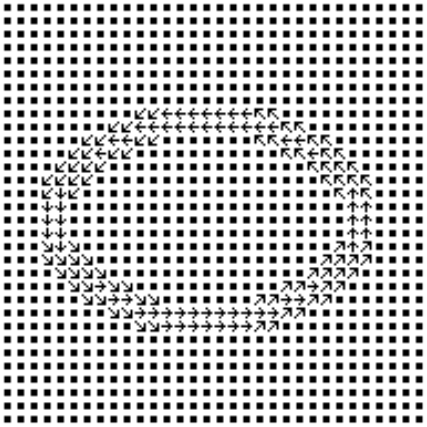

(c) The direction distribution of the virtual curl source of *test1*

Fig. 3-56 The result of curl source reverse for *test1*

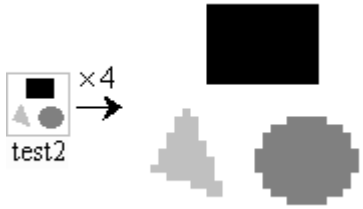

(a) The image *test2* (4 times of the original size on the right for a clear view)

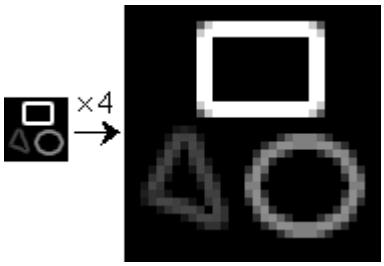

(b) The magnitude distribution of the virtual curl source of *test2*
(4 times of the original size on the right for a clear view)

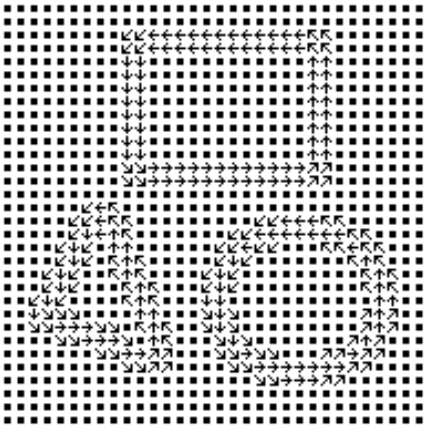

(c) The direction distribution of the virtual curl source of *test2*

Fig. 3-57 The result of curl source reverse for *test2*

(a) The image *test3* (4 times of the original size on the right for a clear view)

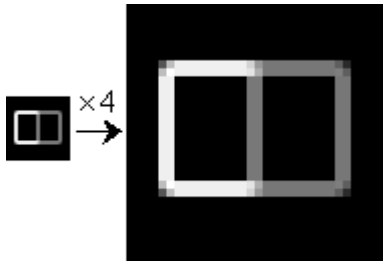

(b) The magnitude distribution of the virtual curl source of *test3*
(4 times of the original size on the right for a clear view)

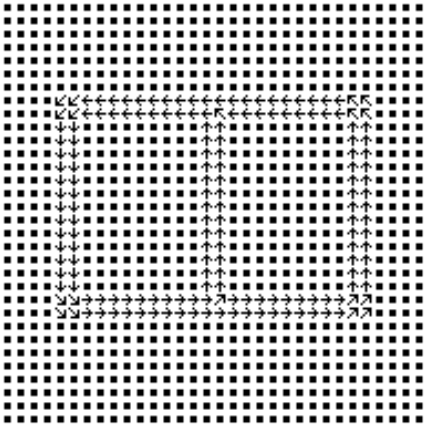

(c) The direction distribution of the virtual curl source of *test3*

Fig. 3-58 The result of curl source reverse for *test3*

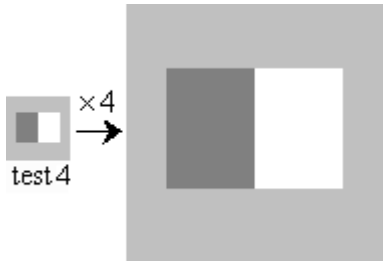

(a) The image *test4* (4 times of the original size on the right for a clear view)

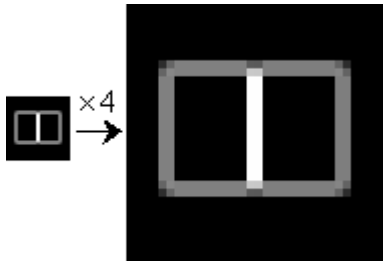

(b) The magnitude distribution of the virtual curl source of *test4*
(4 times of the original size on the right for a clear view)

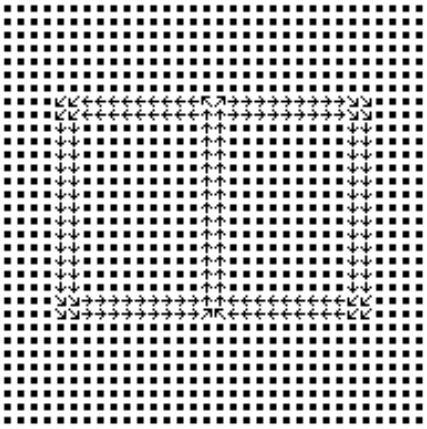

(c) The direction distribution of the virtual curl source of *test4*

Fig. 3-59 The result of curl source reverse for *test4*

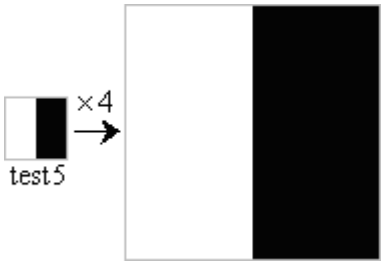

(a) The image *test5* (4 times of the original size on the right for a clear view)

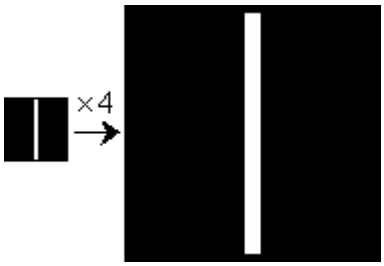

(b) The magnitude distribution of the virtual curl source of *test5*
(4 times of the original size on the right for a clear view)

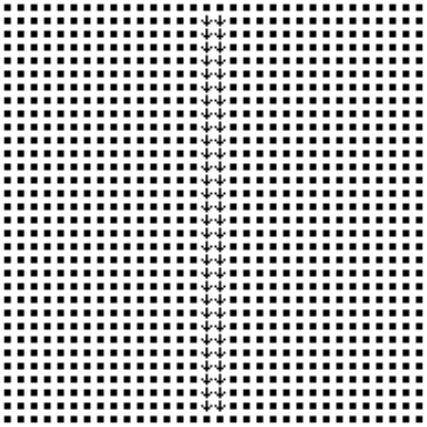

(c) The direction distribution of the virtual curl source of *test5*

Fig. 3-60 The result of curl source reverse for *test5*

The experimental results reveal the spatial properties of the virtual curl source. In the figures with the label (b) in Fig. 3-56 to Fig. 3-60, larger gray-scale values correspond to larger vector magnitudes.

The figures with the label (b) in Fig. 3-56 to Fig. 3-60 show that the energy (i.e. non-zero values) in the virtual curl source concentrates near the region borders, where there is more complex structure than the other parts of the image[88,89]. This is because each vector in the virtual curl source has the same magnitude as the gradient vector at the same point, but their directions are different. This property of energy concentration in the magnitude distribution of the virtual curl source may be exploited in data compression, which is similar to the energy concentration of the 2-D Fourier transform in the frequency domain [90-92].

The direction distribution of the virtual curl source is shown in the figures with the label (c) in Fig. 3-56 to Fig. 3-60. The direction angles of the vectors are visualized by discretizing the angles into 8 discrete directions. The black dots in the figures with the label (c) in Fig. 3-56 to Fig. 3-60 indicate the positions of zero vectors. Experimental results indicate that the direction distribution of the virtual source has direct relationship with the image structure. In the figures with the label (c) in Fig. 3-56 to Fig. 3-60, the vectors in the virtual curl source have a rotating pattern as a whole, which rotate along the borders of the regions. For example, the curl vectors in Fig. 3-56(c) rotate anti-clockwise as a whole. On the other hand, the curl vectors in the source are zero within homogeneous regions.
Moreover, the rotating direction of the curl vectors as a whole has direct relationship with the gray-scale difference between adjacent regions. Experimental results indicate that when moving along the rotating direction indicated by the curl vectors, the region on the left hand has lower gray-scale than that on the right hand. Therefore, the spatial properties of the magnitude and direction distributions of the virtual curl source can be an effective representation of image structure, which may be exploited in further analysis.

3.3.4 The opposite transform form the virtual curl source to the restored image

It is an important characteristic of a transform whether it is reversible. For the curl source reverse, the opposite transform from the virtual curl source to the restored image is discussed in this section.

In physics, the continuous magnetic field $\vec{B}$ can be obtained from the distribution of the current density $\vec{J}$, which is well known as the Biot-Savart Law[75-78]:

$$\vec{B}(p) = \frac{\mu_0}{4\pi} \int_V \frac{\vec{J} \times \vec{r}}{r^3} dv \tag{3-25}$$

where $\vec{B}(p)$ is the magnetic induction at the point p; $\vec{J}$ is the current density; $\vec{r}$ is the vector from the current density to the point p. The integral in Equation (3-25) is for the whole source space where the current density exists.

Imitating Equation (3-25), the restoration from the virtual source $\vec{C}(x, y)$ to the field $\vec{I}'(x, y)$ (i.e. the restored image) is proposed. Because the virtual source and the gradient field are related by Equation (3-24), the proposed restoration method can also be a method for estimating the image from its gradient field.

Because $\vec{C}(x, y)$ is a vector field defined on a discrete 2-D plane, the restoration of the field $\vec{I}'(x, y)$ should also use discrete operations, i.e. the integral in Equation (3-25) should be replaced by summation as following:

$$\vec{I}'(x, y) = K \cdot \sum_{\substack{j=0 \\ (j \neq y \text{ or } i \neq x)}}^{H-1} \sum_{i=0}^{W-1} \frac{\vec{C}(i, j) \times \vec{r}_{(i,j) \to (x,y)}}{r^3_{(i,j) \to (x,y)}} \tag{3-26}$$

where K is a constant; H and W are the height and width of the image respectively; $\vec{C}(i,j)$ is the virtual curl source; $\vec{I}'(x,y)$ is the restored field whose magnitude distribution corresponds to the restored image; $\vec{r}_{(i,j)\to(x,y)}$ is the vector from (i,j) to (x,y).

Because $\vec{r}_{(i,j)\to(x,y)}$ and $\vec{C}(x,y)$ are both 2D vector fields on the image plane, their components on z-coordinate are zero:

$$\begin{aligned} C_z &= 0 \\ r_z &= 0 \end{aligned} \tag{3-27}$$

Therefore, the cross product of $\vec{C}(x,y)$ and $\vec{r}_{(i,j)\to(x,y)}$ is as following:

$$\vec{C}\times\vec{r} = \begin{vmatrix} \vec{i} & \vec{j} & \vec{k} \\ C_x & C_y & C_z \\ r_x & r_y & r_z \end{vmatrix} = \begin{vmatrix} \vec{i} & \vec{j} & \vec{k} \\ C_x & C_y & 0 \\ r_x & r_y & 0 \end{vmatrix} = (C_x r_y - C_y r_x)\vec{k} \tag{3-28}$$

where r_x and r_y are the two components of $\vec{r}_{(i,j)\to(x,y)}$ respectively. Combine Equation (3-26) and (3-28), the restoration of the field from the virtual curl source is given as following:

$$\vec{I}'(x,y) = K \cdot \sum_{\substack{j=0 \\ (j\neq y \text{ or } i\neq x)}}^{H-1}\sum_{i=0}^{W-1} \frac{(C_x(i,j)\cdot r_y - C_y(i,j)\cdot r_x)}{r^3_{(i,j)\to(x,y)}}\vec{k} \tag{3-29}$$

Because the virtual curl source is related to the gradient field of the image by Equation (3-24), the above restoration is also a way to estimate the original image from its gradient field with the virtual curl source as an intermediary. First, the gradient field can be transformed to $\vec{C}(x,y)$ according to Equation (3-24). Then the image can be estimated according to Equation (3-29).

Experiments of image restoration from the virtual curl source are carried out for a group of real world images. The experimental results are shown in Fig. 3-61 to Fig. 3-66. The figures with the label (a) in Fig. 3-61 to Fig. 3-66 are the visualization of the original magnitude distribution of the restored $\vec{I}'(x,y)$. The figures with the label (b) in Fig. 3-61 to Fig. 3-66 are the results after contrast enhancement of the original restored magnitudes. The figures with the label (c) in Fig. 3-61 to Fig. 3-66 are the original images.

(a) Visualization of $I'(x,y)$ (b) Result of contrast enhancement (c) The original image of the boat

Fig. 3-61 The result of opposite transform from the virtual curl source to the boat image

(a) Visualization of $I'(x,y)$ (b) Result of contrast enhancement (c) The original image of the bridge

Fig. 3-62 The result of opposite transform from the virtual curl source to the bridge image

(a) Visualization of $I'(x,y)$ (b) Result of contrast enhancement (c) The original image of the house

Fig. 3-63 The result of opposite transform from the virtual curl source to the house image

(a) Visualization of $I'(x,y)$ (b) Result of contrast enhancement (c) The original image of the peppers

Fig. 3-64 The result of opposite transform from the virtual curl source to the peppers image

(a) Visualization of $I'(x,y)$ (b) Result of contrast enhancement (c) The original image of the cameraman

Fig. 3-65 The result of opposite transform from the virtual curl source to the cameraman image

(a) Visualization of $I'(x,y)$ (b) Result of contrast enhancement (c) The original image of the broadcaster

Fig. 3-66 The result of opposite transform from the virtual curl source to the broadcaster image

The results indicate that the restored images can be the approximations of the original images for visual understanding, but there are differences between the restored and original images. Although the transform for continuous field defined by Equation (3-18) and (3-25) are reversible, the curl source reverse for digital images defined by Equation (3-22) and (3-29) includes operations of discretization, which introduces data errors into the restored results. Therefore, the proposed transform of curl source reverse is not strictly reversible, but the opposite transform from the virtual curl source to the image just provides relatively acceptable results for visual perception.

Further research will investigate the application of the curl source reverse in other image processing applications. It will also be investigated to remove the data errors caused by discretization in the transform process so that the opposite transform from the virtual curl source to the image can have the quality similar to those strictly reversible transforms.

4 Relative Field Method on Image Sequence Processing

Image sequence processing is one of the main research topics in digital image processing, which has significant value in theory and practice[93-96]. An image sequence can be regarded as a 3D signal $g(x,y,t)$. The 3D signal of image sequence can have much more information than a single 2D image $f(x,y)$. Many real-world applications are based on image sequence processing such as security monitoring, traffic surveillance, medical image sequence analysis, etc. For such practical tasks, the trend is advanced intelligent analysis which aims at accurate object recognition, human gesture recognition and even behavior recognition. The practical tasks continuously give new requirements of processing techniques, which has attracted lots of research interest and efforts.

Recently, physics inspired methodology has attracted more and more research interest in image processing, which exhibits the ability of effective feature extraction and analysis[3,17,19,22,69-74]. Electro-static field plays an important role in such methods[3,19,70,74]. The fundamental idea underlying the methods inspired by physical fields is the transform from one form of the field to another (i.e. from field source to its potential) so that the feature of interest can be revealed[3,74]. Some unique characteristics of the physical fields are exploited in such methods, which leads to impressively effective processing results. Preliminary results indicate the promising wide application of such methods in practical tasks.

Currently, most physics-inspired methods concentrate on the processing of single 2D images. In previous Chapters of the book, the authors have studied a series of novel methods inspired by electro-magnetics for single 2D image analysis. In this chapter, the physical field inspired methodology is extended to image sequence analysis based on the authors' previous work. In fact, the relative potential and most vector field methods in Chapter 2 and 3 have some similarity in the definition of the virtual field, including the relative potential field, diffusing vector field, curling vector field and compressing vector field. All of them define the virtual field by introducing the measurement of pixel difference $g(i,j)$-$g(x,y)$ into their definitions. Such virtual fields are named "relative field", which are defined with the relative value of one pixel compared to another (i.e. $g(i,j)$-$g(x,y)$). In this chapter, the 3D relative potential field is studied as a typical example of extending the "relative field" for 2D images to 3D image sequence analysis. Because the similarity in definition, other "relative field" methods in this book may be extended to their 3D forms in a similar way.

The method described in this chapter is named three-dimensional relative potential, which exploits the relationship between the source and the potential in the physical electro-static field. The spatial property of the 3D relative potential is investigated by both theoretic analysis and experiments, which proves that the positive-negative sign distribution of the 3D relative potential value is a natural and convenient representation for 3D volume separation and segmentation. The segmented 3D volumes in the 3D relative potential field provide an effective object tracking method in image sequences, which can be used in further intelligent recognition.

4.1 The 3D relative potential field of image sequences

In the physical electro-static field, the potential is determined by the source (i.e. the charge distribution)[75-78]. Therefore, the potential field can reflect some characteristics of the source. This relationship between the field and its source can be exploited in image transform, in which the image is regarded as the source (i.e. the pixels are regarded as discrete charges) and the generated virtual field may reveal important features of the images. The attraction of physical field inspired methods is the possibility of a natural representation of image structure or components without artificially set parameters (such as thresholds in image segmentation). In this chapter, a general form of virtual potential field for 3D image sequence is proposed, which is inspired by the physical electro-static field.

4.1.1 The electro-static potential and its spatial property

The formula of the physical electro-static potential generated by a charge q is[75-78]:

$$V = \frac{1}{4\pi\varepsilon} \cdot \frac{q}{r} \tag{4-1}$$

where V is the electro-static potential at a space point. q is the charge quantity. r is the distance between the charge and the space point. ε is a physical constant.

For a charge distribution ρ in the space, the potential generated by ρ on point (x,y) is[75-78]:

$$V = \frac{1}{4\pi\varepsilon} \int_V \frac{\rho \cdot d\tau}{r} \tag{4-2}$$

where V is the electro-static potential at a space point. The integral in Equation (4-2) is for the 3D area where the charge distribution ρ exists.

Many image processing techniques involves local operations in the image, i.e. local image features are extracted and analyzed[79-81]. Local image features usually have the form of a function $f(x,y,z)$ defined in the three-dimensional space of the image sequence. On the other hand, the analysis of the image also requires consideration of the neighbouring area of each image point in order to get practically useful results. Generally speaking, neighbouring points have stronger relevance than remote points, i.e. the closer the distance, the stronger the relevance. In many image processing tasks, it is necessary to consider the balance between the strong local relevance of close neighbouring points and a wide range of weaker relevance of remote points. Equation (4-2) indicates that the potential of a charge q on a space point (i.e. the impact of q on that point) is in direct proportion to the reciprocal of the distance r. The mathematical form of the distance reciprocal in Equation (4-2) inspires the representation of the local-global relevance between image points. For a point p in the space, the near charge distribution in the small local neighboring area has greater impact on p's potential than remote charge distribution. On the other hand, no matter how far the distance is, remote charge distribution still has relatively weak impact on p's potential. Moreover, the accumulation of the weak impacts of wide-range remote charge distribution can not be neglected. The above characteristic of the distance reciprocal form in Equation (4-2) is quite suitable for the requirement of image analysis that both local and global relevance between image points should be considered[82-87].

4.1.2 A general form of virtual potential field for images

The electro-static potential has a suitable mathematical form to model the local-global relevance of image points. Here a general form of virtual image potential field is proposed with the electro-static analogy. For image analysis, not only the distance between two image points but also the relationship between their gray-scale should be considered. Therefore, a general continuous form of virtual potential field for image sequences is proposed as:

$$V_c^m(x,y,z) = A \cdot \int_a \int_b \int_c \frac{f(g(a,b,c), g(x,y,z))}{r^m_{(a,b,c)\to(x,y,z)}} da \cdot db \cdot dc \tag{4-3}$$

where $V_c^m(x,y,z)$ is the continuous image potential value at point (x,y,z). (x,y,z) and (a,b,c) are coordinates in the 3D space. Here the 3D space corresponds to the image sequence, which includes the single image as a special 2D case. A is a predefined constant value. g is the gray-scale value of image points in the sequence (here gray-scale image sequences are considered). f is a function defined

according to specific image processing tasks, which represents the relationship between the gray-scale values of point (x,y,z) and (a,b,c). r is the distance between (x,y,z) and (a,b,c). m is a constant that affect the reciprocal's decreasing rate with the increasing distance r. The multiple integral in Equation (4-3) is on the three-dimensional image space. For a specific processing task, the function f, the constants A and m should be pre-defined according to the specific processing purpose.

For digital image sequences, the discrete form of the virtual potential field is presented as the discrete form of Equation (4-3):

$$V_d^m(x,y,z) = A \cdot \sum_{\substack{k=0 \\ (k\neq z \text{ or } j\neq y \text{ or } i\neq x)}}^{D-1} \sum_{j=0}^{H-1} \sum_{i=0}^{W-1} \frac{f(g(i,j,k), g(x,y,z))}{r_{(i,j,k)\to(x,y,z)}^m} \tag{4-4}$$

where $V_d^m(x,y,z)$ is the discrete image potential on point (x,y,z). A is a predefined constant value. H and W are the height and width of the digital image respectively. D is the depth of the image sequence (i. e. the frame number), which may represent the temporal position in a video sequence, or the spatial position in a sequence of section scanning. g is the gray-scale value of image points. f is a function defined according to specific image processing tasks, which represents the relationship between the gray-scale values of point (x,y,z) and (i,j,k). r is the distance between (x,y,z) and (i,j,k). m is a constant that affect the reciprocal's decreasing rate with the increasing distance r. Equation (4-4) imitates the form of the physical electro-static potential. It is defined in a flexible form, which extends the physical formula of (4-2) by introducing the function f and constant m adjustable for different processing tasks.

4.1.3 The definition of 3D relative potential field

For some important image processing tasks such as edge detection and segmentation, the difference between pixels (i.e. their gray-scale difference) is the factor of major consideration. In this chapter, the 3D relative potential is proposed for gray-scale image sequences based on the general form of discrete image potential, where the function $f(g(i,j,k), g(x,y,z))$ in Equation (4-4) is specialized as the difference between the gray-scale values of the two points (x,y,z) and (i,j,k) in the sequence:

$$V_R^m(x,y,z) = A \cdot \sum_{\substack{k=0 \\ (k\neq z \text{ or } j\neq y \text{ or } i\neq x)}}^{D-1} \sum_{j=0}^{H-1} \sum_{i=0}^{W-1} \frac{g(i,j,k) - g(x,y,z)}{r_{(i,j,k)\to(x,y,z)}^m} \tag{4-5}$$

where $V_R^m(x,y,z)$ is the discrete relative potential at the point (x,y,z). A is a predefined constant value. D, H and W are the depth, height and width of the image sequence respectively. g is the gray-scale value of the points in the sequence. r is the distance between (x,y,z) and (i,j,k). m is a constant that affect the reciprocal's decreasing rate with the increasing distance r. Equation (4-5) is an extension of the definition in section 2.1.1.

Compared with the mathematic form of the electro-static potential, the proposed relative potential has two major differences. One is the replacement of the charge with the gray-scale difference, which can make the relative potential represents the difference of one point between others in the sequence. This is the reason why the virtual potential is called "relative". The other is the m-th power of the distance r. Thus the adjustment of the value m can change the decreasing rate of the relevance between image points with the increasing distance r according to the requirement of a specific task.

4.2 The spatial characteristics of the 3D relative potential field

In Equation (4-5), the relevance between two image points with distance r is represented quantitatively by the reciprocal of r^m. The value of relative potential is virtually the weighted sum of

the gray-scale difference between the image point (x,y,z) and all other points, and the weight is the factor of relevance, i.e. the reciprocal of r^m.

According to the definition of the image relative potential in Equation (4-5), the relative potential value of a point p is mainly affected by its local neighboring area in the 3D space. The local neighboring area consists of two classes of points. One class is those in the same region of p (i.e. with similar gray-scale of p), the other is those in the different region. To investigate the properties of the relative potential field, experiments are carried out for a series of simple test image sequences. For these simple test image sequences, the gray-scale difference in the same region is zero. Thus the relative potential of p is mainly affected by the gray-scale difference between p's region and its adjacent area. Suppose $\boldsymbol{A}$ and $\boldsymbol{B}$ are two adjacent areas shown in Fig. 4-1. p_a and p_b are two border points at different border sides. p_a is in area $\boldsymbol{A}$ and p_b is in area $\boldsymbol{B}$. g_a and g_b are the gray-scale of area $\boldsymbol{A}$ and $\boldsymbol{B}$ respectively. According to the above discussion, the sign of p_a 's relative potential is determined by g_b - g_a, while the sign of p_b 's relative potential is determined by g_a - g_b. Thus the signs of p_a and p_b are opposite. Therefore, in the 3D relative potential field, the sign of the relative potential value will reverse across the border between adjacent 3D areas. In another word, the sign of the relative potential values in two different adjacent 3D bodies (or 3D volumes) is different. This spatial feature of the relative potential field can be exploited in image sequence analysis.

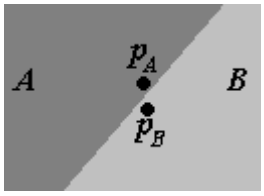

Fig. 4-1 p_a and p_b on different sides of the area border

In order to study the spatial property of the 3D relative potential field, experiments are carried out on a group of test image sequences. The simple test sequences used in this chapter are of the size 160×160 for each frame. Each sequence has 6 frames. The 3D relative potential field is calculated for each sequence. When computing the relative potential values, the constant m in Equation (4-5) is pre-defined as m=3. Fig. 4-2 To Fig. 4-9 show the experimental results for some typical test sequences. The sequences in Fig. 4-2, 4-4 and 4-6 represent the typical movements of shifting, shrinking, dilating and deforming respectively. The forth sequence in Fig. 4-8 combines the shifting, rotating and deforming simultaneously. In the experiment, the sign distribution of the 3D relative potential field is recorded for each frame.

In Fig. 4-2, there are three simple shapes (square, triangle and circle) and they move by shifting between the frames. Such test aims to investigate the relative potential distribution for sequences with objects of translational motion.

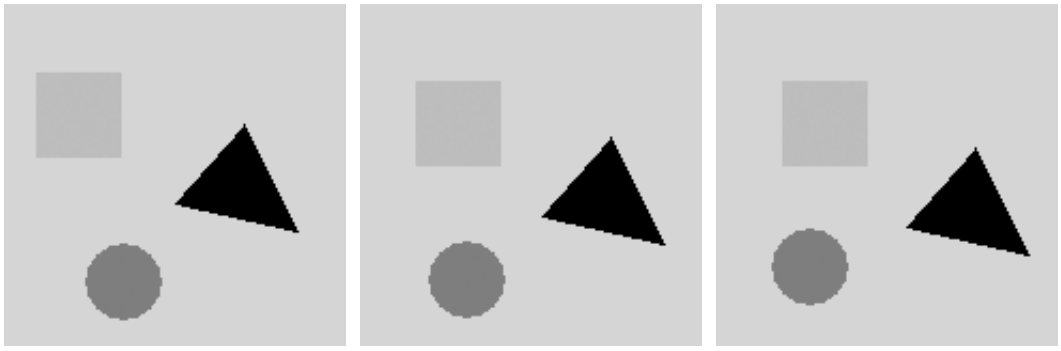

(a) frame 1 (b) frame 2 (c) frame 3

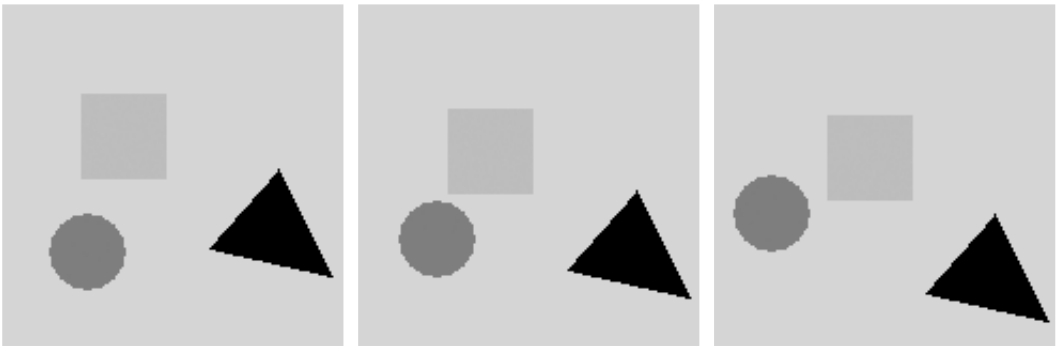

(d) frame 4 (e) frame 5 (f) frame 6

Fig. 4-2 The frames of the "shifting" sequence

In Fig. 4-3, the sign distribution of the relative potential values are shown for the "shifting" sequence, where white points represent the positive sign and the black points represents the negative sign. It is indicated that the sign of the relative potential value will reverse across the border of two adjacent 3D bodies.

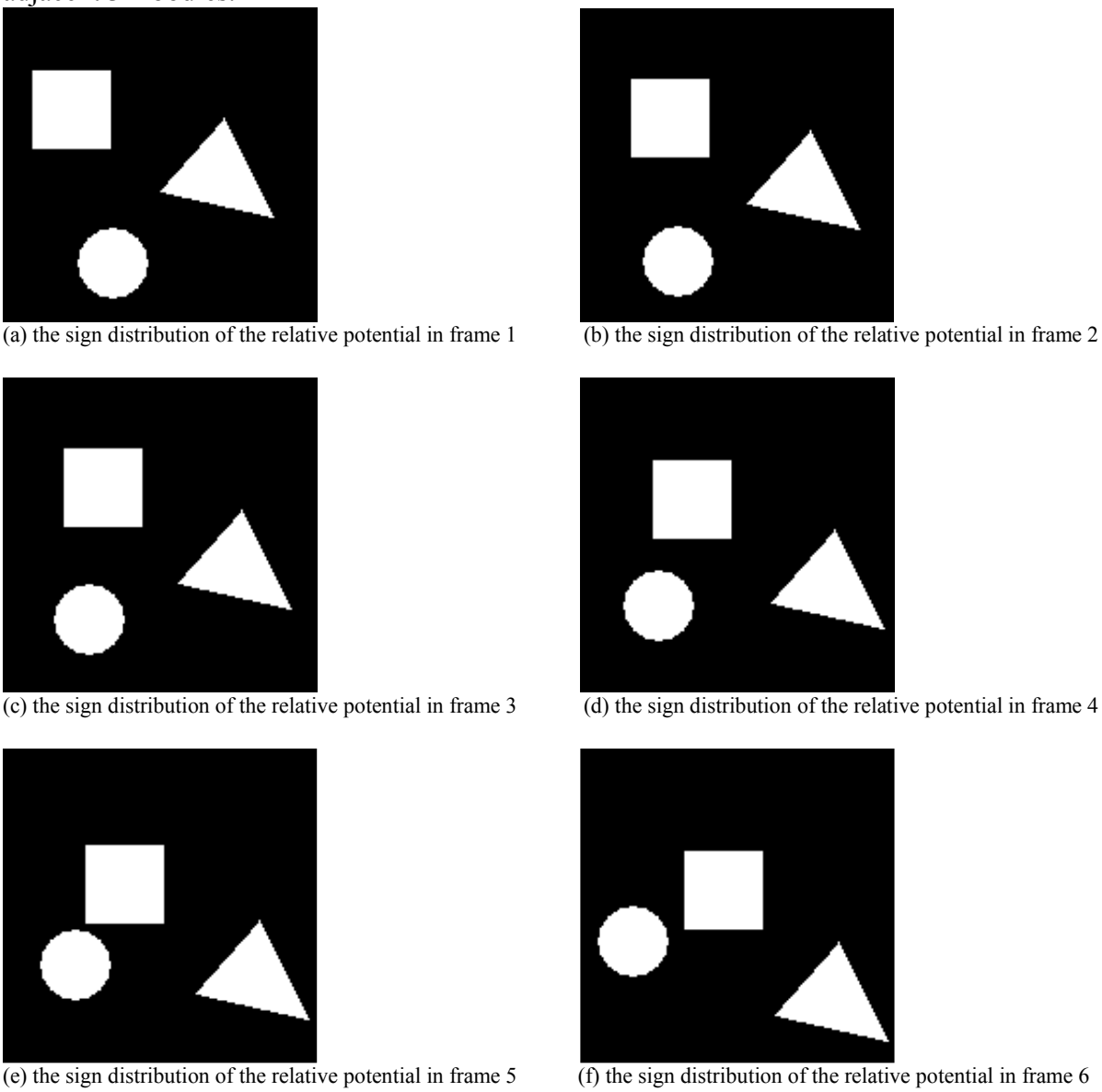

(a) the sign distribution of the relative potential in frame 1 (b) the sign distribution of the relative potential in frame 2

(c) the sign distribution of the relative potential in frame 3 (d) the sign distribution of the relative potential in frame 4

(e) the sign distribution of the relative potential in frame 5 (f) the sign distribution of the relative potential in frame 6

Fig. 4-3 The sign distribution of the 3D relative potential value on each frame of the "shifting" sequence

In Fig. 4-4, there are two simple shapes (square and circle). In the sequence the square gets smaller and smaller, while the circle gets larger and larger. Such test aims to investigate the relative potential distribution for sequences with objects of shrinking or dilating.

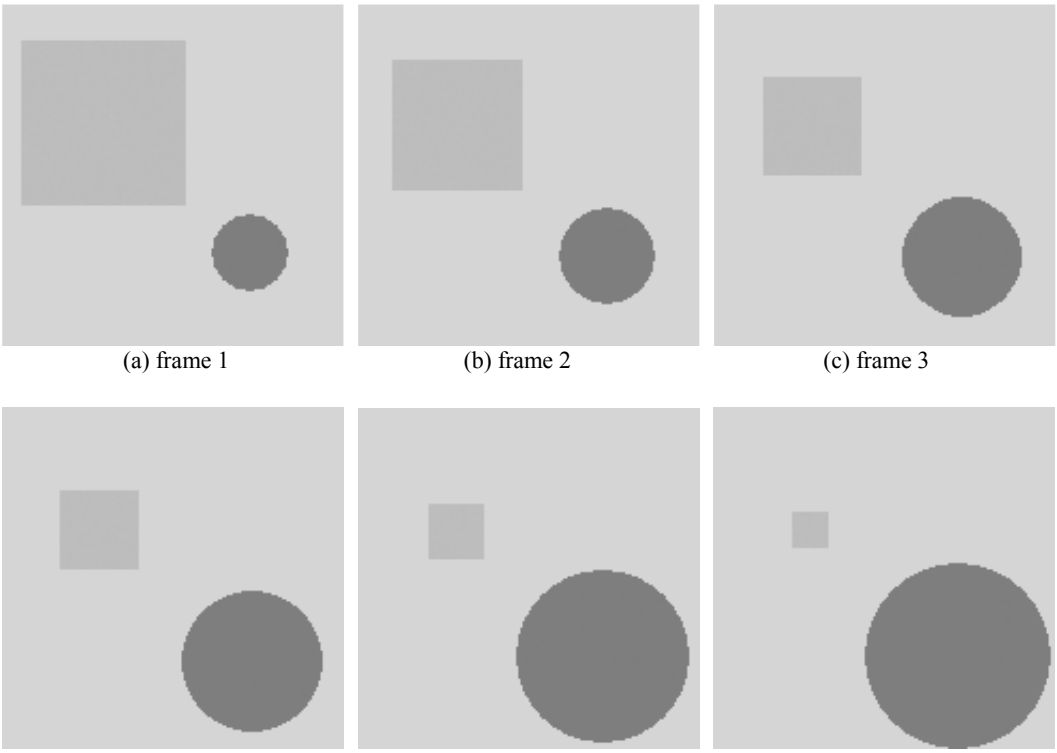

(a) frame 1 (b) frame 2 (c) frame 3

(d) frame 4 (e) frame 5 (f) frame 6

Fig. 4-4 The frames of the "shrinking and dilating" sequence

In Fig. 4-5, the sign distribution of the relative potential values are shown for the "shrinking and dilating" sequence, where white points represent the positive sign and the black points represents the negative sign. It is indicated that the sign of the relative potential value will reverse across the border of two adjacent 3D bodies.

(a) the sign distribution of the relative potential in frame 1 (b) the sign distribution of the relative potential in frame 2

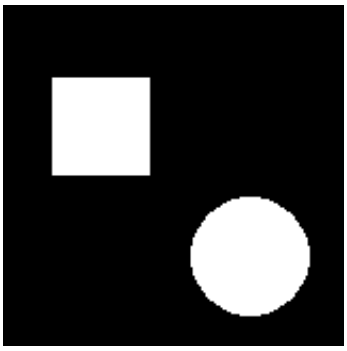

(c) the sign distribution of the relative potential in frame 3

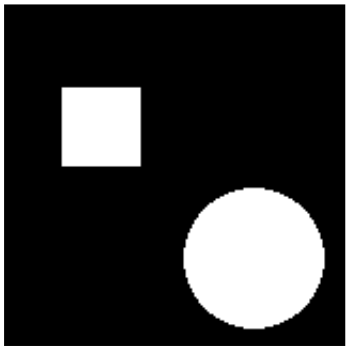

(d) the sign distribution of the relative potential in frame 4

(e) the sign distribution of the relative potential in frame 5

(f) the sign distribution of the relative potential in frame 6

Fig. 4-5 The sign distribution of the 3D relative potential value on each frame of the "shrinking and dilating" sequence

In Fig. 4-6, there are two simple shapes (square and circle). In the sequence, the square and the circle both change their shapes. The square is deformed to a rectangle and the circle to an ellipse. Such test aims to investigate the relative potential distribution for sequences with objects of deforming.

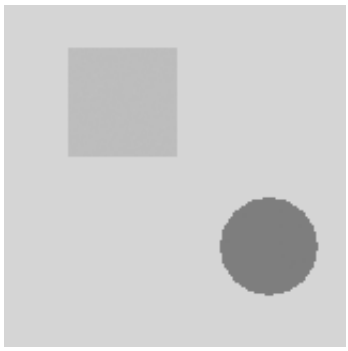

(a) frame 1

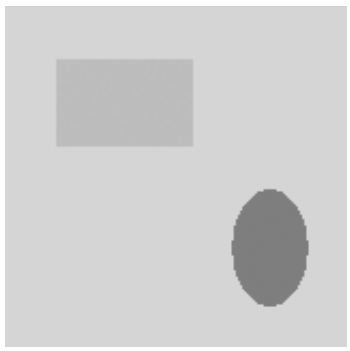

(b) frame 2

(c) frame 3

(d) frame 4

(e) frame 5

(f) frame 6

Fig. 4-6 The frames of the "deforming" sequence

In Fig. 4-7, the sign distribution of the relative potential values are shown for the “deforming” sequence, where white points represent the positive sign and the black points represents the negative sign. It is indicated that the sign of the relative potential value will reverse across the border of two adjacent 3D bodies.

(a) the sign distribution of the relative potential in frame 1

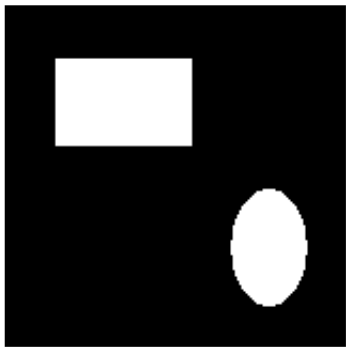

(b) the sign distribution of the relative potential in frame 2

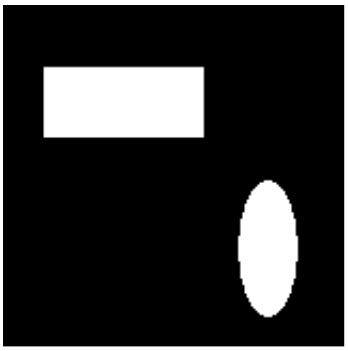

(c) the sign distribution of the relative potential in frame 3

(d) the sign distribution of the relative potential in frame 4

(e) the sign distribution of the relative potential in frame 5

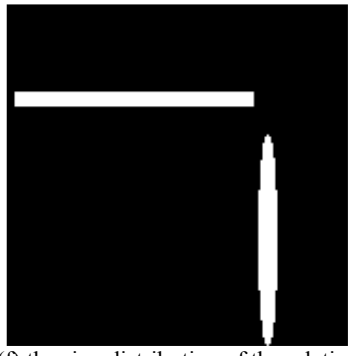

(f) the sign distribution of the relative potential in frame 6

Fig. 4-7 The sign distribution of the 3D relative potential value on each frame of the “deforming” sequence

In Fig. 4-8, there are three simple shapes (square, triangle and circle). They move by shifting, rotating and deforming. Such test is more complex in the motion of objects, which aims to investigate the relative potential distribution for sequences with objects of combinational motion.

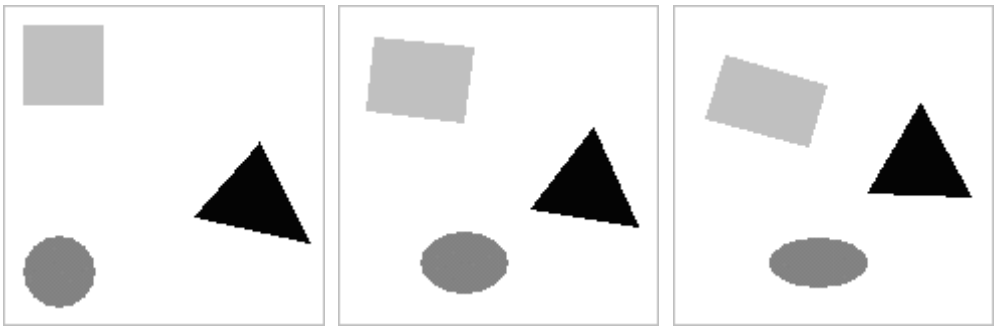

(a) frame 1 (b) frame 2 (c) frame 3

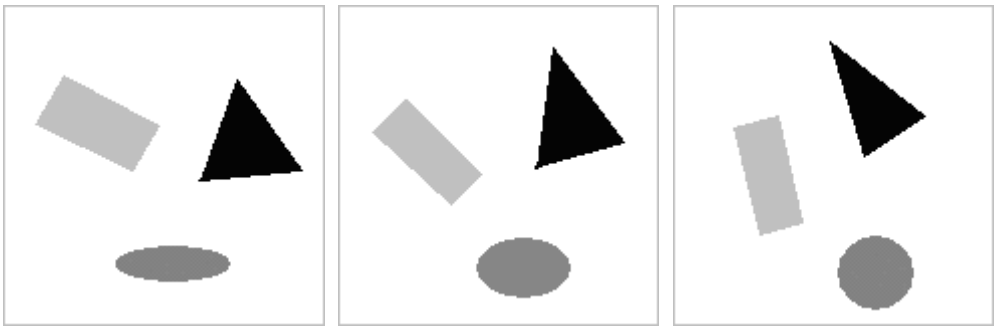

(d) frame 4 (e) frame 5 (f) frame 6

Fig. 4-8 The frames of the "combinational motion" sequence

In Fig. 4-9, the sign distribution of the relative potential values are shown for the sequence of "combinational motion", where white points represent the positive sign and the black points represents the negative sign. It is indicated that the sign of the relative potential value will reverse across the border of two adjacent 3D bodies.

(a) the sign distribution of the relative potential in frame 1

(b) the sign distribution of the relative potential in frame 2

(c) the sign distribution of the relative potential in frame 3

(d) the sign distribution of the relative potential in frame 4

(e) the sign distribution of the relative potential in frame 5

(f) the sign distribution of the relative potential in frame 6

Fig. 4-9 The sign distribution of the 3D relative potential value on each frame of the "combinational motion" sequence

The above experimental results for simple test sequences indicate the importance and possible application of the sign distribution in the 3D relative potential field. Since the sign of the relative potential reverses across the border of adjacent object areas, it may serve as the feature of 3D border. This spatial feature can be exploited in the segmentation of 3D volumes for image sequences, which is proved by the following experiments in the next section.

4.3 3D segmentation of image sequence in the relative potential field

Based on the above analysis, 3D segmentation is implemented for the simple test sequences, which separates each connected 3D volumes with the same sign of relative potential from others. Since the sign of relative potential are opposite in the two different adjacent spatial areas, this can provide the basis of object segmentation and tracking in the image sequence. Based on the experimental results, a method of 3D body division in the relative potential field is proposed as following:
***Step*1**: Calculate the 3D relative potential field;
***Step*2**: Obtain the sign distribution of the relative potential field;
***Step*3**: Group the adjacent points with the same sign of relative potential into connected 3D bodies. In the grouping process, the adjacent points of 6-connection in the 3D space for a point p at (x,y,z) is investigated. The points of 6-connection for (x,y,z) include: $(x+1,y,z)$, $(x-1,y,z)$, $(x,y+1,z)$, $(x,y-1,z)$, $(x,y,z+1)$ and $(x,y,z-1)$. If any of the six adjacent points has the same sign of relative potential as p, it is grouped into the 3D region which p belongs to. The obtained connected 3D regions are the result of segmentation for the image sequence.

The obtained set of connected regions is the result of 3D volume division for the gray-scale image sequence. Therefore, the 3D signal space of the sequence is segmented to several 3D bodies. Each 3D body is a connected 3D area in which the points have the same sign of relative potential value.

4.3.1 The 3D segmentation results for the testing image sequences

The segmentation results for some test image sequences are shown as following. Fig. 4-10 shows the 3D segmentation result of the "shifting" sequence according to the sign distribution in Fig. 4-3, where different 3D bodies are represented by different gray-scale values for visualization. The segmented 3D bodies are shown as a series of sections in 2D form. In another word, each 2D section of the bodies on the corresponding frame plane is shown separately, and in each section the areas of different 3D bodies are of different gray-scale values.

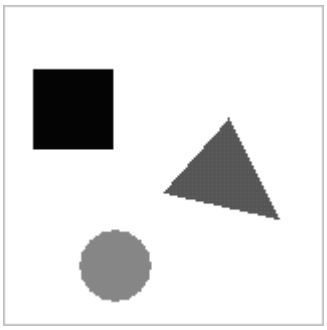

(a) the segmentation result on the plane of frame 1

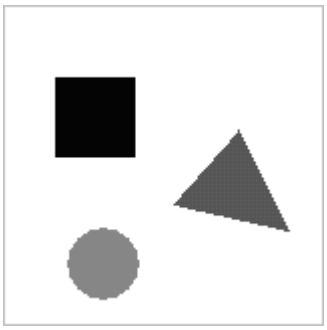

(b) the segmentation result on the plane of frame 2

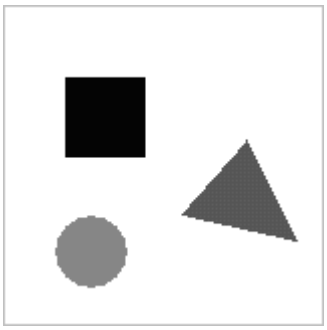

(c) the segmentation result on the plane of frame 3

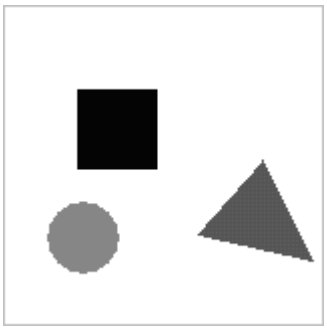

(d) the segmentation result on the plane of frame 4

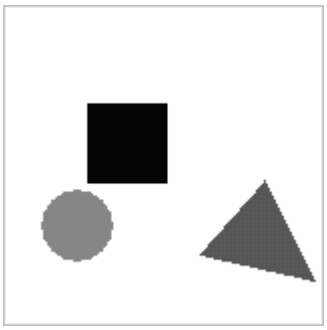

(e) the segmentation result on the plane of frame 5

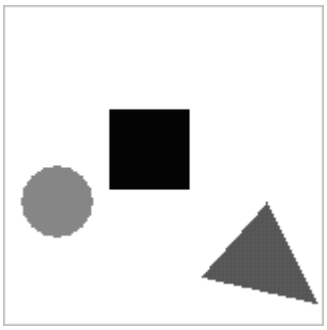

(f) the segmentation result on the plane of frame 6

Fig. 4-10 The sections of the segmented 3D bodies on each frame of the "shifting" sequence

In order to show the segmentation results in a clearer way, the sections shown in Fig. 4-10 are overlaid together in Fig. 4-11, which can clearly show the movement of each object through the sequence. In Fig. 4-11, only the region borders in each section are shown, and the arrows show the moving direction of each object.

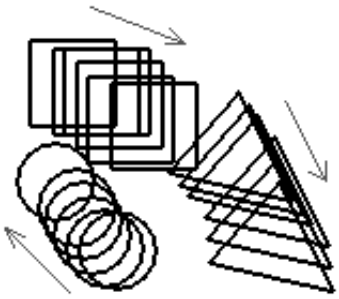

Fig. 4-11 The overlaid result of the 2D sections in Fig. 4-10

Fig. 4-12 shows the 3D segmentation result for the "shrinking and dilating" sequence according to the sign distribution in Fig. 4-5, where different 3D bodies are represented by different gray-scale values for visualization. The segmented 3D bodies are shown as a series of sections in 2D form. In another word, each 2D section of the bodies on the corresponding frame plane is shown separately, and in each section the areas of different 3D bodies are of different gray-scale values.

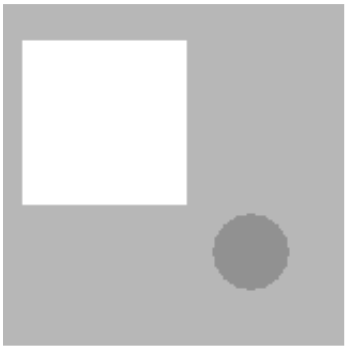

(a) the segmentation result on the plane of frame 1

(b) the segmentation result on the plane of frame 2

(c) the segmentation result on the plane of frame 3

(d) the segmentation result on the plane of frame 4

(e) the segmentation result on the plane of frame 5

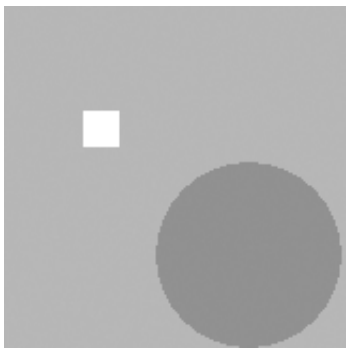

(f) the segmentation result on the plane of frame 6

Fig. 4-12 The sections of the segmented 3D bodies on each frame of the "shrinking and dilating" sequence

In order to show the segmentation results in a clearer way, the sections shown in Fig. 4-12 are overlaid together in Fig. 4-13, which can clearly show the movement of each object through the sequence. In Fig. 4-13, only the region borders in each section are shown, and the arrows indicate the shrinking or dilating of each object.

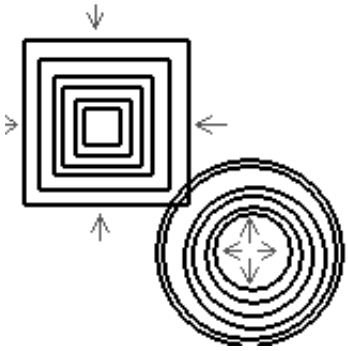

Fig. 4-13 The overlaid result of the 2D sections in Fig. 4-12

Fig. 4-14 shows the 3D segmentation result for the "deforming" sequence according to the sign distribution in Fig. 4-7, where different 3D bodies are represented by different gray-scale values for visualization. The segmented 3D bodies are shown as a series of sections in 2D form. In another word, each 2D section of the bodies on the corresponding frame plane is shown separately, and in each section the areas of different 3D bodies are of different gray-scale values.

(a) the segmentation result on the plane of frame 1

(b) the segmentation result on the plane of frame 2

(c) the segmentation result on the plane of frame 3

(d) the segmentation result on the plane of frame 4

(e) the segmentation result on the plane of frame 5

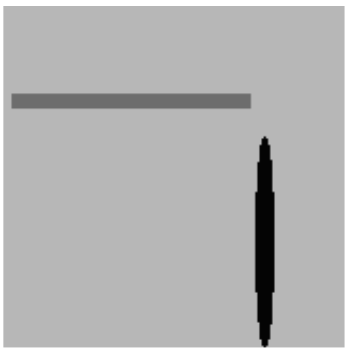

(f) the segmentation result on the plane of frame 6

Fig. 4-14 The sections of the segmented 3D bodies on each frame of the "deforming" sequence

In order to show the segmentation results in a clearer way, the sections shown in Fig. 4-14 are overlaid together in Fig. 4-15, which can clearly show the movement of each object through the sequence. In Fig. 4-15, only the region borders in each section are shown, and the arrows indicate the deforming of each object in the sequence.

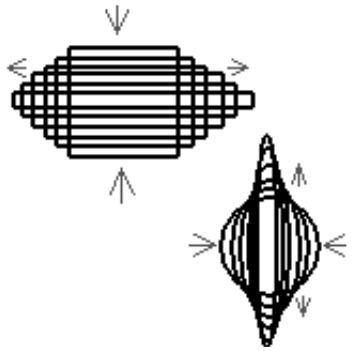

Fig. 4-15 The overlaid result of the 2D sections in Fig. 4-14

Fig. 4-16 shows the 3D segmentation result for the sequence of "combinational motion" according to the sign distribution in Fig. 4-9, where different 3D bodies are represented by different gray-scale values for visualization. The segmented 3D bodies are shown as a series of sections in 2D form. In another word, each 2D section of the bodies on the corresponding frame plane is shown separately, and in each section the areas of different 3D bodies are of different gray-scale values.

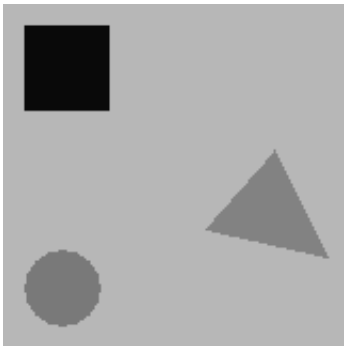

(a) the segmentation result on the plane of frame 1

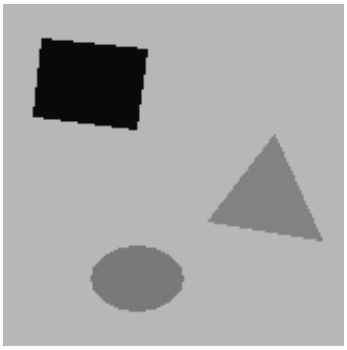

(b) the segmentation result on the plane of frame 2

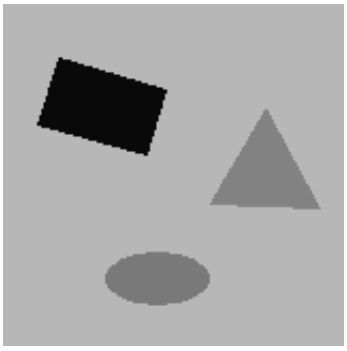

(c) the segmentation result on the plane of frame 3

(d) the segmentation result on the plane of frame 4

(e) the segmentation result on the plane of frame 5

(f) the segmentation result on the plane of frame 6

Fig. 4-16 The sections of the segmented 3D bodies on each frame of the "combinational motion" sequence

In order to show the segmentation results in a clearer way, the sections shown in Fig. 4-16 are overlaid together in Fig. 4-17, which can clearly show the movement of each object through the sequence. In Fig. 4-17, only the region borders in each section are shown, and the arrows show the moving direction of each object.

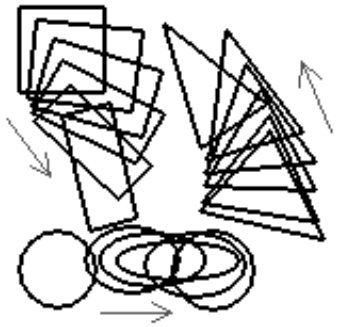

Fig. 4-17 The overlaid result of the 2D sections in Fig. 4-16

In the above experimental results, the regions of the simple objects are effectively separated from others in each single frame. Moreover, because the segmentation is implemented in the 3D space, the results are 3D bodies (or 3D volumes) in the space. Each 2D region segmented in a single frame is just a section of a corresponding 3D body. In another word, each segmented 3D body is formed by a corresponding object region which runs through the frame sequence (maybe with the movements of shifting, rotating or deforming). Therefore, the 3D segmentation result can provide a basis of object tracking for further analysis and recognition.

4.3.2 The 3D segmentation results for the real-world image sequences

To investigate the practical application of the above 3D segmentation method, experiments have also been carried out for real world image sequences. Real world image sequences are more complex than the test sequences. It is much more difficult to handle the real world images because of noise, shadow, sheltering between moving objects, etc. In this section, experiments are carried out on lots of real world sequences for several hot topics of research and application. These topics include: hand tracking and segmentation (for gesture recognition), face tracking and segmentation (for expression recognition), the tracking and segmentation of the speaker's lip (for automatic lip reading by computers), moving person tracking and segmentation (for posture recognition and human behavior identification), vehicle tracking and segmentation (for vehicle type recognition), and medical sequence segmentation. Such experiments aim at the proving of the proposed method's practical effectiveness, and also possible improvements of the method in practical use. Some of the sequences

used in the experiments are captured by the authors with a digital camera. The others are obtained from public image databases on the Internet. In the following discussion, some experiments are discussed, where the original sequences and the segmentation results are shown and analyzed.

Fig. 4-18 is the sequence of a waving hand, which has the size 160×120 for each frame. In the experiment, the sign distribution of the relative potential in the 3D space is recorded. The result is shown in a 2D form in Fig. 4-19, where the sign distribution in each frame is shown separately. According to Fig. 4-19, the main area of the moving hand can be segmented as a connected region of the same sign of relative potential. Moreover, the tracking of the hand is also possible based on the segmentation result because in the result the hand area is a connected 3D area through the sequence. The segmentation result is shown in Fig. 4-20, where the 3D result is shown in a 2D form and different areas are represented by different gray-scale values.

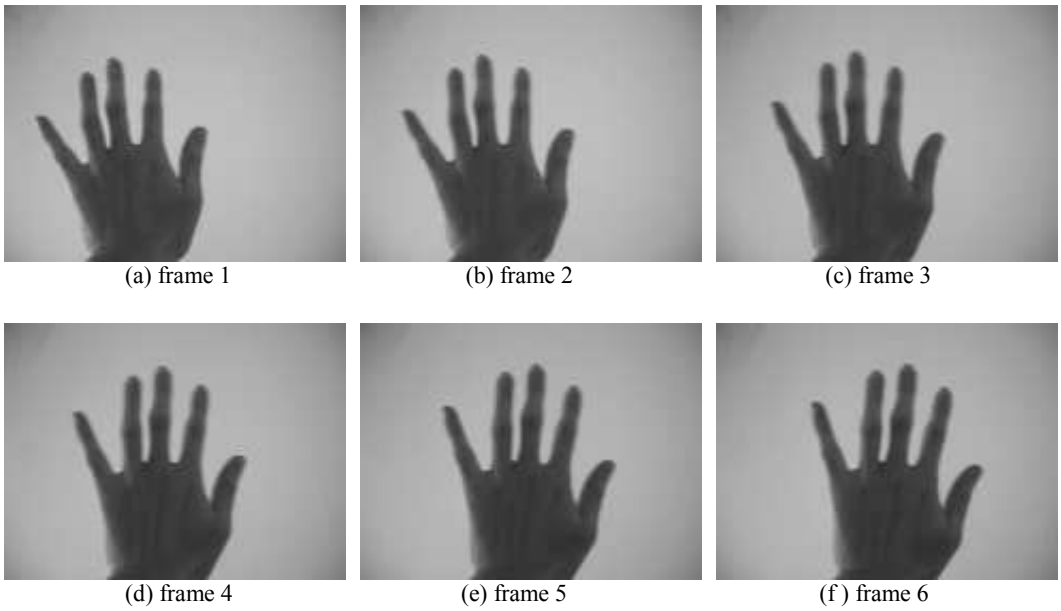

(a) frame 1 (b) frame 2 (c) frame 3

(d) frame 4 (e) frame 5 (f) frame 6

Fig. 4-18 The video sequence of a waving hand

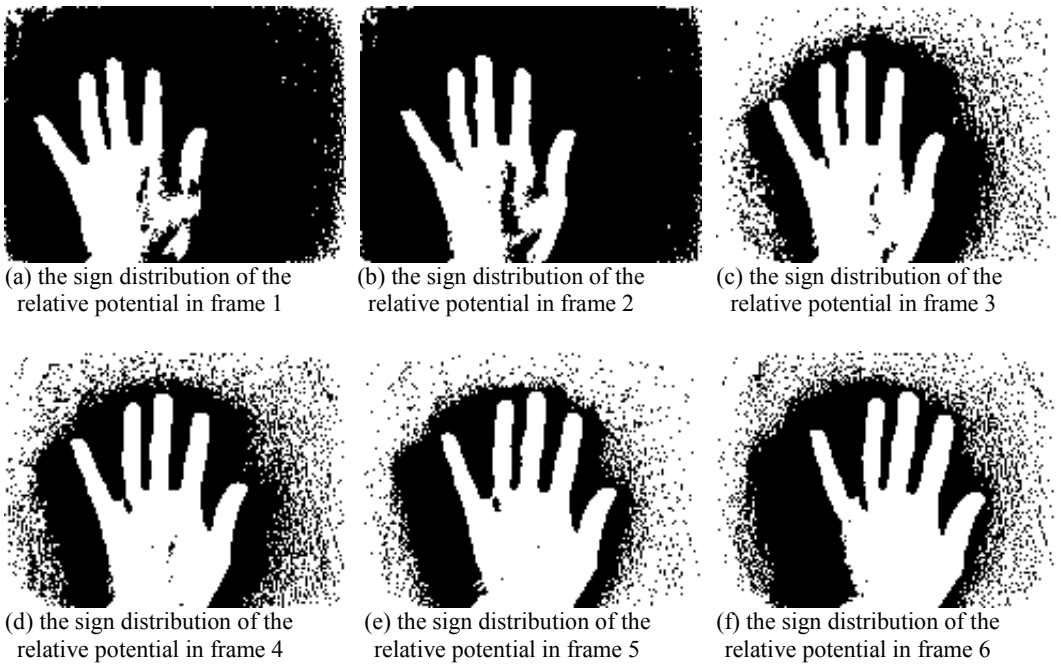

(a) the sign distribution of the relative potential in frame 1

(b) the sign distribution of the relative potential in frame 2

(c) the sign distribution of the relative potential in frame 3

(d) the sign distribution of the relative potential in frame 4

(e) the sign distribution of the relative potential in frame 5

(f) the sign distribution of the relative potential in frame 6

Fig. 4-19 The sign distribution of the relative potential values for the "waving hand" video sequence

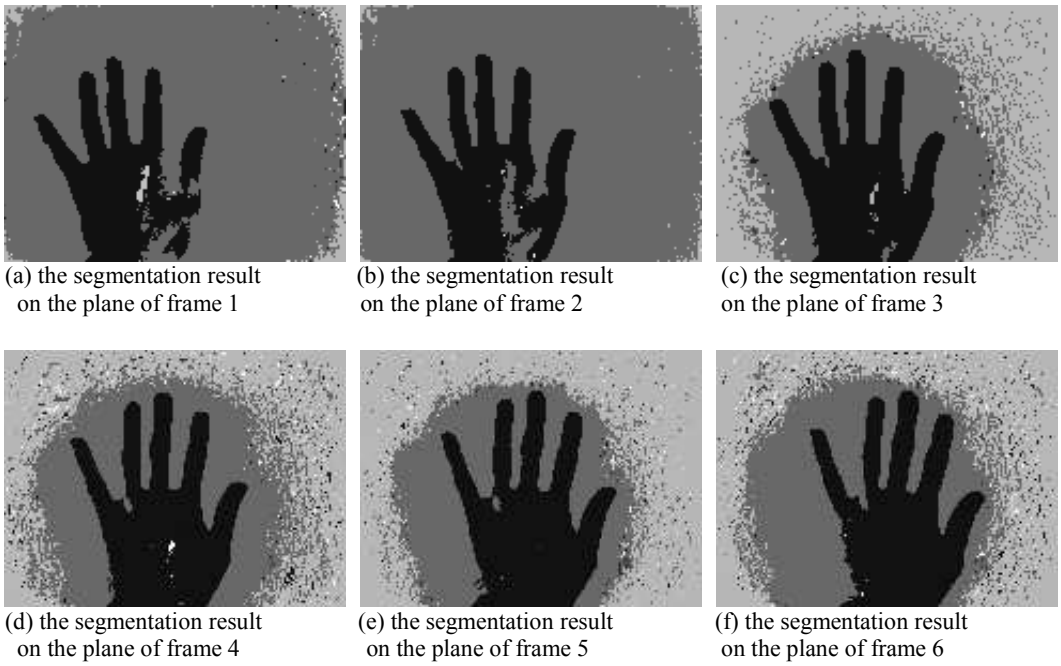

(a) the segmentation result on the plane of frame 1
(b) the segmentation result on the plane of frame 2
(c) the segmentation result on the plane of frame 3
(d) the segmentation result on the plane of frame 4
(e) the segmentation result on the plane of frame 5
(f) the segmentation result on the plane of frame 6

Fig. 4-20 The segmentation results on the plane of each frame

Fig. 4-21 is the result of extracting the hand area from each frame based on the 3D segmentation result. It is clear that the tracking of the hand can be implemented based on the result. In Fig. 4-22, the segmentation on each frame are put together to show the tracking of the hand motion in the sequence. Based on the segmentation result, further hand gesture recognition can be carried out. The behavior identification of the hand can also be studied based on the segmentation.

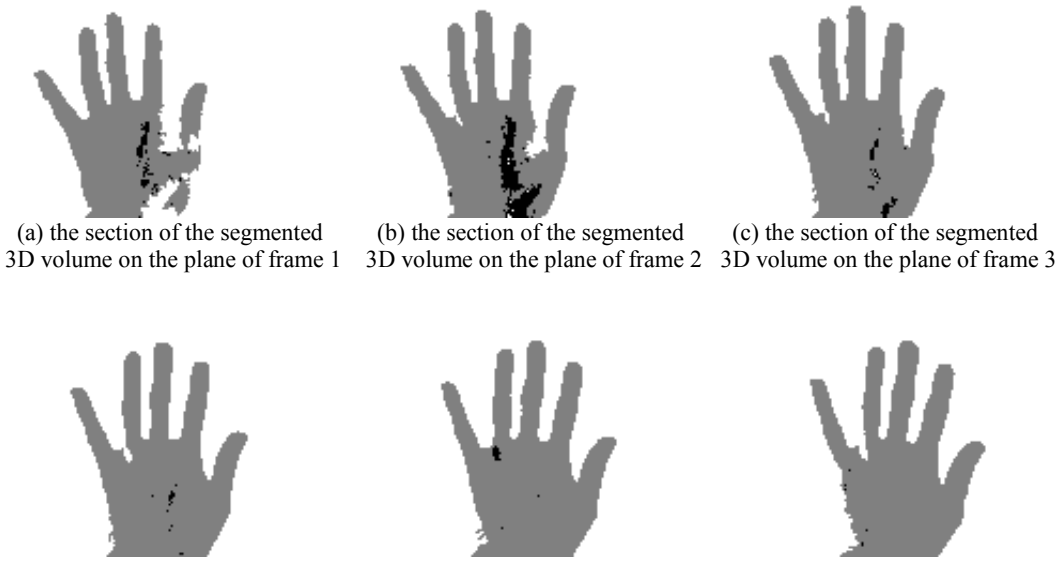

(a) the section of the segmented 3D volume on the plane of frame 1
(b) the section of the segmented 3D volume on the plane of frame 2
(c) the section of the segmented 3D volume on the plane of frame 3
(d) the section of the segmented 3D volume on the plane of frame 4
(e) the section of the segmented 3D volume on the plane of frame 5
(f) the section of the segmented 3D volume on the plane of frame 6

Fig. 4-21 The segmented hand area on the plane of each frame

Fig. 4-22 The sequence of waving hand area segmented from the video

Fig. 4-23 is the sequence of a clenching hand, which has the size 160×120 for each frame. In the experiment, the sign distribution of the relative potential in the 3D space is recorded. The result is shown in a 2D form in Fig. 4-24, where the sign distribution in each frame is shown separately. According to Fig. 4-24, the main area of the clenching hand can be segmented as a connected region of the same sign of relative potential value. Moreover, the tracking of the hand is also possible based on the segmentation result because in the result the hand area is a connected 3D area through the whole sequence. The segmentation result is shown in Fig. 4-25, where the 3D result is shown in a 2D form and different areas are represented by different gray-scale values. In Fig. 4-26, the segmentation on each frame are put together to show the tracking of the hand's clenching process. Based on the segmentation result, further hand gesture recognition can be carried out. The behavior identification of the hand can also be studied based on the segmentation.

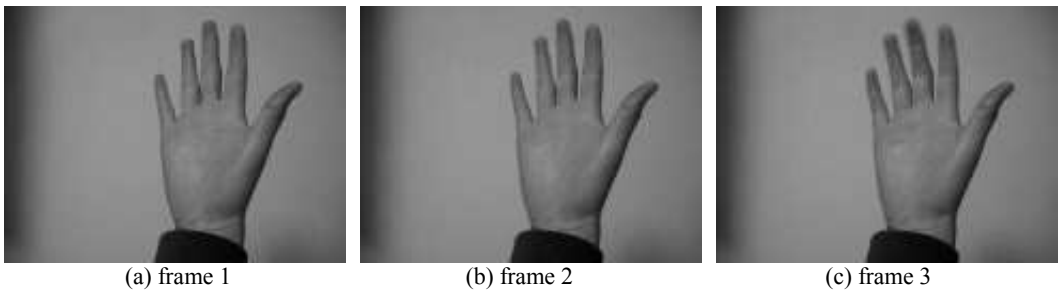

(a) frame 1 (b) frame 2 (c) frame 3

(d) frame 4 (e) frame 5 (f) frame 6

Fig. 4-23 The video sequence of a clenching hand

(a) the sign distribution of the relative potential in frame 1

(b) the sign distribution of the relative potential in frame 2

(c) the sign distribution of the relative potential in frame 3

(d) the sign distribution of the relative potential in frame 4 (e) the sign distribution of the relative potential in frame 5 (f) the sign distribution of the relative potential in frame 6

Fig. 4-24 The sign distribution of the relative potential values for the "clenching hand" video sequence

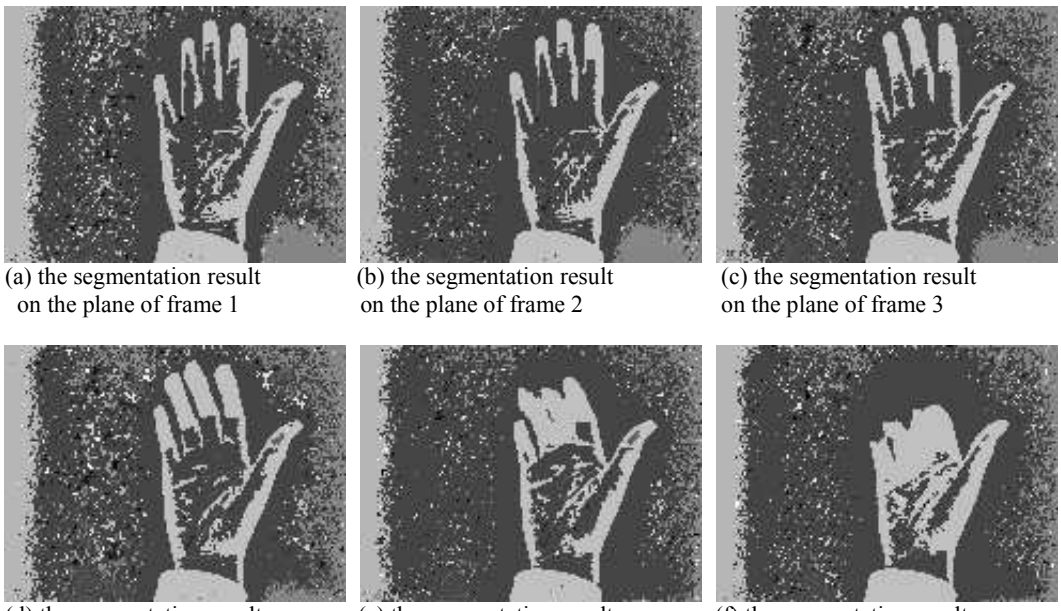

(a) the segmentation result on the plane of frame 1 (b) the segmentation result on the plane of frame 2 (c) the segmentation result on the plane of frame 3

(d) the segmentation result on the plane of frame 4 (e) the segmentation result on the plane of frame 5 (f) the segmentation result on the plane of frame 6

Fig. 4-25 The segmentation results for the "clenching hand" video sequence

Fig. 4-26 The sequence of clenching hand area segmented from the video

Fig. 4-27 is the sequence of a grabbing hand, which has the size 160×120 for each frame. In the experiment, the sign distribution of the relative potential in the 3D space is recorded. The result is shown in a 2D form in Fig. 4-28, where the sign distribution in each frame is shown separately. According to Fig. 4-28, the main area of the grabbing hand can be segmented as a connected region of the same sign of relative potential value. Moreover, the tracking of the hand is also possible based on the segmentation result because in the result the hand area is a connected 3D area through the whole sequence. The segmentation result is shown in Fig. 4-29, where the 3D result is shown in a 2D form and different areas are represented by different gray-scale values. In Fig. 4-30, the segmentation on each frame are put together to show the tracking of the hand's grabbing process. Based on the segmentation result, further hand gesture recognition can be carried out. The behavior identification of the hand can also be studied based on the segmentation result. In this sequence, the influence of the

shadow within the hand area is obvious, while the outer counter of the hand can still be determined clearly.

(a) frame 1 (b) frame 2 (c) frame 3

Fig. 4-27 The video sequence of a grabbing hand

(a) the sign distribution of the relative potential in frame 1 (b) the sign distribution of the relative potential in frame 2 (c) the sign distribution of the relative potential in frame 3

Fig. 4-28 The sign distribution of the relative potential values for the "grabbing hand" video sequence

(a) the segmentation result on the plane of frame 1 (b) the segmentation result on the plane of frame 2 (c) the segmentation result on the plane of frame 3

Fig. 4-29 The segmentation results for the "grabbing hand" video sequence

Fig. 4-30 The sequence of "grabbing hand" area segmented from the video

Fig. 4-31 is the first sequence of a TV broadcaster, which has the size 176×144 for each frame. In the experiment, the sign distribution of the relative potential in the 3D space is recorded. The result is shown in a 2D form in Fig. 4-32, where the sign distribution in each frame is shown separately. According to Fig. 4-32, the main area of the broadcaster can be segmented as several connected regions, including the hair and face. Moreover, the tracking of the face is also possible based on the segmentation result because the result includes connected 3D areas through the whole sequence. The segmentation result is shown in Fig. 4-33, where the 3D result is shown in a 2D form and different areas are represented by different gray-scale values. Especially, for the application of automatic lip

reading, in Fig. 4-34 the segmentation of the lip on each frame are put together to show the tracking of the moving lip. In Fig. 4-34, the extraction of lips is shown in both the original size and 4 times of original size for a clear view. Based on the segmentation result, further recognition can be carried out.

(a) frame 1 (b) frame 2

(c) frame 3 (d) frame 4

Fig. 4-31 The 1st video sequence of a broadcaster

(a) the sign distribution of the relative potential in frame 1

(b) the sign distribution of the relative potential in frame 2

(c) the sign distribution of the relative potential in frame 3

(d) the sign distribution of the relative potential in frame 4

Fig. 4-32 The sign distribution of the relative potential values for the 1st "broadcaster" video sequence

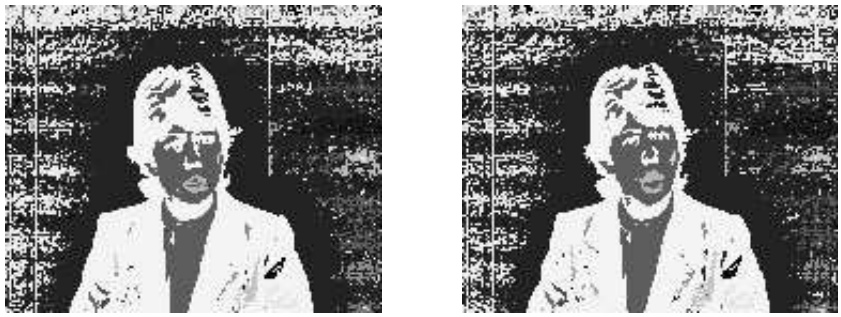

(a) the segmentation result on the plane of frame 1

(b) the segmentation result on the plane of frame 2

(c) the segmentation result on the plane of frame 3

(d) the segmentation result on the plane of frame 4

Fig. 4-33 The segmentation results for the 1st "broadcaster" video sequence

Fig. 4-34 The sequence of the moving lip segmented from the 1st "broadcaster" video sequence

Fig. 4-35 is the second sequence of a TV broadcaster, which has the size 176×144 for each frame. In the experiment, the sign distribution of the relative potential in the 3D space is recorded. The result is shown in a 2D form in Fig. 4-36, where the sign distribution in each frame is shown separately. According to Fig. 4-36, the main area of the broadcaster can be segmented as several connected regions, including the hair and face. Moreover, the tracking of the face is also possible based on the segmentation result because the result includes connected 3D areas through the whole sequence. The segmentation result is shown in Fig. 4-37, where the 3D result is shown in a 2D form and different areas are represented by different gray-scale values. Especially, for the application of automatic lip reading, in Fig. 4-38 the segmentation of the lip on each frame are put together to s show the tracking of the moving lip. Based on the segmentation result, further recognition can be carried out.

(a) frame 1 (b) frame 2

(c) frame 3 (d) frame 4

(e) frame 5 (f) frame 6

Fig. 4-35 The 2nd video sequence of the broadcaster

(a) the sign distribution of the relative potential in frame 1 (b) the sign distribution of the relative potential in frame 2

(c) the sign distribution of the relative potential in frame 3

(d) the sign distribution of the relative potential in frame 4

(e) the sign distribution of the relative potential in frame 5

(f) the sign distribution of the relative potential in frame 6

Fig. 4-36 The sign distribution of the relative potential values for the 2nd "broadcaster" video sequence

(a) the segmentation result on the plane of frame 1

(b) the segmentation result on the plane of frame 2

(c) the segmentation result on the plane of frame 3

(d) the segmentation result on the plane of frame 4

(e) the segmentation result on the plane of frame 5

(f) the segmentation result on the plane of frame 6

Fig. 4-37 The segmentation results for the 2nd "broadcaster" video sequence

Fig. 4-38 The sequence of the moving lip segmented from the 2nd "broadcaster" video sequence

Fig. 4-39 is the third sequence of a TV broadcaster, which has the size 176×144 for each frame. In the experiment, the sign distribution of the relative potential in the 3D space is recorded. The result is shown in a 2D form in Fig. 4-40, where the sign distribution in each frame is shown separately. According to Fig. 4-40, the main area of the broadcaster can be segmented as several connected regions, including the hair and face. Moreover, the tracking of the face is also possible based on the segmentation result because the result includes connected 3D areas through the whole sequence. The segmentation result is shown in Fig. 4-41, where the 3D result is shown in a 2D form and different areas are represented by different gray-scale values. Especially, for the application of automatic lip reading, in Fig. 4-42 the segmentation of the lip on each frame are put together to show the tracking of the moving lip. Based on the segmentation result, further recognition can be carried out.

(a) frame 1

(b) frame 2

(c) frame 3

(d) frame 4

(e) frame 5

(f) frame 6

Fig. 4-39 The 3rd video sequence of the broadcaster

(a) the sign distribution of the relative potential in frame 1

(b) the sign distribution of the relative potential in frame 2

(c) the sign distribution of the relative potential in frame 3

(d) the sign distribution of the relative potential in frame 4

(e) the sign distribution of the relative potential in frame 5

(f) the sign distribution of the relative potential in frame 6

Fig. 4-40 The sign distribution of the relative potential values for the 3rd "broadcaster" video sequence

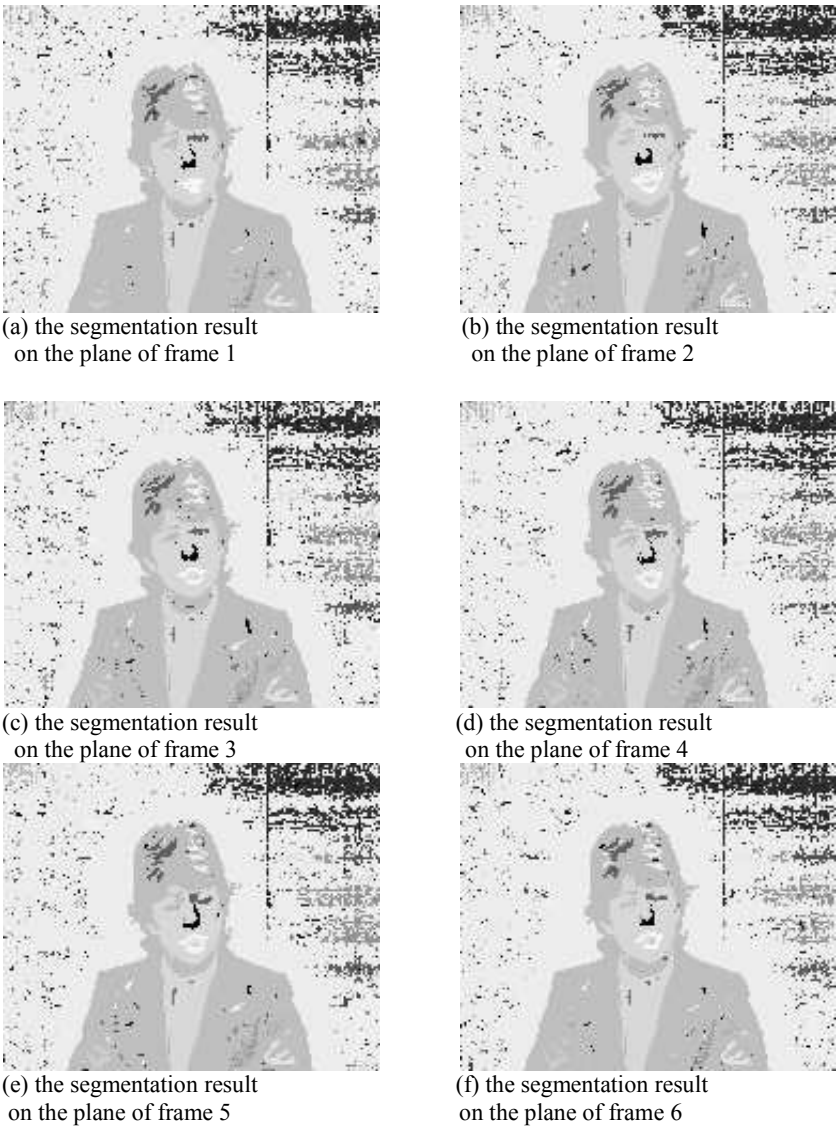

(a) the segmentation result on the plane of frame 1

(b) the segmentation result on the plane of frame 2

(c) the segmentation result on the plane of frame 3

(d) the segmentation result on the plane of frame 4

(e) the segmentation result on the plane of frame 5

(f) the segmentation result on the plane of frame 6

Fig. 4-41 The segmentation results for the 3rd "broadcaster" video sequence

Fig. 4-42 The sequence of the moving lip segmented from the 3rd "broadcaster" video sequence

Fig. 4-43 is the forth sequence of a TV broadcaster, which has the size 176×144 for each frame. In the experiment, the sign distribution of the relative potential in the 3D space is recorded. The result is shown in a 2D form in Fig. 4-44, where the sign distribution in each frame is shown separately. According to Fig. 4-44, the main area of the broadcaster can be segmented as several connected regions, including the hair and face. Moreover, the tracking of the face is also possible based on the segmentation result because the result includes connected 3D areas through the whole sequence. The segmentation result is shown in Fig. 4-45, where the 3D result is shown in a 2D form and different

areas are represented by different gray-scale values. Especially, for the application of automatic lip reading, in Fig. 4-46 the segmentation of the lip on each frame are put together to show the tracking of the moving lip. Based on the segmentation result, further recognition can be carried out.

(a) frame 1 (b) frame 2

(c) frame 3 (d) frame 4

(e) frame 5 (f) frame 6

Fig. 4-43 The 4th video sequence of the broadcaster

(a) the sign distribution of the relative potential in frame 1

(b) the sign distribution of the relative potential in frame 2

(c) the sign distribution of the relative potential in frame 3

(d) the sign distribution of the relative potential in frame 4

(e) the sign distribution of the relative potential in frame 5

(f) the sign distribution of the relative potential in frame 6

Fig. 4-44 The sign distribution of the relative potential values for the 4th "broadcaster" video sequence

(a) the segmentation result on the plane of frame 1

(b) the segmentation result on the plane of frame 2

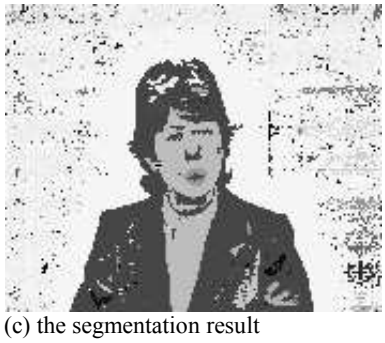

(c) the segmentation result on the plane of frame 3

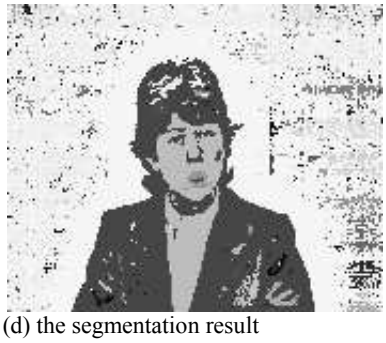

(d) the segmentation result on the plane of frame 4

(e) the segmentation result on the plane of frame 5

(f) the segmentation result on the plane of frame 6

Fig. 4-45 The segmentation results for the 4th "broadcaster" video sequence

Fig. 4-46 The sequence of the moving lip segmented from the 4th "broadcaster" video sequence

Fig. 4-47 is the first sequence of another TV broadcaster, which has the size 176×144 for each frame. In the experiment, the sign distribution of the relative potential in the 3D space is recorded. The result is shown in a 2D form in Fig. 4-48, where the sign distribution in each frame is shown separately. According to Fig. 4-48, the main area of the broadcaster can be segmented as several connected regions including the face. Moreover, the tracking of the face is also possible based on the segmentation result because the result includes connected 3D areas through the whole sequence. The segmentation result is shown in Fig. 4-49, where the 3D result is shown in a 2D form and different areas are represented by different gray-scale values. Especially, for the application of automatic expression recognition, in Fig. 4-50 the segmentation of the face on each frame are put together to show the tracking of the face in the sequence. The segmentations of the lip in each frame are also put together in Fig. 4-51. Based on the segmentation results, further recognition can be carried out.

(a) frame 1

(b) frame 2

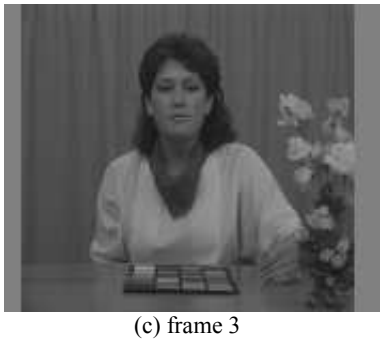

(c) frame 3

(d) frame 4

(e) frame 5

(f) frame 6

Fig. 4-47 The 1st video sequence of a TV presenter

(a) the sign distribution of the relative potential in frame 1

(b) the sign distribution of the relative potential in frame 2

(c) the sign distribution of the relative potential in frame 3

(d) the sign distribution of the relative potential in frame 4

(e) the sign distribution of the relative potential in frame 5

(f) the sign distribution of the relative potential in frame 6

Fig. 4-48 The sign distribution of the relative potential values for the 1st "TV presenter" video sequence

(a) the segmentation result on the plane of frame 1

(b) the segmentation result on the plane of frame 2

(c) the segmentation result on the plane of frame 3

(d) the segmentation result on the plane of frame 4

(e) the segmentation result on the plane of frame 5

(f) the segmentation result on the plane of frame 6

Fig. 4-49 The segmentation results for the 1st "TV presenter" video sequence

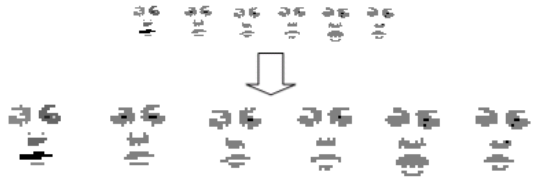

Fig. 4-50 The sequence of the face (including eyebrows, eyes, nose and lip) segmented from the 1st video of the TV presenter

Fig. 4-51 The sequence of the moving lip segmented from the 1st video of the TV presenter

Fig. 4-52 is the second sequence of the TV broadcaster, which has the size 176×144 for each frame. In the experiment, the sign distribution of the relative potential in the 3D space is recorded. The result is shown in a 2D form in Fig. 4-53, where the sign distribution in each frame is shown separately. According to Fig. 4-53, the main area of the broadcaster can be segmented as several connected regions including the face. Moreover, the tracking of the face is also possible based on the segmentation result because the result includes connected 3D areas through the whole sequence. The segmentation result is shown in Fig. 4-54, where the 3D result is shown in a 2D form and different areas are represented by different gray-scale values. Especially, for the application of automatic expression recognition, in Fig. 4-55 the segmentation of the face on each frame are put together to show the tracking of the face in the sequence. The segmentations of the lip in each frame are also put together in Fig. 4-56. Based on the segmentation results, further recognition can be carried out.

(a) frame 1

(b) frame 2

(c) frame 3

(d) frame 4

(e) frame 5

(f) frame 6

Fig. 4-52 The 2nd video sequence of a TV presenter

(a) the sign distribution of the relative potential in frame 1

(b) the sign distribution of the relative potential in frame 2

(c) the sign distribution of the relative potential in frame 3

(d) the sign distribution of the relative potential in frame 4

(e) the sign distribution of the relative potential in frame 5

(f) the sign distribution of the relative potential in frame 6

Fig. 4-53 The sign distribution of the relative potential values for the 2nd video sequence of a TV presenter

(a) the segmentation result on the plane of frame 1

(b) the segmentation result on the plane of frame 2

(c) the segmentation result on the plane of frame 3

(d) the segmentation result on the plane of frame 4

(e) the segmentation result on the plane of frame 5

(f) the segmentation result on the plane of frame 6

Fig. 4-54 The segmentation results for the 2nd video sequence of a TV presenter

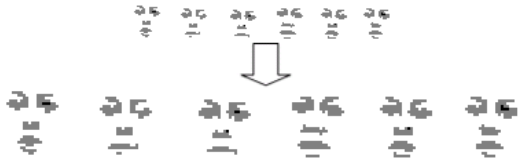

Fig. 4-55 The sequence of the face (including eyebrows, eyes, nose and lip) segmented from the 2nd video of the TV presenter

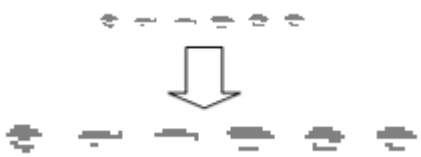

Fig. 4-56 The sequence of the moving lip segmented from the 2nd video of the TV presenter

Fig. 4-57 is the third sequence of the TV broadcaster, which has the size 176×144 for each frame. In the experiment, the sign distribution of the relative potential in the 3D space is recorded. The result is shown in a 2D form in Fig. 4-58, where the sign distribution in each frame is shown separately. According to Fig. 4-58, the main area of the broadcaster can be segmented as several connected regions including the face. Moreover, the tracking of the face is also possible based on the segmentation result because the result includes connected 3D areas through the whole sequence. The segmentation result is shown in Fig. 4-59, where the 3D result is shown in a 2D form and different areas are represented by different gray-scale values. Especially, for the application of automatic expression recognition, in Fig. 4-60 the segmentation of the face on each frame are put together to show the tracking of the face in the sequence. The segmentations of the lip in each frame are also put together in Fig. 4-61. Based on the segmentation results, further recognition can be carried out.

(a) frame 1 (b) frame 2

(c) frame 3 (d) frame 4

(e) frame 5 (f) frame 6

Fig. 4-57 The 3rd video sequence of a TV presenter

(a) the sign distribution of the relative potential in frame 1

(b) the sign distribution of the relative potential in frame 2

(c) the sign distribution of the relative potential in frame 3

(d) the sign distribution of the relative potential in frame 4

(e) the sign distribution of the relative potential in frame 5

(f) the sign distribution of the relative potential in frame 6

Fig. 4-58 The sign distribution of the relative potential values for the 3rd video of the TV presenter

(a) the segmentation result on the plane of frame 1

(b) the segmentation result on the plane of frame 2

(c) the segmentation result on the plane of frame 3

(d) the segmentation result on the plane of frame 4

(e) the segmentation result on the plane of frame 5

(f) the segmentation result on the plane of frame 6

Fig. 4-59 The segmentation results for the 3rd video of the TV presenter

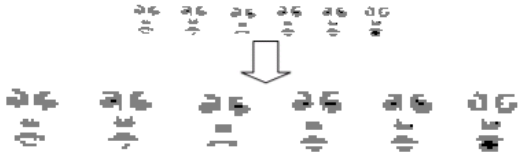

Fig. 4-60 The sequence of the face (including eyebrows, eyes, nose and lip) segmented from the 3rd video of the TV presenter

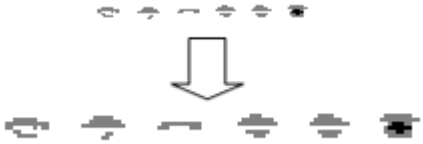

Fig. 4-61 The sequence of the moving lip segmented from the 3rd video of the TV presenter

Fig. 4-62 is the forth sequence of the TV broadcaster, which has the size 176×144 for each frame. In the experiment, the sign distribution of the relative potential in the 3D space is recorded. The result is shown in a 2D form in Fig. 4-63, where the sign distribution in each frame is shown separately. According to Fig. 4-63, the main area of the broadcaster can be segmented as several connected regions including the face. Moreover, the tracking of the face is also possible based on the segmentation result because the result includes connected 3D areas through the whole sequence. The segmentation result is shown in Fig. 4-64, where the 3D result is shown in a 2D form and different areas are represented by different gray-scale values. Especially, for the application of automatic expression recognition, in Fig. 4-65 the segmentation of the face on each frame are put together to show the tracking of the face in the sequence. The segmentations of the lip in each frame are also put together in Fig. 4-66. Based on the segmentation results, further recognition can be carried out.

(a) frame 1

(b) frame 2

(c) frame 3

(d) frame 4

(e) frame 5

(f) frame 6

Fig. 4-62 The video sequence of the 4th video of the TV presenter

(a) the sign distribution of the relative potential in frame 1

(b) the sign distribution of the relative potential in frame 2

(c) the sign distribution of the relative potential in frame 3

(d) the sign distribution of the relative potential in frame 4

(e) the sign distribution of the relative potential in frame 5

(f) the sign distribution of the relative potential in frame 6

Fig. 4-63 The sign distribution of the relative potential values for the 4th video of the TV presenter

(a) the segmentation result on the plane of frame 1

(b) the segmentation result on the plane of frame 2

(c) the segmentation result on the plane of frame 3

(d) the segmentation result on the plane of frame 4

(e) the segmentation result on the plane of frame 5

(f) the segmentation result on the plane of frame 6

Fig. 4-64 The segmentation results for the 4th video of the TV presenter

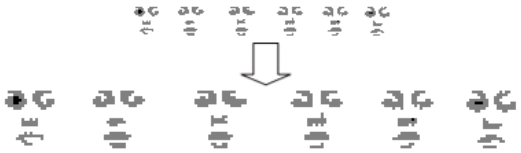

Fig. 4-65 The sequence of the face (including eyebrows, eyes, nose and lip) segmented from the 4th video of the TV presenter

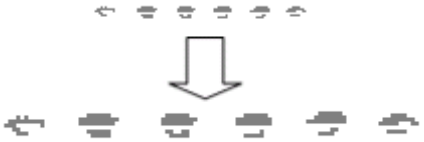

Fig. 4-66 The sequence of the moving lip segmented from the 4th video of the TV presenter

Fig. 4-67 is the sequence of a person raising his arms, which has the size 160×120 for each frame. In the experiment, the sign distribution of the relative potential in the 3D space is recorded. The result is shown in a 2D form in Fig. 4-68, where the sign distribution in each frame is shown separately. According to Fig. 4-68, the main area of the person can be segmented as a connected region with the same sign of the relative potential value. Moreover, the tracking of the person's action is also possible based on the segmentation result because the result includes connected 3D area of the person through the whole sequence. The segmentation result is shown in Fig. 4-69, where the 3D result is shown in a 2D form and different areas are represented by different gray-scale values. For the application of automatic posture and behavior recognition, in Fig. 4-70 the segmentation of the person on each frame are put together to show the tracking of his action in the sequence. Based on the segmentation results, further recognition can be carried out.

(a) frame 1

(b) frame 2

(c) frame 3

(d) frame 4

(e) frame 5

Fig. 4-67 The video sequence of a person raising the arms

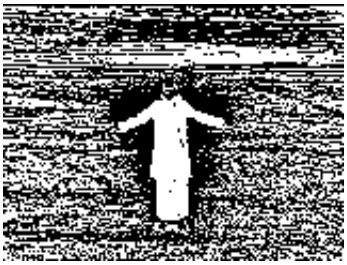

(a) the sign distribution of the relative potential in frame 1

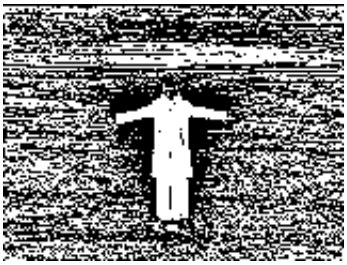

(b) the sign distribution of the relative potential in frame 2

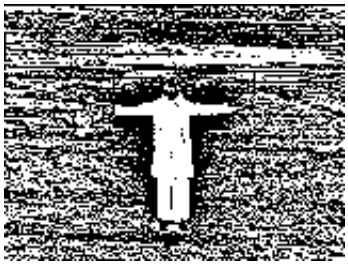

(c) the sign distribution of the relative potential in frame 3

(d) the sign distribution of the relative potential in frame 4

(e) the sign distribution of the relative potential in frame 5

Fig. 4-68 The sign distribution of the relative potential values for the "raising arms" video sequence

(a) the segmentation result on the plane of frame 1

(b) the segmentation result on the plane of frame 2

(c) the segmentation result on the plane of frame 3

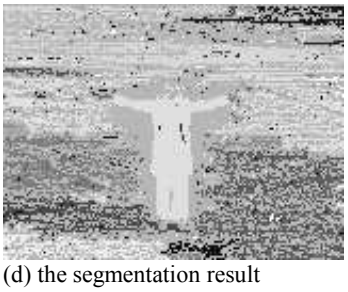

(d) the segmentation result on the plane of frame 4

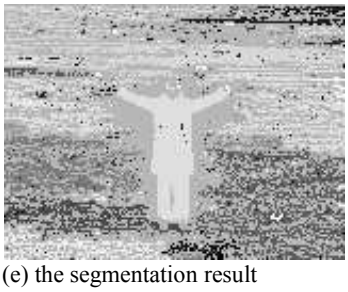

(e) the segmentation result on the plane of frame 5

Fig. 4-69 The segmentation results for the "raising arms" video sequence

Fig. 4-70 The sequence of the "raising arms" action segmented from the video

Fig. 4-71 is the sequence of a running person, which has the size 160×120 for each frame. In the experiment, the sign distribution of the relative potential in the 3D space is recorded. The result is shown in a 2D form in Fig. 4-72, where the sign distribution in each frame is shown separately. According to Fig. 4-72, the main area of the person can be segmented as a connected region with the same sign of the relative potential value. Moreover, the tracking of the person's action is also possible based on the segmentation result because the result includes connected 3D area of the person through the whole sequence. The segmentation result is shown in Fig. 4-73, where the 3D result is shown in a 2D form and different areas are represented by different gray-scale values. For the application of automatic posture and behavior recognition, in Fig. 4-74 the segmentation of the person on each frame are put together to show the tracking of his action in the sequence. Based on the segmentation results, further recognition can be carried out.

(a) frame 1 (b) frame 2 (c) frame 3

Fig. 4-71 The video sequence of a running person

(a) the sign distribution of the relative potential in frame 1 (b) the sign distribution of the relative potential in frame 2 (c) the sign distribution of the relative potential in frame 3

Fig. 4-72 The sign distribution of the relative potential values for the "running" video sequence

(a) the segmentation result on the plane of frame 1 (b) the segmentation result on the plane of frame 2 (c) the segmentation result on the plane of frame 3

Fig. 4-73 The segmentation results for the "running" video sequence

Fig. 4-74 The sequence of the running person segmented from the video

Fig. 4-75 is a traffic sequence, which has the size 160×120 for each frame. In the experiment, the sign distribution of the relative potential in the 3D space is recorded. The result is shown in a 2D form in Fig. 4-76, where the sign distribution in each frame is shown separately. According to Fig. 4-76, the main area of the car at the front can be segmented as a connected region with the same sign of the relative potential. The tracking of the front car is possible based on the segmentation result because the result includes connected 3D area of the car through the whole sequence. The segmentation result is shown in Fig. 4-77, where the 3D result is shown in a 2D form and different areas are represented by different gray-scale values. For the application of automatic car tracking, in Fig. 4-78 and Fig. 4-79 the segmentations of the front car in each frame are put together to show the vertical and horizontal movement respectively. In Fig. 4-78, the vertical positions of the car in each frame are kept unchanged to show the vertical translation through the sequence. In Fig. 4-79, the horizontal positions of the car in each frame are kept unchanged to show the horizontal translation through the sequence. Then the movement of the car can be estimated for further analysis.

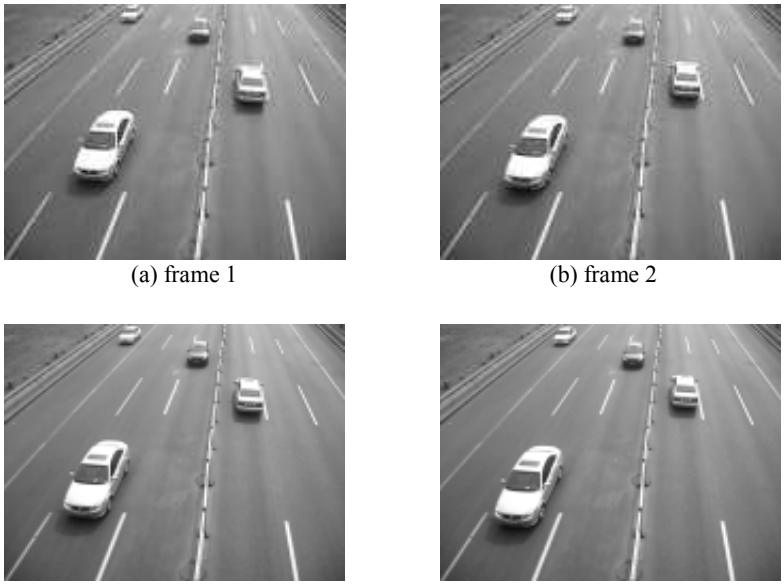

(a) frame 1 (b) frame 2

(c) frame 3 (d) frame 4

Fig. 4-75 A traffic video sequence

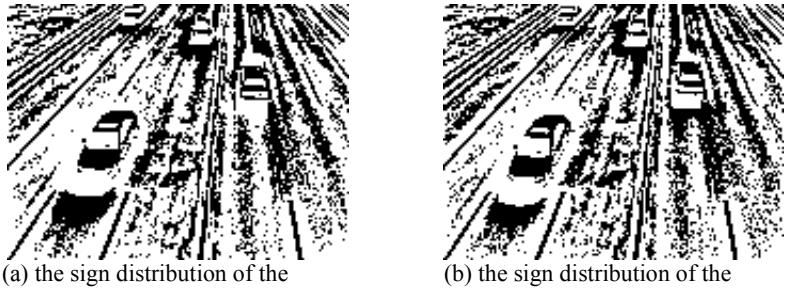

(a) the sign distribution of the relative potential in frame 1

(b) the sign distribution of the relative potential in frame 2

(c) the sign distribution of the relative potential in frame 3

(d) the sign distribution of the relative potential in frame 4

Fig. 4-76 The sign distribution of the relative potential values for the traffic video sequence

(a) the segmentation result on the plane of frame 1

(b) the segmentation result on the plane of frame 2

(c) the segmentation result on the plane of frame 3

(d) the segmentation result on the plane of frame 4

Fig. 4-77 The segmentation results for the traffic video sequence

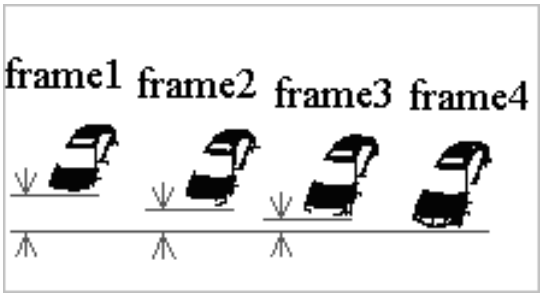

Fig. 4-78 The segmented car and the change of its vertical position in the image sequence

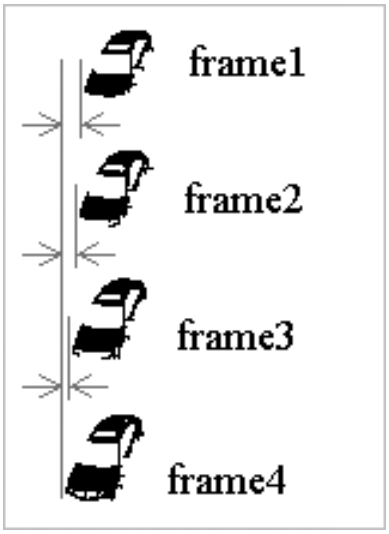

Fig. 4-79 The segmented car and the change of its horizontal position in the image sequence

Fig. 4-80 shows two frames of a ping-pong sequence, which has the size 176×120 for each frame. In the experiment, the sign distribution of the relative potential in the 3D space is recorded. The result is shown in a 2D form in Fig. 4-81, where the sign distribution in each frame is shown separately. The segmentation result is shown in Fig. 4-82, where the 3D result is shown in a 2D form and different areas are represented by different gray-scale values. Because it is obvious that there is much noise in the original images, the segmentation results have many small areas. Moreover, some regions of interest (such as the arm and the bat) are connected to the background noise areas. Nevertheless, the ball and some part of the hand can still be extracted according to Fig. 4-82, which is shown in Fig. 4-83. In Fig. 4-83, it is obvious that the vertical translation of the ball can be estimated for further analysis.

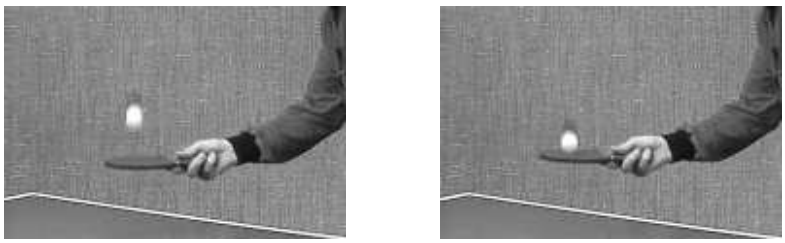

(a) frame 1 (b) frame 2

Fig. 4-80 Two frames of the "table tennis" video

(a) the sign distribution of the relative potential in frame 1

(b) the sign distribution of the relative potential in frame 2

Fig. 4-81 The sign distribution of the relative potential values for the "table tennis" video sequence

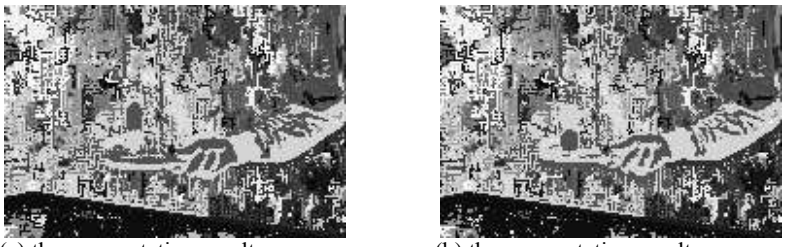

(a) the segmentation result on the plane of frame 1

(b) the segmentation result on the plane of frame 2

Fig. 4-82 The segmentation results for the "table tennis" video sequence

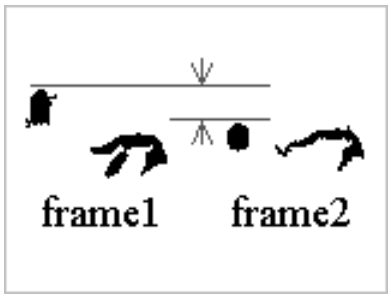

Fig. 4-83 The comparison of the ball's vertical position segmented from the "table tennis" video

Fig. 4-84 shows three frames of a CT image sequence obtained from a public medical image database on the Internet for research use. The sequence has the size 192×192 for each frame. Fig. 4-85 shows the sign distribution of the 3D relative potential field in a 2D form, where different 3D bodies are represented by different gray-scale values. The segmented 3D bodies are shown as a series of sections in 2D form in Fig. 4-86. In another word, each 2D section of the bodies on the corresponding frame plane is shown separately as 2D image, and in each section the areas of different bodies are of different gray-scale values.

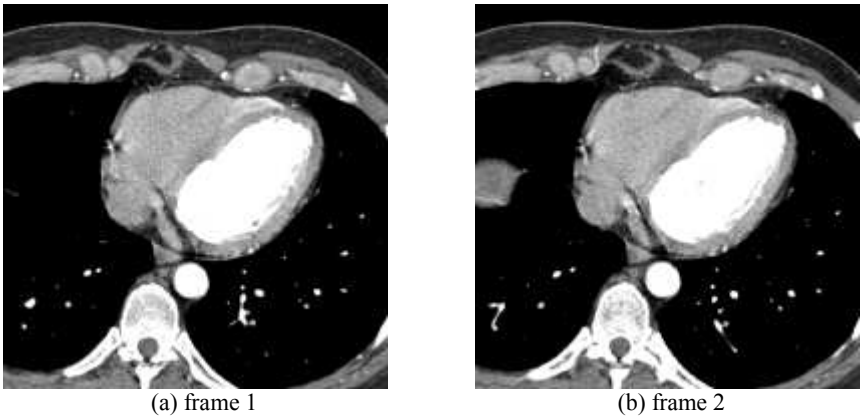

(a) frame 1

(b) frame 2

(c) frame 3

Fig. 4-84 Three frames from a CT image sequence

(a) the sign distribution of the relative potential in frame 1

(b) the sign distribution of the relative potential in frame 2

(c) the sign distribution of the relative potential in frame 3

Fig. 4-85 The sign distribution of the 3D relative potential field

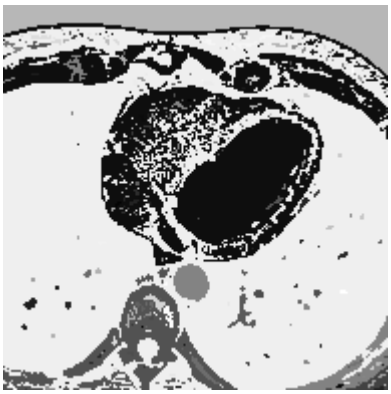

(a) the segmentation result
on the plane of frame 1

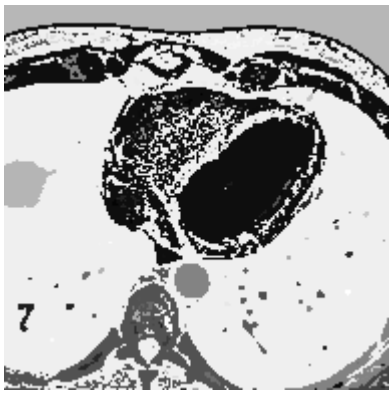

(b) the segmentation result
on the plane of frame 2

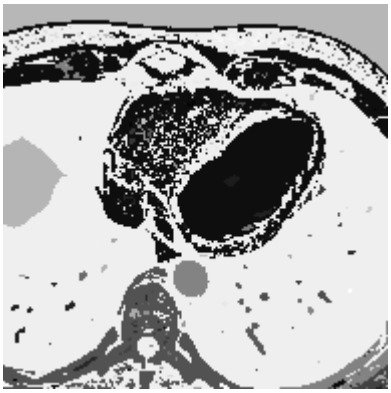

(c) the segmentation result
on the plane of frame 3

Fig. 4-86 The segmentation result according to Fig. 4-85

In this chapter, plenty of experimental results are shown for the study of 3D relative potential analysis on image sequences. The above experimental results indicate that the relative potential field of 3D image sequences can serve as a natural representation of 3D region border for object division. Moreover, the segmented 3D bodies from the sequence provide a convenient way for object tracking and analysis. The effectiveness of the relative potential method is based on some unique characteristics of its mathematical form, which serves as a suitable model for the representation of the local-global relevance between image points. The structure information of the sequence can be revealed by the relative potential transform. The sign distribution of the relative potential values can serve as the feature of 3D region border, based on which image sequence segmentation can be performed.

5 Relative Field Method on Color Image Processing

Color image processing is an important branch of digital image processing[97-103]. Nowadays, color image can be obtained conveniently by many types of image capture devices. Color images are widely applied in research, industry, medicine, etc. The gray-scale value (or brightness, intensity) of a pixel can be derived from its color. The color has more information, based on which more accurate and effective processing results may be obtained. Therefore, color image processing has attracted more and more research interest and efforts.

Currently, many existing processing methods are for gray-scale images. It is of much practical importance to extend such methods to color image processing, or study novel methods for color images considering their special characteristics. The extension from gray-scale processing to color involves the increasing of the data dimension (i.e. from scalar grayscale to three-dimensional color space such as RGB or HSI). The increasing of the data amount in color images also brings about new requirements for processing methods.

In recent years, the physical field inspired methods have achieved promising results for image processing tasks such as image segmentation, biometrics, corner detection, etc[3,17,19,22,69-74]. The idea of regarding a digital image as a virtual field imitating the physical field gives a natural way of image structure presentation and decomposition for further analysis. Moreover, the novel representation may reveal new features useful in practical tasks. The electro-magnetic field in physics has a complete set of theoretical descriptions (a series of laws and theorems)[75-78]. There are on-going researches to explore the practical use of the methods imitating the electro-magnetic rules in signal and image analysis. In this research direction, existing methods focus on grayscale image processing, and there is a practical need of extending such promising methods to color image processing.

In previous research work, the authors have presented a series of novel methods inspired by electro-magnetics for gray-scale image analysis. In this chapter, the extension of such methods from gray-scale processing to color image is studied. Since the “relative field” methods mentioned in Chapter 4 have similarity in their definition, they may be extended to color image processing in a similar way. The key idea underlying the “relative field” is introducing the measurement of pixel difference in their definitions. Therefore, the key problem of extending the “relative field” methods from grayscale to color image processing is the definition of the measurement of color difference.

In this chapter, a novel measurement of color difference in the RGB space is presented. The relative potential field for color image analysis is presented, which is a typical case of extending the “relative field” methods. The spatial feature of the color relative potential is discussed theoretically and investigated by experiments on a series of color images, which is then applied in color image segmentation. Moreover, the brightness normalization is presented to eliminate the influence of shading and sheltering.

5.1 The definition of the relative potential for color images

In physics, the electro-static potential is determined by the source (i.e. the charge distribution). Therefore, the potential field can reflect some characteristics of the source. This relationship between the field and its source can be exploited in image transform, in which the image is regarded as the source (i.e. the pixels are regarded as discrete charges) and the generated virtual field may reveal important features of the image. In this chapter, a general form of virtual potential field for digital images (both gray-scale and color images) is presented.

5.1.1 A general form of virtual potential field for 2D images

The formula of the physical electro-static potential generated by a charge q is as following[75-78]:

$$V = \frac{1}{4\pi\varepsilon} \cdot \frac{q}{r} \tag{5-1}$$

where V is the electro-static potential at a space point. q is the charge quantity. r is the distance between the charge and the space point. ε is a physical constant.
For a charge distribution ρ in the space, the potential generated by ρ on the point (x,y) is as following[75-78]:

$$V = \frac{1}{4\pi\varepsilon} \int_V \frac{\rho \cdot d\tau}{r} \tag{5-2}$$

where V is the electro-static potential at a space point. The integral in Equation (5-2) is for the whole region where the charge distribution ρ exists.

Imitating the physical electro-static field, a general form of virtual potential for digital images (both color and grayscale images) is presented. For image analysis, not only the distance between two image points but also the relationship between their optical characteristics (such as the color) should be considered. Therefore, a general continuous form of image virtual potential is proposed as:

$$V_c^m(x,y) = A \cdot \int_a \int_b \frac{f(h(a,b),h(x,y))}{r_{(a,b)\to(x,y)}^m} da \cdot db \tag{5-3}$$

where $V_c^m(x,y)$ is the continuous image potential value on point (x,y). A is a predefined constant value. h is the optical characteristics (such as the color) of image points. f is a function defined according to specific image processing tasks, which represents the relationship between the gray-scale values of point (x,y) and (a,b). r is the distance between (x,y) and (a,b). m is a constant that affect the reciprocal's decreasing rate with the increasing distance r. The double integral in Equation (5-3) is on the two-dimensional image plane. For a specific processing task, the function f and the constants A, m should be pre-defined according to the specific processing purpose.

For digital images, the general discrete form of image virtual potential is proposed as the discrete form of Equation (5-3):

$$V_d^m(x,y) = A \cdot \sum_{\substack{j=0 \\ (j\neq y \text{ or } i\neq x)}}^{H-1} \sum_{i=0}^{W-1} \frac{f(h(i,j),h(x,y))}{r_{(i,j)\to(x,y)}^m} \tag{5-4}$$

where $V_d^m(x,y)$ is the discrete image potential on point (x,y). A is a predefined constant value. H and W are the height and width of the digital image respectively. h is the optical characteristic (such as the color) of image points. f is a function defined according to specific image processing tasks, which represents the relationship between the optical characteristic values of point (x,y) and (i,j). r is the distance between (x,y) and (i,j). m is a constant that affect the reciprocal's decreasing rate with the increasing distance r.

5.1.2 The relative potential field for color images

For some important image processing tasks such as segmentation and edge detection, the difference between pixel values are the factor of major consideration. Therefore, the relative potential field for images is defined based on the general form of discrete image potential, where the function $f(h(i,j), h(x,y))$ is specialized as the difference between the optical characteristics (such as the color) of the two image points (x,y) and (i,j):

$$V_R^m(x,y) = A \cdot \sum_{\substack{j=0 \\ (j\neq y \text{ or } i\neq x)}}^{H-1} \sum_{i=0}^{W-1} \frac{Difference(h(i,j),h(x,y))}{r_{(i,j)\to(x,y)}^m} \tag{5-5}$$

where $V_R^m(x,y)$ is the relative potential value of point (x,y). A is a predefined constant value. H and W are the height and width of the image respectively. *Difference*($h(i,j)$, $h(x,y)$) is the difference of pixel value h (color or grayscale), which is a scalar measuring the degree of difference between the two pixels. r is the distance between (x,y) and (i,j). m is a constant that affect the reciprocal's decreasing rate with the increasing distance r.

For gray-scale images, the *Difference*($h(i,j)$, $h(x,y)$) is naturally $g(i,j)$-$g(x,y)$ (g is the grayscale value). The grayscale relative potential is as following:

$$V_R^m(x,y) = A \cdot \sum_{\substack{j=0 \\ (j\neq y \text{ or } i\neq x)}}^{H-1} \sum_{i=0}^{W-1} \frac{g(i,j)-g(x,y)}{r_{(i,j)\to(x,y)}^m} \tag{5-6}$$

where $V_R^m(x,y)$ is the relative potential of the grayscale image on point (x,y). A is a predefined constant value. H and W are the height and width of the digital image respectively. g is the gray-scale value of image points. r is the distance between (x,y) and (i,j). m is a constant that affect the reciprocal's decreasing rate with the increasing distance r. Such definition for gray-scale images has been studied in Section 2.1.1.

For color images, because the color value is usually defined as a vector (such as RGB, HSI, etc.), the definition of the difference between pixels should be extended and re-defined. In this chapter, a novel measurement of color difference in RGB space is presented, based on which the color relative potential is defined for color image analysis.

In order to extend the relative potential to color images, a scalar is needed to measure the difference of two colors in the three-dimensional RGB space. Here the proposed color difference measurement is presented as the extension of grayscale difference. The difference of two grayscale values g_1, g_2 is a scalar: *Difference*(g_1, g_2)=g_1-g_2. The difference has two factors: one is the sign, the other is its absolute value. The absolute value represents the degree of grayscale difference. The meaning of the sign can be considered as the relative order of the two grayscale values in an ordered set of all the possible grayscale values. In another word, all the possible discrete grayscale values form an ordered set with their natural value order from small to large. The sign of g_1-g_2 is '+' (i.e. positive) when g_1 comes after g_2 in the ordered set. Otherwise, the sign is '-' (i.e. negative) when g_1 comes before g_2 in the ordered set.

Based on the above discussion, the grayscale difference can be extended to the measurement of color difference *Difference*(c_1, c_2). (c_1, c_2) is a pair of points in RGB color space. In order to define the sign of *Difference*(c_1, c_2), an ordered set of all possible discrete RGB color vectors is needed, in which the relative order of two arbitrary colors can be defined clearly and unambiguously. The ordered set of grayscale values is defined according to the natural value order. Since the RGB vector is composed of three intensities of color components, the order of such vectors can also be defined imitating the ordered grayscale set. In another word, the relative order between two colors can be based on the natural value order of the three intensities respectively. Consider the two color values:

$$c_1=(r_1, g_1, b_1) \quad c_2=(r_2, g_2, b_2)$$

where (r_1, g_1, b_1) and (r_2, g_2, b_2) are the red, green and blue components of c_1 and c_2 respectively. The determination of the order between c_1 and c_2 is defined as the following rule:

if $r_1<r_2$ then c_1 comes before c_2
else if $r_1>r_2$ then c_1 comes after c_2
else if $g_1<g_2$ then c_1 comes before c_2
else if $g_1>g_2$ then c_1 comes after c_2
else if $b_1<b_2$ then c_1 comes before c_2
else if $b_1>b_2$ then c_1 comes after c_2
else c_1 is equal to c_2

The above order is the extension of the grayscale case, in which the intensities of the red, green and blue are compared one by one with decreasing priority. If r_1 is not equal to r_2, the order can be determined by comparing r_1 and r_2. If $r_1=r_2$, g_1 and g_2 is then compared to determine the order. If $r_1=r_2$ and $g_1=g_2$, b_1 and b_2 should be compared. Based on the above rule, the relative order of c_1 and c_2 is defined and the sign of *Difference*(c_1, c_2) can be determined. If c_1 comes before c_2, the sign is '-' (negative). If c_1 comes after c_2, the sign is '+' (positive). Because the intensity of each RGB component is normally discrete and stored as 1 byte in computers, the value range of each component is [0, 255]. Therefore, an equivalent definition of the relative order for the color pair (c_1, c_2) is proposed as following:

$$Order(c_1, c_2) = \mathrm{sgn}((r_1 \cdot 65536 + g_1 \cdot 256 + b_1) - (r_2 \cdot 65536 + g_2 \cdot 256 + b_2)) \tag{5-7}$$

According to Equation (5-7), *Order*(c_1, c_2) is +1 if c_1 comes after c_2 in the ordered color set, and it is -1 if c_1 comes before c_2.

The absolute value of *Difference*(c_1, c_2) can be naturally defined as the Euclidean distance of c_1 and c_2 in the three-dimensional RGB space:

$$Euclidean(c_1, c_2) = \sqrt{(r_1 - r_2)^2 + (g_1 - g_2)^2 + (b_1 - b_2)^2} \tag{5-8}$$

Therefore, the scalar measurement of the difference for RGB color (c_1, c_2) can be defined as:

$$Difference(c_1, c_2) = Order(c_1, c_2) \cdot Euclidean(c_1, c_2) \tag{5-9}$$

In Equation (5-9), the absolute value of *Difference*(c_1, c_2) represents the degree of difference in RGB space. The sign of *Difference*(c_1, c_2) represents the relative order of the two color vector in the predefined ordered set of RGB colors.

Based on the definition of *Difference*(c_1, c_2), the relative potential field for color images can be defined as following:

$$V_R^m(x, y) = A \cdot \sum_{\substack{j=0 \\ (j \neq y \text{ or } i \neq x)}}^{H-1} \sum_{i=0}^{W-1} \frac{Difference(h(i, j), h(x, y))}{r_{(i,j)\to(x,y)}^m} \tag{5-10}$$

where $V_R^m(x, y)$ is the color relative potential on the point (x, y). $h(i,j)$ and $h(x,y)$ are the pixels' colors: $h(i,j)=(R_1, G_1, B_1)$, $h(x,y)=(R_2, G_2, B_2)$.

The color difference is as following:

$$Difference(h(i, j), h(x, y)) = Order(h(i, j), h(x, y)) \cdot Euclidean((h(i, j), h(x, y)) \tag{5-11}$$

where

$$Order(h(i, j), h(x, y)) = \mathrm{sgn}((R_1 \cdot 65536 + G_1 \cdot 256 + B_1) - (R_2 \cdot 65536 + G_2 \cdot 256 + B_2)) \tag{5-12}$$

and

$$Euclidean(h(i,j),h(x,y)) = \sqrt{(R_1 - R_2)^2 + (G_1 - G_2)^2 + (B_1 - B_2)^2} \quad (5\text{-}13)$$

The property of the color relative potential field is investigated in the following section.

5.2 The spatial property of the color relative potential field

In Equation (5-10), the relevance between two image points with distance r is represented quantitatively by the reciprocal of r^m. The value of relative potential is virtually the weighted sum of the difference between image pixel (x,y) and all other points, and the weight is the factor of relevance, i.e. the reciprocal of r^m. To investigate the properties of the color relative potential field, experiments are carried out for a series of test color images with the size of 128×128. When computing the relative potential values, the constant m in Equation (5-10) is pre-defined as m=3. The experimental results for some typical test color images are shown in Fig. 5-1 to Fig. 5-8.

Fig. 5-1(a) to Fig. 5-8(a) are the original test images. Fig. 5-1(c) to Fig. 5-8(c) show the absolute value distributions of the color relative potential for the corresponding test images, where larger gray-scale represents larger relative potential. Fig. 5-1(b) to Fig. 5-8(b) record the sign of relative potential value on each point, where white points represent positive values and black points represent negative values. The results shown in Fig. 5-1(b) to Fig. 5-8(b) indicate that the sign of the color relative potential value will reverse across the boundary of two adjacent regions, which may be exploited in the segmentation of different regions in color images.

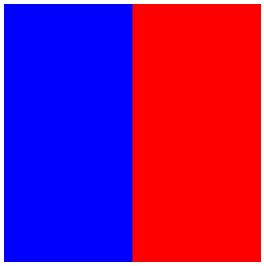

(a) Color image *test*1 of the relative potential

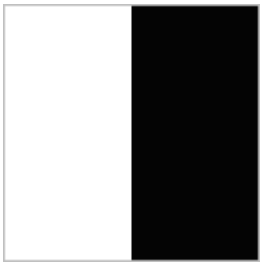

(b) The sign distribution of the relative potential

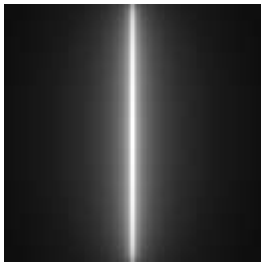

(c) The absolute value distribution

Fig. 5-1 The relative potential field of color image *test*1

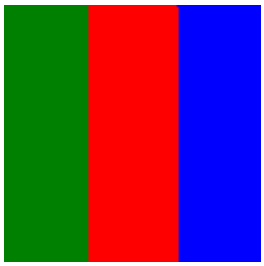

(a) Color image *test*2 of the relative potential

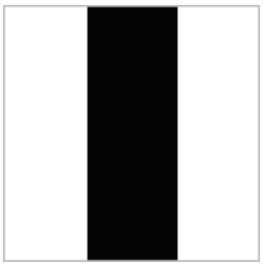

(b) The sign distribution of the relative potential

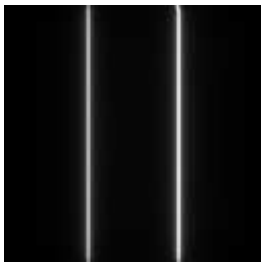

(c) The absolute value distribution

Fig. 5-2 The relative potential field of color image *test*2

(a) Color image *test*3 of the relative potential

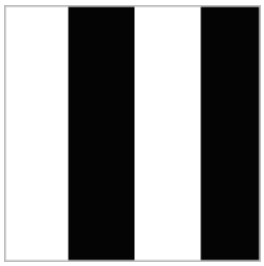

(b) The sign distribution of the relative potential

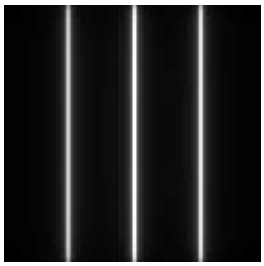

(c) The absolute value distribution

Fig. 5-3 The relative potential field of color image *test*3

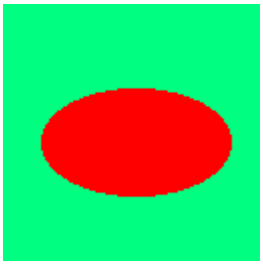

(a) Color image *test*4 of the relative potential

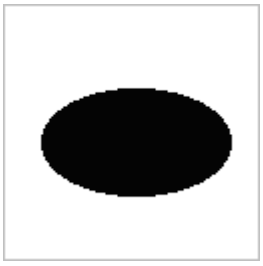

(b) The sign distribution of the relative potential

(c) The absolute value distribution

Fig. 5-4 The relative potential field of color image *test*4

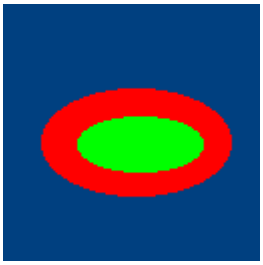

(a) Color image *test*5 of the relative potential

(b) The sign distribution of the relative potential

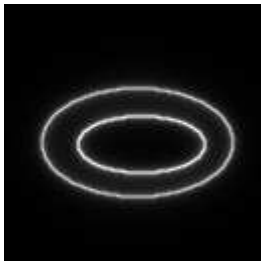

(c) The absolute value distribution

Fig. 5-5 The relative potential field of color image *test*5

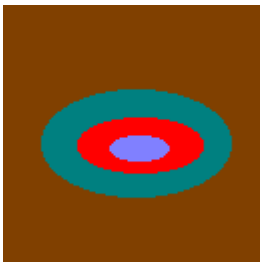

(a) Color image *test*6 of the relative potential

(b) The sign distribution of the relative potential

(c) The absolute value distribution

Fig. 5-6 The relative potential field of color image *test*6

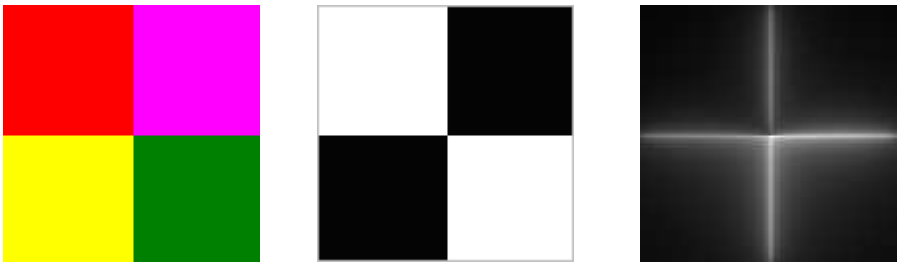

(a) Color image *test*7 of the relative potential (b) The sign distribution of the relative potential (c) The absolute value distribution

Fig. 5-7 The relative potential field of color image *test*7

(a) Color image *test*8 of the relative potential (b) The sign distribution of the relative potential (c) The absolute value distribution

Fig. 5-8 The relative potential field of color image *test*8

According to the definition of the color relative potential in Equation (5-10), the relative potential value of a pixel p is mainly affected by its local neighboring area. The local neighboring area consists of two classes of points. One class consists of the pixels in the same region of p (i.e. with similar color of p), the other consists of those in the different region. For simple test images, the color difference in the same region is zero. Thus the relative potential of p is mainly affected by the color difference between p's region and its adjacent region. Suppose $\boldsymbol{A}$ and $\boldsymbol{B}$ are two adjacent regions shown in Fig. 5-9. p_a and p_b are two border points at different border sides. p_a is in region $\boldsymbol{A}$ and p_b is in region $\boldsymbol{B}$. c_a and c_b are the colors of region $\boldsymbol{A}$ and $\boldsymbol{B}$ respectively. According to the above discussion, the sign of p_a's relative potential is determined by *Difference*(c_a, c_b), while the sign of p_b's relative potential is determined by *Difference*(c_b, c_a). It is obvious that the signs of the relative potential on p_a and p_b are opposite. This is why the sign of the relative potential will reverse across the region border. This property of the relative potential field can be exploited in image analysis.

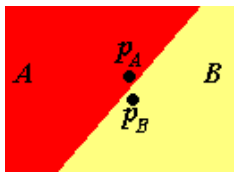

Fig. 5-9 p_a and p_b on different sides of the region border

5.3 Color image segmentation in the color relative potential field

In the experimental results of the test images, it is indicated that the signs of color relative potential are opposite in the two different adjacent regions. This can provide the basis of region segmentation in color images. Here a method of region segmentation for color images is proposed based on the color relative potential as following:

***Step*1**: Calculate the color relative potential field for the color image;

***Step*2**: Obtain the sign distribution of the color relative potential;

Step3: Group the adjacent points with the same sign of relative potential into connected regions. In the region grouping process, the adjacent pixels of the 4-connection (i.e. the upper, lower, left and right pixels) for an image point p is investigated. If any of the four adjacent pixels has the same sign of relative potential as p, it is grouped into the region which p belongs to. The obtained connected regions are the result of region segmentation for the color image.

Fig. 5-10 to Fig. 5-17 show the segmentation results based on the sign distribution of the relative potential according to Fig. 5-1(b) to Fig. 5-8(b). In the figures of segmentation results, different regions are represented by different gray-scale values. The results indicate that the region segmentation method is effective for test color images.

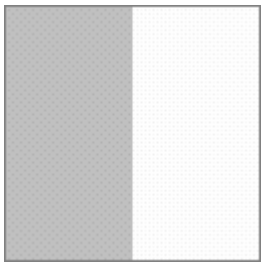

Fig. 5-10 The segmentation result for color image *test*1

Fig. 5-11 The segmentation result for color image *test*2

Fig. 5-12 The segmentation result for color image *test*3

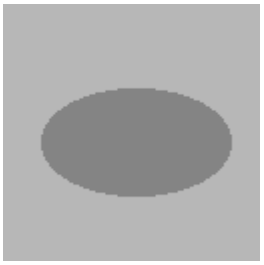

Fig. 5-13 The segmentation result for color image *test*4

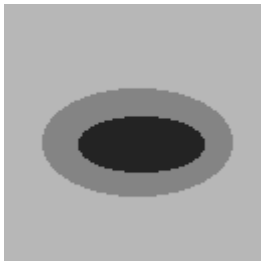

Fig. 5-14 The segmentation result for color image *test*5

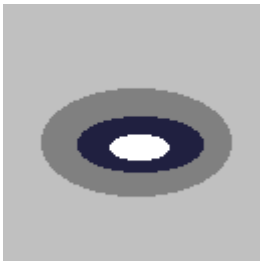

Fig. 5-15 The segmentation result for color image *test*6

Fig. 5-16 The segmentation result for color image *test*7

Fig. 5-17 The segmentation result for color image *test*8

Real world color images consist of much more complex regions than the simple test images. To investigate the effectiveness of the above method on real world images, experiments are carried out for a series of real world color images. These color images are obtained from the public image databases on the Internet. Some of the experimental results are shown from Fig. 5-18 to Fig. 5-20.

Fig. 5-18(a) shows a color image of a horse. The sign and absolute value distribution of the color relative potential are shown in Fig. 5-18(b) and Fig. 5-18(c) respectively. The segmentation result based on the sign distribution is shown in Fig. 5-18(d), where different regions are represented by different gray-scale values. In Fig. 5-18(d), the horse area can be effectively extracted. Fig. 5-18(e) shows the area of the horse extracted from the segmented result for a clearer view.

To compare the color segmentation to grayscale image segmentation with the relative potential method, experiment is also carried out for the corresponding grayscale image of the horse. Fig. 5-18(f) shows the grayscale image of the horse. Fig. 5-18(g) shows the sign distribution of the gray-scale relative potential for the grayscale image, and Fig. 5-18(h) shows the segmentation result based on the sign distribution.

(a) The original color image of the horse

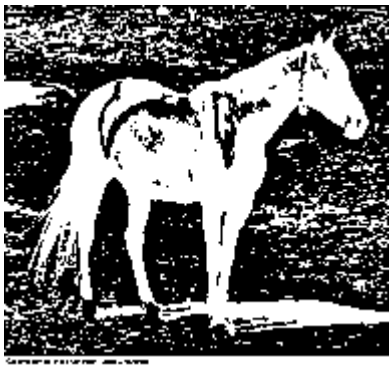

(b) The sign distribution of the relative potential field for the color image of horse

(c) The absolute value distribution of the relative potential field for the color image

(d) The segmentation result based on the sign distribution for the color image

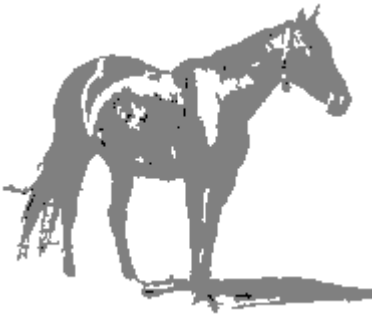

(e) The area of the horse extracted from the segmented result

(f) The corresponding grayscale image of the horse

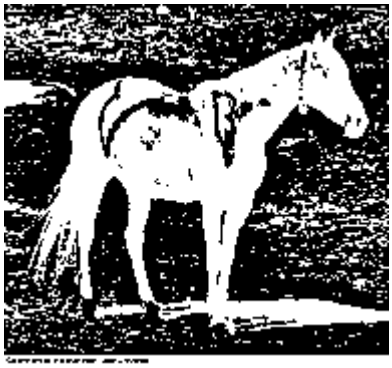

(g) The sign distribution of the relative potential field for the grayscale image

(h) The segmentation result based on the sign distribution for the grayscale image

Fig. 5-18 The experimental results for the horse image

In Fig 18(d) and Fig. 5-18(h), the segmentation of the horse area for color and grayscale image are both effective. Moreover, the two results are similar perhaps because the colors in Fig 18(a) are not rich.

Fig. 5-19(a) shows a color image of a house. The sign and absolute value distribution of the color relative potential are shown in Fig. 5-19(b) and Fig. 5-19(c) respectively. The segmentation result based on the sign distribution is shown in Fig. 5-19(d), where the main parts of the house can be effectively extracted and separated.

To compare the color segmentation to grayscale image segmentation with the relative potential method, experiment is also carried out for the corresponding grayscale image of the house. Fig. 5-19(e) shows the grayscale image of the house. Fig. 5-19(f) shows the sign distribution of the gray-scale relative potential for the grayscale image, and Fig. 5-19(g) shows the segmentation result based on the sign distribution.

(a) The original color image of the house

(b) The sign distribution of the relative potential field for the color image

(c) The absolute value distribution of the relative potential field for the color image

(d) The segmentation result based on the sign distribution for the color image

(e) The corresponding grayscale image of the house

(f) The sign distribution of the relative potential field for the grayscale image

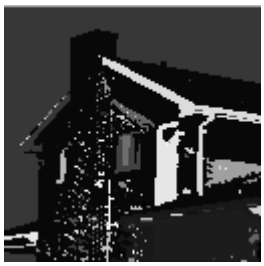

(g) The segmentation result based on the sign distribution for the grayscale image

Fig. 5-19 The experimental results for the house image

For the house image, the advantage of color segmentation is indicated by the comparison to grayscale segmentation. It is clear that the color segmentation gets better result than the grayscale segmentation for the house image by comparing Fig. 5-19(d) to Fig. 5-19(g). For example, the chimney, roof and eaves are separated clearly in Fig. 5-19(d). But in Fig. 5-19(g) the chimney, roof and eaves are connected into one region.

Fig. 5-20(a) shows the color image of a butterfly. The sign and absolute value distribution of the color relative potential are shown in Fig. 5-20 (b) and Fig. 5-20 (c) respectively. The segmentation result based on the sign distribution is shown in Fig. 5-20 (d), where the butterfly area can be effectively extracted. Fig. 5-20 (e) shows the area of the butterfly extracted from the segmented result for a clearer view.

To compare the color segmentation to grayscale image segmentation with the relative potential method, experiment is also carried out for the corresponding grayscale image of the butterfly. Fig. 5-20 (f) shows the grayscale image of the butterfly. Fig. 5-20 (g) shows the sign distribution of the grayscale relative potential for the grayscale image, and Fig. 5-20 (h) shows the segmentation result based on the sign distribution.

(a) The original color image of the butterfly

(b) The sign distribution of the relative potential field for the color image

(c) The absolute value distribution of the relative potential field for the color image

(d) The segmentation result based on the sign distribution for the color image

(e) The area of the butterfly extracted from the segmented result

(f) The corresponding grayscale image of the butterfly

(g) The sign distribution of the relative potential field for the grayscale image

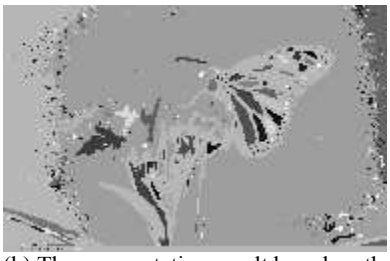

(h) The segmentation result based on the sign distribution for the grayscale image

Fig. 5-20 The experimental results for the butterfly image

The advantage of color image segmentation is also indicated by the comparison of Fig. 5-20(d) and Fig. 5-20(h). In Fig. 5-20(d), the area of the butterfly can be clearly separated from other objects, which is clearly shown in Fig. 5-20(e). However, in Fig. 5-20(h) the butterfly area is combined to the flower area. It is indicated that since color carries more information than grayscale, the processing of the color image may obtain more satisfactory results if proper method is used.

5.4 The preprocessing of brightness normalization

Color is one of the most important optical features of an object's surface. However, curved parts on the surface are common, and the change of normal direction at different surface points may cause the change of reflection characteristics. Therefore, it is common that the surface of an object has several parts of the same chrominance but different brightness. Moreover, part of a surface may also be in the shadow of other objects. In another word, shading is also commonly seen in color images. In such cases, the surface of a single object may be segmented into several sub-regions, which is not preferred when the integrity of the segmented objects is of much importance.

In this chapter, a brightness normalization method is proposed to eliminate the influence of shading or surface curvature in color image segmentation. In the proposed method, the brightness of each pixel is normalized to the same value before the calculation of the color relative potential. Therefore, only the chrominance is considered in the measurement of color difference when calculating the color relative potential. Here the normalized value of brightness is set to 255. For the pixel with the color (r_1, g_1, b_1), the brightness normalization result (r_N, g_N, b_N) is given as following:

$$\begin{aligned} r_N &= r_1 \cdot 255 / h_1 \\ g_N &= g_1 \cdot 255 / h_1 \\ b_N &= b_1 \cdot 255 / h_1 \end{aligned} \tag{5-14}$$

where h_1 is the original brightness of (r_1, g_1, b_1) according to the well known relationship between the RGB color and the brightness:

$$h_1 = 0.299 \cdot r_1 + 0.587 \cdot g_1 + 0.114 \cdot b_1 \tag{5-15}$$

Then the brightness after normalization is:

$$\begin{aligned} h_N &= 0.299 \cdot r_N + 0.587 \cdot g_N + 0.114 \cdot b_N \\ &= 0.299 \cdot (r_1 \cdot 255 / h_1) + 0.587 \cdot (g_1 \cdot 255 / h_1) + 0.114 \cdot (b_1 \cdot 255 / h_1) \\ &= (0.299 \cdot r_1 + 0.587 \cdot g_1 + 0.114 \cdot b_1) / h_1 \cdot 255 \\ &= 255 \end{aligned}$$

Thus the brightness of each pixel is normalized to 255. All the pixels are processed according to Equation (5-14) before the calculation of the color relative potential. Experiments are carried out to investigate the effectiveness of the brightness normalization on color image segmentation. The color relative potential is calculated for the normalized color image, and then the segmentation based on the sign distribution is implemented. Experiments are carried out on a series of color images, which are obtained from the public image databases on the Internet. Some of the experimental results are shown from Fig. 5-21 to Fig. 5-24.

Fig. 5-21(a) is the color image of a Border Collie dog. The result of brightness normalization is shown in Fig. 5-21(b), where all the pixels have the same brightness. Fig. 5-21(c) shows the sign distribution of the color relative potential for the brightness normalized image. The segmentation result based on the sign distribution is shown in Fig. 5-21(d), where the dog area can be effectively extracted. Fig. 5-21(e) shows the dog area extracted from Fig. 5-21(d) for a clearer view. Because the main parts of the dog area is in grayscale and some areas of the grass are also in grayscale, in Fig. 5-21(e) the dog area is attached with a small part of the grass area.

In order to compare the segmentation results with and without brightness normalization, experiments are also carried out for color images without brightness normalization, and also for the grayscale image. Fig. 5-21(f) shows the sign distribution of the color relative potential for the original color image without brightness normalization, and Fig. 5-21(g) shows the corresponding segmentation

result. The grayscale image is shown in Fig. 5-21(h), and the corresponding sign distribution of the gray-scale relative potential is shown in Fig. 5-21(i). The segmentation result for the grayscale image is shown in Fig. 5-21(j). The comparison of Fig. 5-21(d), (g) and (j) indicates that the brightness normalization achieves more satisfactory results.

(a) The original color image of a Border Collie dog

(b) The brightness normalized image

(c) The sign distribution of the relative potential field for the brightness normalized image

(d) The segmentation result based on the sign distribution for the brightness normalized image

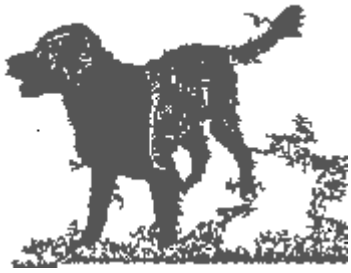

(e) The area of the dog extracted from the segmented result

(f) The sign distribution of the relative potential field for the original color image

(g) The segmentation result based on the sign distribution for the original color image

(h) The corresponding grayscale image of the Border Collie dog

(i) The sign distribution of the relative potential field for the grayscale image

(j) The segmentation result based on the sign distribution for the grayscale image

Fig. 5-21 The experimental results of brightness normalization for the image of Border Collie dog

Fig. 5-22(a) is the color image of the flower. The result of brightness normalization is shown in Fig. 5-22(b), where all the pixels have the same brightness. Fig. 5-22(c) shows the sign distribution of the color relative potential for the brightness normalized image. The segmentation result based on the sign distribution is shown in Fig. 5-22(d), where the flower area can be effectively extracted. Fig. 5-22(e) shows the flower area extracted from Fig. 5-22(d) for a clearer view.

In order to compare the segmentation results with and without brightness normalization, experiments are also carried out for color image without brightness normalization, and also for the grayscale image. Fig. 5-22(f) shows the sign distribution of the color relative potential for the original color image without brightness normalization, and Fig. 5-22(g) shows the corresponding segmentation result. The grayscale image is shown in Fig. 5-22(h), and the corresponding sign distribution of the gray-scale relative potential is shown in Fig. 5-22(i). The segmentation result for the grayscale image is shown in Fig. 5-22(j). The comparison of Fig. 5-22(d), (g) and (j) indicates that the brightness normalization achieves more satisfactory results.

(a) The original color image of the flower

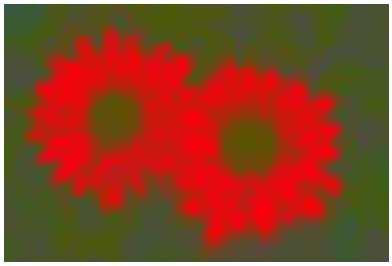

(b) The brightness normalized image

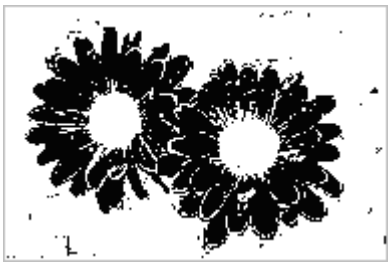

(c) The sign distribution of the relative potential field for the brightness normalized image

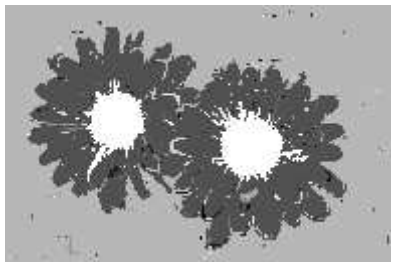

(d) The segmentation result based on the sign distribution for the brightness normalized image

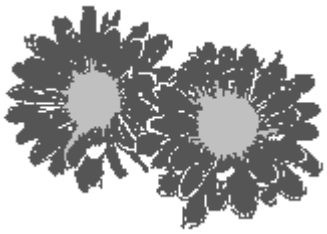

(e) The area of the flower extracted from the segmented result

(f) The sign distribution of the relative potential field for the original color image

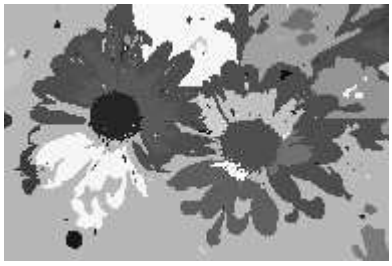

(g) The segmentation result based on the sign distribution for the original color image

(h) The corresponding grayscale image of the flower

(i) The sign distribution of the relative potential field for the grayscale image

(j) The segmentation result based on the sign distribution for the grayscale image

Fig. 5-22 The experimental results of brightness normalization for the flower image

Fig. 5-23(a) is the color image of the peppers. The result of brightness normalization is shown in Fig. 5-23(b), where all the pixels have the same brightness. Fig. 5-23(c) shows the sign distribution of the color relative potential for the brightness normalized image. The segmentation result based on the

sign distribution is shown in Fig. 5-23(d), where the areas of different peppers can be effectively extracted and properly separated.

In order to compare the segmentation results with and without brightness normalization, experiments are also carried out for color image without brightness normalization, and also for the grayscale image. Fig. 5-23(e) shows the sign distribution of the color relative potential for the original color image without brightness normalization, and Fig. 5-23(f) shows the corresponding segmentation result. The grayscale image is shown in Fig. 5-23(g), and the corresponding sign distribution of the gray-scale relative potential is shown in Fig. 5-23(h). The segmentation result for the grayscale image is shown in Fig. 5-23(i). The comparison of Fig. 5-23(d), (f) and (i) indicates that the brightness normalization achieves more satisfactory results.

(a) The original color image of the peppers

(b) The brightness normalized image

(c) The sign distribution of the relative potential field for the brightness normalized image

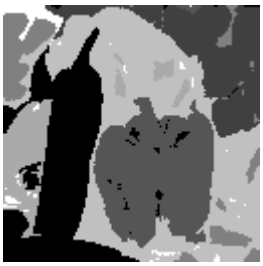

(d) The segmentation result based on the sign distribution for the brightness normalized image

(e) The sign distribution of the relative potential field for the original color image

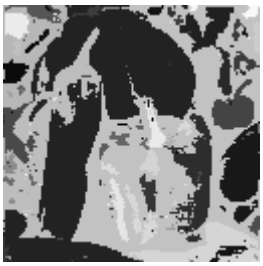

(f) The segmentation result based on the sign distribution for the original color image

(g) The corresponding grayscale image of the peppers

(h) The sign distribution of the relative potential field for the grayscale image

(i) The segmentation result based on the sign distribution for the grayscale image

Fig. 5-23 The experimental results of brightness normalization for the peppers image

Fig. 5-24(a) is the color image of a dog and the grass. The result of brightness normalization is shown in Fig. 5-24(b), where all the pixels have the same brightness. Fig. 5-24(c) shows the sign distribution of the color relative potential for the brightness normalized image. The segmentation result based on the sign distribution is shown in Fig. 5-24(d), where the dog area can be effectively extracted. Fig. 5-24(e) shows the dog area extracted from Fig. 5-24(d) for a clearer view. Because some part of the grass area has similar chrominance to that of the dog area, the extracted dog area is attached with a small part of the grass area in Fig. 5-24(e).

In order to compare the segmentation results with and without brightness normalization, experiments are also carried out for color image without brightness normalization, and also for the grayscale image. Fig. 5-24(f) shows the sign distribution of the color relative potential for the original color image without brightness normalization, and Fig. 5-24(g) shows the corresponding segmentation result. The dog area extracted from Fig. 5-24(g) is shown in Fig. 5-24(h). Compared with Fig. 5-24(e), the brightness normalization can produce more complete segmentation result of the dog area.

The grayscale image is shown in Fig. 5-24(i), and the corresponding sign distribution of the grayscale relative potential is shown in Fig. 5-24(j). The segmentation result for the grayscale image is shown in Fig. 5-24(k). The comparison of Fig. 5-24(d), (g) and (k) indicates that the brightness normalization achieves more complete segmentation results.

(a) The original color image of a dog and the grass

(b) The brightness normalized image

(c) The sign distribution of the relative potential field for the brightness normalized image

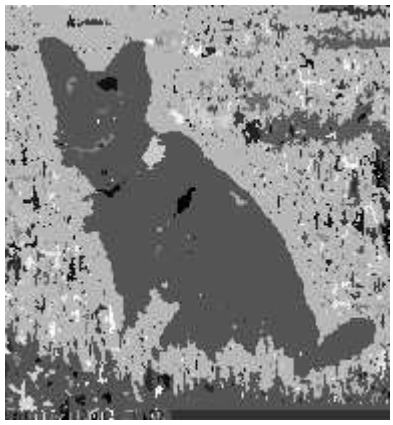

(d) The segmentation result based on the sign distribution for the brightness normalized image

(e) The area of the dog extracted from the segmented result

(f) The sign distribution of the relative potential field for the original color image

(g) The segmentation result based on the sign distribution for the original image

(h) The area of the dog extracted from the segmented result for the original image

(i) The corresponding grayscale image of a dog and the grass

(j) The sign distribution of the relative potential field for the grayscale image

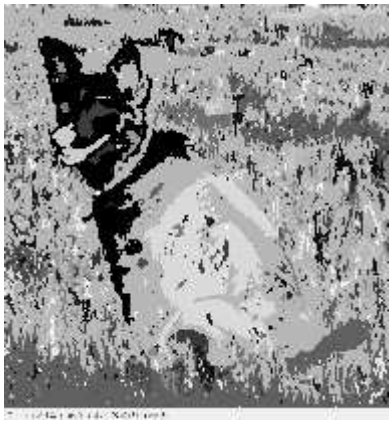

(k) The segmentation result based on the sign distribution for the grayscale image

Fig. 5-24 The experimental results of brightness normalization for the image of a dog and the grass

The brightness normalization is suitable for such color images where the surfaces of different adjacent objects have different chrominance, which is a common case in color images. But the brightness normalization also has limitation. For those image areas where different adjacent objects have familiar chrominance but different brightness (such as the images with lots of grayscale area), the brightness normalization method may mistake two adjacent regions of different objects into one area in segmentation. Therefore, it is indicated that there should be a proper balance between the consideration of brightness and chrominance in color image segmentation, which will be investigated in future research.

The work in this chapter indicates that the “relative field” method can be effectively extended to color image processing. The richer information in color images may bring more satisfactory processing results than grayscale images. In this chapter, the RGB color model is used to representing color information. Because there are other color models which have their own advantages respectively, further work will study the possible improvements of the processing results by using other kind of color model.

6 Summary and Discussion

Physics-inspired image processing is a promising and interesting research area. The work described in this book is part of the authors' on-going research work. It is obvious that there is much possibility for the improvement and extension of the methods, and also the creation of new and better algorithms. In this chapter, some interesting topics about the methods presented in the book are discussed.

6.1 The transformation among different patterns (the diffusing, whirling, and shrinking patterns) of vector field

In this book, several image analysis methods inspired by electro-magnetism are presented. Effective image segmentation can be implemented based on these methods. These methods are of different types according to their operating principles. The relative potential field is a scalar field method, in which image region division can be performed according to the change of relative potential's sign. The edge vector method generates a vector field which is at right angles to the image plane, and region division can be performed according to the change of vector direction (i.e. coming out of or into the image plane).

On the other hand, the diffusing vector field, curling vector field and compressing vector field are of the same category, in which the region division is performed by area growing in the 2D vector field on the image plane. Moreover, the above three vector fields are all belong to the "relative field". Therefore, it is interesting to study the similarity and relation of the three forms (the diffusing, whirling, and shrinking forms) of 2D vector field.

Experiments have been carried out for test images to get their diffusing vector field and then transform the field pattern. It is interesting to find that the rotation of the vectors can implement the transformation among the three patterns of the 2D vector field. In another word, a vector field of diffusing pattern (in which the vectors diffuse outwards in each homogeneous region) can be transformed to a compressing pattern (in which the vectors shrink inwards in each homogeneous region) by reversing the direction of each vector. Moreover, a vector field of diffusing pattern can also be turned into a whirling pattern (in which the vectors form a whirl in each homogeneous region) by rotating each vector 90 degrees clockwise. The experimental results for some test images are shown in Fig. 6-1 to Fig. 6-3. The vector directions in these results are discretized into eight directions.

Fig. 6-1(a) shows a whole homogeneous region. Fig. 6-1(b) shows its diffusing vector field in which the vectors form a pattern of expanding. Fig. 6-1(c) shows the result of rotating each vector in Fig. 6-1(b) 90 degrees clockwise. Fig. 6-1(c) has a pattern of whirling. Fig. 6-1(d) is the result of reversing each vector in Fig. 6-1(b). Fig. 6-1(d) has a pattern of shrinking.

(a) the image *test1* (the original image, and 4 times of original size on the right)

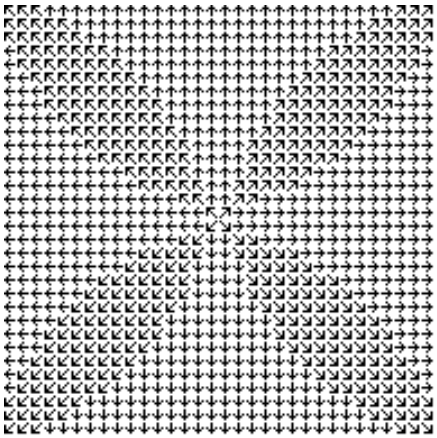

(b) the direction of each vector in the diffusing vector field of *test1*

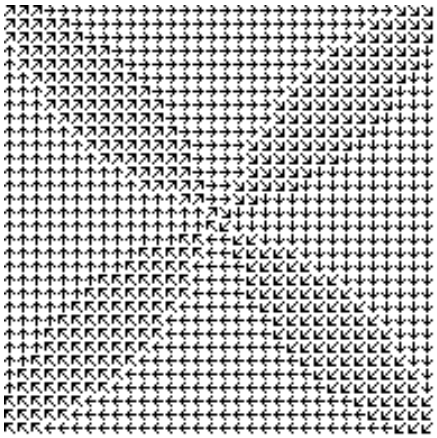

(c) the field of whirling vectors by rotating each vector in (b) 90 degrees clockwise

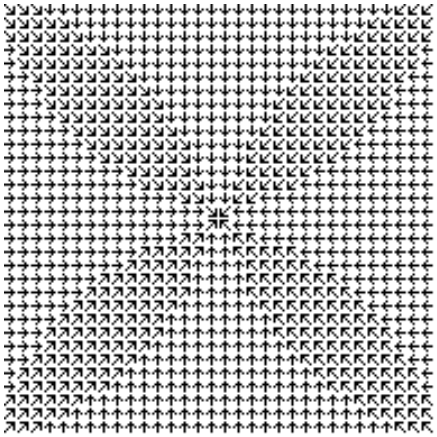

(d) the field of shrinking vectors by reversing the direction of each vector in (b)

Fig. 6-1 The diffusing vector field of image *test1*, and the corresponding whirling and shrinking patterns obtained by vector rotation

Fig. 6-2(a) has a region of ellipse. Fig. 6-2(b) shows its diffusing vector field. In Fig. 6-2(b), the vectors in the ellipse region form a pattern of expanding, which is highlighted by the dark area. Fig. 6-2(c) shows the result of rotating each vector in Fig. 6-2(b) 90 degrees clockwise. In Fig. 6-2(c), the vectors in the ellipse region form a pattern of whirling. Fig. 6-2(d) shows the result of reversing each vector in Fig. 6-2(b). In Fig. 6-2(d), the vectors in the ellipse region form a pattern of shrinking.

(a) the image *test2* (the original image, and 4 times of original size on the right)

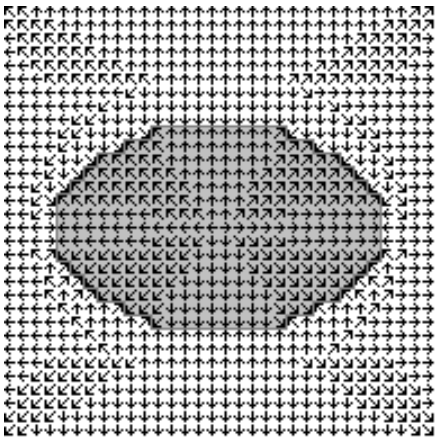

(b) the direction of each vector in the diffusing vector field of *test2*

(c)

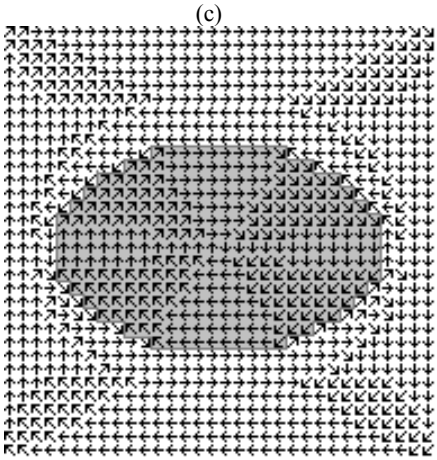

(c) the field of whirling vectors by rotating each vector in (b) 90 degrees clockwise

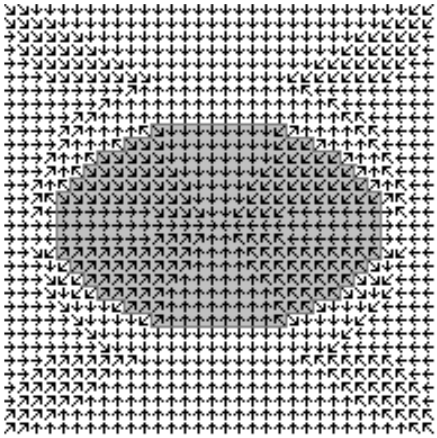

(d) the field of shrinking vectors by reversing the direction of each vector in (b)

Fig. 6-2 The diffusing vector field of image *test2*, and the corresponding whirling and shrinking patterns obtained by vector rotation

Fig. 6-3(a) has two regions of an ellipse and a rectangle. Fig. 6-3(b) shows its diffusing vector field. In Fig. 6-3(b), the vectors in the ellipse and rectangle regions form a pattern of expanding respectively, which is highlighted by the two dark areas. Fig. 6-3(c) shows the result of rotating each vector in Fig. 6-3(b) 90 degrees clockwise. In Fig. 6-3(c), the vectors in the ellipse and rectangle regions form a pattern of whirling. Fig. 6-3(d) shows the result of reversing each vector in Fig. 6-3(b). In Fig. 6-3(d), the vectors in the ellipse and rectangle regions form a pattern of shrinking.

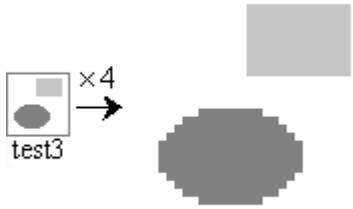

(a) the image *test3* (the original image, and 4 times of original size on the right)

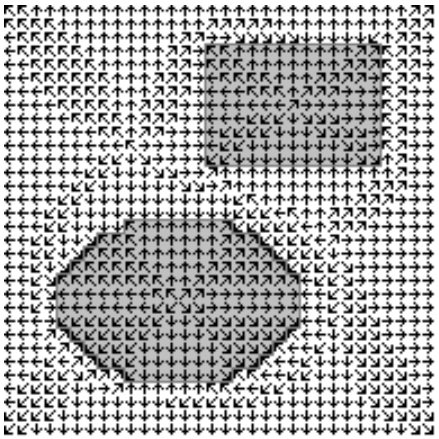

(b) the direction of each vector in the diffusing vector field of *test3*

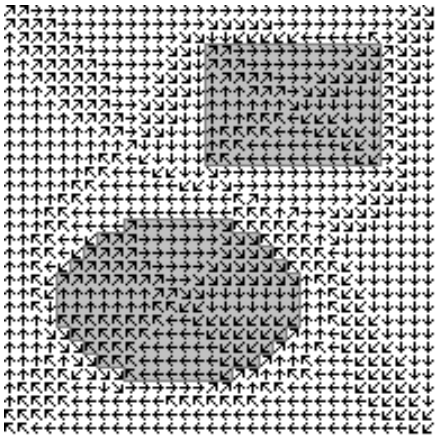

(c) the field of whirling vectors by rotating each vector in (b) 90 degrees clockwise

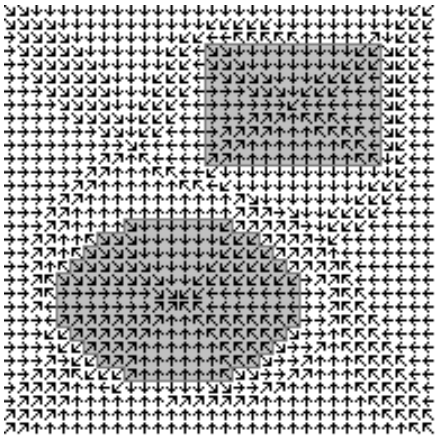

(d) the field of shrinking vectors by reversing the direction of each vector in (b)

Fig. 6-3 The diffusing vector field of image *test3*, and the corresponding whirling and shrinking patterns obtained by vector rotation

According to the above results, the three patterns of the vector "relative field" can be transformed to one another. It is indicated that there is close relationship between the three 2D vector field methods in this book. Further work may study their detailed relationship for a better understanding of the "relative field".

6.2 The Source-reverse Transform and the Laplacian Operator

It is interesting that some of the methods in the book have underlying relationship with other existing concepts and methods. The relationship between the source-reverse transform and the Laplacian operator is one example. In Chapter 2, a source-reverse transform is presented, in which the virtual field source $F(x,y)$ is estimated according to Equation (2-25). Here the definition of the source reversing is re-written for a convenient view and discussion:

$$F(x,y) = -div(grad\ (f(x,y))) \tag{6-1}$$

The gradient of the image $f(x,y)$ is given as:

$$\vec{G} = grad\ (f(x,y)) = \frac{\partial f(x,y)}{\partial x}\vec{i} + \frac{\partial f(x,y)}{\partial y}\vec{j} \tag{6-2}$$

Then the divergence of the image's gradient is given as:

$$div\,\vec{G} = \frac{\partial G_x}{\partial x} + \frac{\partial G_y}{\partial y} \tag{6-3}$$

The two components of the gradient vector are:

$$G_x = \frac{\partial f(x,y)}{\partial x} \quad G_y = \frac{\partial f(x,y)}{\partial y} \tag{6-4}$$

Therefore, in mathematics the virtual source $F(x,y)$ is given as:

$$F(x,y) = div\,\vec{G} = \frac{\partial^2 f(x,y)}{\partial x^2} + \frac{\partial^2 f(x,y)}{\partial y^2} \tag{6-5}$$

In mathematics, the operation like Equation (6-5) is virtually defined as the Laplacian operator[104-107]:

$$\Delta = \left(\frac{\partial^2}{\partial x^2} + \frac{\partial^2}{\partial y^2} \right) \tag{6-6}$$

$$\Delta f = \left(\frac{\partial^2}{\partial x^2} + \frac{\partial^2}{\partial y^2} \right) f = \frac{\partial^2 f}{\partial x^2} + \frac{\partial^2 f}{\partial y^2} \tag{6-7}$$

The Laplacian operator has been used in image edge detection[104-107]. According to Equation (6-5) and (6-7), the Laplacian operator on images has a similar effect of the source-reverse transform studied in Chapter 2. With the Laplacian operator, the edge points can be located by detecting the zero-crossing points after applying the operator on the image. Similarly, in Chapter 2 it is indicated by experiments that the region borders can be detected by the sign reverse of the source values (equivalent to zero-crossing in the Laplacian operator method) in the virtual source. It is quite interesting that the Laplacian operator has a physical analogy of source reverse.

The relationship between the virtual curl source and the image gradient is another interesting case. It is proved in Chapter 3 that the virtual curl source and the image gradient field are orthogonal. In another word, the virtual curl source can be obtained by rotating each gradient vector 90 degrees (all clockwise or all anti-clockwise). Moreover, the original image can be estimated by an opposite transform form the virtual curl source to the image. Therefore, the curl source transform provide a way of approximating the image from its gradient field with a magneto-static analogy. In the field of physics-inspired methodology for image processing, there are still plenty of unexplored research topics which are both interesting and of great value in practical use.

6.3 Summary

As a new branch of image transform method, the electro-magnetism inspired transforms has some unique characteristics compared with mathematical transforms such as Fourier transform, discrete cosine transform, etc. The virtual filed obtained by the transform is still defined in the same 2D or 3D space as the image. This is because the physical field itself is a kind of spatial distribution, and the field and the source both exist in the same physical space. In another word, the field inspired transforms convert the image in the 2D or 3D space into another form of representation in the same space. Therefore, the spatial properties of the transformed fields may have direct relationship with the image structure, and it is convenient to obtain some spatial features of the image directly in the transformed virtual field.

The electro-magnetic fields (both scalar and vector field) have some common characteristics in their definition. Considering the electro-static potential, the electro-static force, and the magneto-static induction field in a continuous spatial area, all of them have a form of integral in their definitions. For a space point *p*, the field value on *p* is defined by an integral, which accumulates the effects of all the source points on *p*. Moreover, the integrands in their definitions have a common factor of **1/*r*** (i.e. the reciprocal of the distance *r* between the source point and the field point). Therefore, the source points near *p* have obviously larger effects on the field value of *p*, and the effect of source point on *p* decreases quickly with the increasing of the distance *r*. Generally speaking, in images neighbouring points have stronger relevance than remote points. Therefore, the mathematical form of the electro-magnetic fields (the common factor of **1/*r*** in their definitions) can be a good representation of the above local-global relevance characteristic in images. In many image processing tasks, it is usually

necessary to consider the balance between the strong local relevance of close neighbouring points and a wide range of weaker relevance of remote points. The electro-magnetism inspired transforms are quite suitable for such requirement of image analysis.

In the book, several forms of virtual field transforms for images are presented and studied, which are inspired by electro-static field or magneto-static field respectively. Some are of scalar field transform, and others are of vector field transform. In these transforms, the basic forms of the physical fields are imitated (i.e. the definition in integral form and the common factor of $\mathbf{1}/r$). Moreover, the original definitions of the physical fields are extended to a flexible and generalized form in some methods presented in this book for adaptability and expansibility. For image segmentation task, the relative potential field, diffusing vector field, compressing vector field and curling vector field are all defined in a form of "relative field", in which the measurement of pixel difference is introduced into the virtual field definitions. In the future work, for various processing tasks, other kind of virtual fields besides the "relative field" will be studied. For example, other kind of virtual fields may be defined by giving different definition of function f in Equation (2-4) and (2-8). Further work will investigate more detailed properties of virtual field transforms inspired by electro-magnetic fields. The possible application of the methods to other practical processing tasks will also be investigated. Moreover, the methods presented in the book concentrate on the static electro-magnetic fields. The principles of time-variant field will be investigated in future work, and the possible application of the electro-magnetic interaction in physics-inspired methods will also be studied.

Reference

[1] Mark S. Nixon, Xin U. Liu, Cem Direkoglu, David J. Hurley, On using physical analogies for feature and shape extraction in computer vision, *Computer Journal*, Vol. 54, No. 1, 2011, pp. 11-25.

[2] D.J. Hurley, M.S. Nixon, J.N. Carter, A new force field transform for ear and face recognition, *IEEE International Conference on Image Processing*, Vol. 1, 2000, pp. 25-28.

[3] David J. Hurley, Mark S. Nixon, John N. Carter, Force field feature extraction for ear biometrics, *Computer Vision and Image Understanding*, Vol. 98, No. 3, 2005, pp. 491-512.

[4] David J. Hurley, Mark S. Nixon, John N. Carter, Force field energy functionals for image feature extraction, *Image and Vision Computing*, Vol. 20, No. 5-6, 2002, pp. 311-317

[5] Xin U Liu, Mark S Nixon, Water Flow Based Complex Feature Extraction. *Advanced Concepts for Intelligent Vision Systems*, Lecture Notes in Computer Science, 2006. pp. 833-845.

[6] Xin U Liu, Mark S Nixon, Medical Image Segmentation by Water Flow, in *Proceedings of Medical Image Understanding and Analysis*, MIUA 2007.

[7] Xin U Liu, Mark S Nixon, Water flow based vessel detection in retinal images, *Proceedings of IET International Conference on Visual Information Engineering* 2006, 2006, pp. 345-350.

[8] Xin U Liu, Mark S Nixon, Image and volume segmentation by water flow, *Third International Symposium on Proceedings of Advances in Visual Computing*, ISVC 2007, 2007, pp. 62-74.

[9] Alastair H. Cummings, On Using Water to Guide Image Feature Extraction, Technical Report, School of Electronics and Computer Science, the University of Southampton, United Kingdom

[10] Cem Direkoglu, FEATURE EXTRACTION VIA HEAT FLOW ANALOGY, a thesis submitted for the degree of Doctor of Philosophy, School of Electronics and Computer Science, University of Southampton, United Kingdom, 2009.

[11] Cem Direkoglu, Mark S. Nixon, Shape extraction via heat flow analogy, *Proceedings of 9th International Conference on Advanced Concepts for Intelligent Vision Systems*, ACIVS 2007, pp. 553-564.

[12] Cem Direkoglu, Mark S. Nixon, On using an analogy to heat flow for shape extraction, a book chapter in *Pattern Analysis & Applications*, Springer 2011.

[13] Cem Direkoglu and Mark S. Nixon, Moving-edge detection via heat flow analogy, *Pattern Recognition Letters*, Vol. 32, No. 2, 2011, pp. 270-279.

[14] Alastair H. Cummings, Mark S. Nixon, John N. Carter, A novel ray analogy for enrolment of ear biometrics, *IEEE 4th International Conference on Biometrics: Theory, Applications and Systems*, BTAS 2010, 2010, pp. 1-16.

[15] Alastair H. Cummings, Mark S. Nixon, John N. Carter, Circle detection using the image ray transform: A novel technique for using a ray analogy to extract circular features, *Proceedings of the International Conference on Computer Vision Theory and Applications*, Vol. 2, 2010, pp. 23-32.

[16] Andrei C. Jalba, Michael H.F. Wilkinson, Jos B.T.M. Roerdink, CPM: A deformable model for shape recovery and segmentation based on charged particles, *IEEE Transactions on Pattern Analysis and Machine Intelligence*, Vol. 26, No. 10, 2004, pp. 1320-1335.

[17] Kenong Wu and Martin D. Levine, 3D part segmentation using simulated electrical charge distributions, *IEEE Transactions on Pattern Analysis and Machine Intelligence*, Vol. 19, No. 11, 1997, pp. 1223-1235.

[18] Andrei C. Jalba, Jos B. T. M. Roerdink, Efficient surface reconstruction using generalized Coulomb potentials, *IEEE Transactions on Visualization and Computer Graphics*, Vol. 13, No. 6, 2007, pp. 1512-1519.

[19] N. Ahuja and J. Chuang, Shape representation using a generalized potential field model, *IEEE Transactions on Pattern Analysis and Machine Intelligence*, Vol. 19, No. 2, 1997, pp. 169-176.

[20] Chi-Hao Tsai, Min-Chi Ko, Skeletonization of Three-Dimensional Object Using Generalized Potential Field, *IEEE Transactions on Pattern Analysis and Machine Intelligence*, Vol. 22 No. 11, 2000, pp. 1241-1251.

[21] Qing Liu, Jian Zhuang, Sun'an Wang, Algorithm for image resolution enhancement based on static electric field theory, *Journal of Xi'an Jiaotong University*, Vol. 40, No. 11, 2006, pp. 1300-1304.

[22] Bin Luo, A.D.J. Cross, E.R. Hancock, Corner detection via topographic analysis of vector-potential, *Pattern Recognition Letters*, Vol. 20, No. 6, 1999, pp. 635-650.

[23] B. Kimia Benjamin and Siddiqi Kaleem, Geometric Heat Equation and Nonlinear Diffusion of Shapes and Images, *Computer Vision and Image Understanding*, Vol. 64, No. 3, 1996, pp. 305–322.

[24] Xinhua Ji, Jufu Feng, A new approach to thinning based on time-reversed heat conduction model, *Proceedings of International Conference on Image Processing*, Vol. 1, 2004, pp. 653-656.

[25] Siddharth Manay, Anthony Yezzi, Anti-geometric diffusion for adaptive thresholding and fast segmentation, *IEEE Transactions on Image Processing*, Vol. 12, No. 11, 2003, pp. 1310-1323.

[26] H. Blum, Biological shape and visual science. I., *Journal of Theoretical Biology*, Vol. 38, No. 2, 1973, pp. 205-287.
[27] Chwen-Jye Sze, Hong-Yuan Mark Liao, Kuo-Chin Fan, A New Image Flux Conduction Model and Its Application to Selective Image Smoothing, *IEEE Transactions on Image Processing*, Vol. 10, No. 2, 2001, pp. 296-306.
[28] M. Bertalmío, A.L. Bertozzi, G. Sapiro, Navier-Stokes, fluid dynamics, and image and video inpainting, *Proceedings of the IEEE Computer Society Conference on Computer Vision and Pattern Recognition*, Vol. 1, 2001, pp. I355-I362.
[29] Yi Zhao, Nonrigid Image Registration Using Physically Based Models, a master thesis presented to the University of Waterloo , Waterloo, Ontario, Canada, 2006.
[30] Xiang Sean Zhou, Yong Rui, Thomas S. Huang, Water-filling: A novel way for image structural feature extraction, *IEEE International Conference on Image Processing*, Vol. 2, 1999, pp. 570-574.
[31] H. Digabel and C. Lantuejoul, Iterative algorithms, Proceedings of 2nd European Symposium on Quantitative Analysis of Microstructures in Material Science, Biology and Medicine, 1977, pp. 85-99.
[32] S. Beucher and C. Lantuejoul, Use of watersheds in contour detection, *International workshop on image processing: real-time edge and motion detection/estimation*, France, 1979.
[33] L. Vincent and P. Soille, Watershed in digital spaces: an efficient algorithm based on immersion simulation, *IEEE Transactions on Pattern Analysis and Machine Intelligence*, Vol. 13, No. 6, 1991, pp. 583-598.
[34] D. R. Chialvo and M. M. Millonas, How swarms build cognitive maps, *The Biology and Technology of Intelligent Autonomous Agents*, No. 144, 1995, pp. 439-450.
[35] Vitorino Ramos and Filipe Almeida, Artificial Ant Colonies in Digital Image Habitats - A Mass Behaviour Effect Study on Pattern Recognition, *Proceedings of ANTS'2000 - 2nd International Workshop on Ant Algorithms* (*From Ant Colonies to Artificial Ants*), 2000, pp. 113-116.
[36] Xiaodong Zhuang and N. E. Mastorakis, Image processing with the artificial swarm intelligence, *WSEAS Transactions on Computers*, Vol.4, Issue 4, 2005, pp. 333-341.
[37] S. Ali Etemad, Tony White, An ant-inspired algorithm for detection of image edge features, *Applied Soft Computing Journal*, Vol. 11, No. 8, 2011, pp. 4883-4893.
[38] Peng Huang, Huizhi Cao, Shuqian Luo, An artificial ant colonies approach to medical image segmentation, *Computer Methods and Programs in Biomedicine*, Vol. 92, No. 3, 2008, pp. 267-273.
[39] Piergiorgio Cerello, Sorin Christian Cheran, Stefano Bagnasco, et al, 3-D object segmentation using ant colonies, *Pattern Recognition*, Vol. 43, No. 4, 2010, pp. 1476-1490.
[40] Chen-yang Yan, You-peng Zhang, Wei-qing Xiong, Artificial Ant Colony Based on Grayscale Grads Perception on Digital Image Edge Detection, *Computer Engineering and Applications*, Vol. 42, No. 36, 2006, pp. 23-27.
[41] Yudong Zhang, Lenan Wu, Face Pose Estimation by Chaotic Artificial Bee Colony, *International Journal of Digital Content Technology and its Applications*. Vol. 5, No. 2, 2011, pp. 55-63.
[42] Alirezae Rezaee, Extracting Edge of Images with Ant Colony, Journal of Electrical Engineering, Vol. 59, No. 1, 2008, pp. 57-59.
[43] Peng Huang, Huizhi Cao, Shuqian Luo, A novel image segmentation algorithm based on artificial ant colonies, *Proceedings of 2nd International Conference on Medical Imaging and Informatics*, 2007, pp. 63-71.
[44] Chad George, James Wolfer, A swarm intelligence approach to counting stacked symmetric objects, *Proceedings of the IASTED International Conference on Artificial Intelligence and Applications*, AIA 2006, 2006, pp. 125-130.
[45] S. Aupetit, V. Bordeau, N. Monmarch´e, M. Slimane, G. Venturini, Interactive evolution of ant paintings, *2003 Congress on Evolutionary Computation Proceedings*IEEE Press, Vol. 2, 2003, pp. 1376–1383.
[46] Gary Greenfield, Ant Paintings using a Multiple Pheromone Model, *7th International Conference on Short and Medium Span Bridges 2006*, Montréal, Québec, Canada, August 23-25, 2006.
[47] Sambarta Dasgupta, Swagatam Das, Arijit Biswas, Abraham, Ajith, Automatic circle detection on digital images with an adaptive bacterial foraging algorithm, *Soft Computing*, Vol. 14, No. 11, 2010, pp. 1151-1164.
[48] Om Prakash Verma, Madasu Hanmandlu, Puneet Kumar, Sidharth Chhabra, Jindal, Akhil, A novel bacterial foraging technique for edge detection, *Pattern Recognition Letters*, Elsevier, Vol. 32, No. 8, 2011, pp. 1187-1196.
[49] Jianhua Yang, Guangyu Wang, Image edge detecting by using the bacteriorhodopsin-based artificial ganglion cell receptive field, *Thin Solid Films*, Vol. 324, No. 1-2, 1998, pp. 281-284.
[50] Dan Liu, Yu Zhao, Yan-Qiu Chen, Artificial Bacilli Model for Image Curve Extraction, *Computer Science*, Vol. 32, No. 5, 2005, pp. 190-194.

[51] Xiao-Li Chu, Ying Zhu, Jun-Tao Shi, Image Edge Detection Based on Improved Artificial Fish-School Swarm Algorithm, *Computer Systems & Application*, Vol. 19, No. 8, 2010, pp. 173-176.
[52] Hao He and Yan Qiu Chen, Artificial Life for Image Segmentation, *International journal of pattern recognition and artificial intelligence*, Vol. 15, No. 6, 2001, pp. 989-1003.
[53] Christine Bourjot, Vincent Chevrier, Vincent Thomas, How social spiders inspired an approach to region detection, *Proceedings of the International Conference on Autonomous Agents*, No. 2, 2002, pp. 426-433.
[54] Christine Bourjot, Vincent Chevrier, Vincent Thomas, A new swarm mechanism based on social spiders colonies: From web weaving to region detection, *Web Intelligence and Agent Systems*, Vol. 1, No. 1, 2003, pp. 47-64.
[55] Jeff Jones, Mohammed Saeed, Steve Lewis, Emergent computation and image processing - Feature extraction patterns generated by the interactions between simple agents and their image environment, *Proceedings of Middle Eastern Symposium on Modelling and Simulation*, 2003, pp. 5-7.
[56] Charles E. White II, Gene A. Tagliarini, Sridhar Narayan, An Algorithm for Swarm-based Color Image Segmentation, *Proceedings of IEEE SouthEast Conference*, 2004, pp. 84-89.
[57] Walther Fledelius, Brian H. Mayoh, A swarm based approach to medical image analysis, *Proceedings of the IASTED International Conference on Artificial Intelligence and Applications*, AIA 2006, 2006, pp. 150-155.
[58] R.F. Edgar, Generation and application of image transforms, *Optics Technology*, Vol. 1, Issue 4, 1969, pp. 183-190.
[59] Wang Min, Zhang Yanning, Sun Jinqiu, Li Ying, Ma Miao, A Method of Image Transform Based on Linear Elements, *Fifth International Conference on Image and Graphics*, 2009, pp. 124-128.
[60] R. Memisevic, G. Hinton, Unsupervised Learning of Image Transformations, Proceedings of *IEEE Conference on Computer Vision and Pattern Recognition*, 2007, pp. 1-8.
[61] Lennart Wietzke, Oliver Fleischmann, Gerald Sommer, 2D Image Analysis by Generalized Hilbert Transforms in Conformal Space, *Proceedings of the 10th European Conference on Computer Vision*: *Part II*, 2008, pp. 638-649.
[62] Shou-Cheng Hsiung, J. H. Jeng, Image retrieval based on fractal transformation, *WSEAS Transactions on Information Science and Applications*, Vol. 2, No. 7, 2005, pp. 827-834.
[63] T. Kowaliw, W. Banzhaf, N. Kharma, S. Harding, Evolving novel image features using genetic programming-based image transforms, *Proceedings of the IEEE Congress on Evolutionary Computation*, 2009, pp. 2502-2507.
[64] Claude Gasquet, Patrick Witomski, Fourier analysis and applications: filtering, numerical computation, wavelets, Springer, 1999.
[65] Lokenath Debnath, *Wavelet transforms and their applications*, Springer, 2002.
[66] S. Mallat, A theory for multi-resolution signal decomposition: The wavelet representation, *IEEE Pat. Anal. Mach. Intell.*, Vol. 11, No. 7, 1989, pp. 674-693.
[67] R.N. Bracewell, *The Fourier Transform and Its Applications* (Series in Electrical Engineering), McGraw-Hill Book Company, New York, 1986.
[68] Jaime Gomez, Carmen Morato, Teresa Castellanos, Juan Seijas, Two different approaches to classification applying appropriate wavelets, *WSEAS Transactions on Systems*, Vol. 4, No. 12, 2005, pp. 2369-2375.
[69] X. D. Zhuang and N. E. Mastorakis, The Curling Vector Field Transform of Gray-Scale Images: A Magneto-Static Inspired Approach, *WSEAS Transactions on Computers*, Vol. 7, Issue 3, 2008, pp. 147-153.
[70] G. Abdel-Hamid and Y. H. Yang, Multiscale Skeletonization: An electrostatic field-based approach, *Proceedings of IEEE International Conference on Image Processing*, Vol. 1, 1994, pp. 949-953.
[71] Andrew D. J. Cross and Edwin R. Hancock, Scale-space vector field for feature analysis, *Proceedings of the IEEE Computer Society Conference on Computer Vision and Pattern Recognition*, 1997, pp. 738-743.
[72] K. Wu and M. D. Levine, 3D part segmentation: A new physics-based approach, *IEEE International symposium on Computer Vision*, 1995, pp. 311-316.
[73] Xiao-Dong Zhuang, Nikos E. Mastorakis, A magneto-statics inspired transform for structure representation and analysis of digital images, *WSEAS Transactions on Computers*, Vol. 8, No. 5, 2009, pp. 874-883.
[74] X. D. Zhuang, N. E. Mastorakis, A novel field-source reverse transform for image structure representation and analysis, *WSEAS Transactions on Computers*, Vol. 8, No. 2, 2009, pp. 376-385.
[75] P. Hammond, *Electromagnetism for Engineers*: *An Introductory Course*, Oxford University Press, USA, forth edition, 1997.
[76] I. S. Grant and W. R. Phillips, *Electromagnetism*, John Wiley & Sons, second edition, 1990.
[77] Terence W. Barrett, *Topological foundations of electromagnetism*, World Scientific series in contemporary chemical physics, Vol. 26, World Scientific, 2008.
[78] Minoru Fujimoto, *Physics of classical electromagnetism*, Springer, 2007.

[79] Gustavo Carneiro, Allan D. Jepson, Flexible Spatial Configuration of Local Image Features, *IEEE Transactions on Pattern Analysis and Machine Intelligence*, Vol. 29, 2007, pp. 2089-2104.
[80] C. R. Shyu, C. E. Brodley, A. C. Kak, A. Kosaka, A. Aisen, L. Broderick, Local versus global features for content-based image retrieval, *IEEE Workshop on Content-Based Access of Image and Video Libraries*, 1998, pp. 30-34.
[81] Y. Shelepin, A. Harauzov, V. Chihman, S. Pronin, V. Fokin, N. Foreman, Incomplete image perception: Local features and global description, *International Journal of Psychophysiology*, Vol. 69, Issue 3, 2008, pp. 164.
[82] Aude Oliva, Antonio Torralba, Building the gist of a scene: the role of global image features in recognition, *Progress in brain research*, Vol. 155, 2006, pp. 23-36.
[83] Yuntao Qian, Rongchun Zhao, Image segmentation based on combination of the global and local information, *International Conference on Image Processing*, Vol. 1, 1997, pp. 204-207.
[84] Dimitri A. Lisin, Marwan A. Mattar, Matthew B. Blaschko, Erik G. Learned-Miller, Mark C. Benfield, Combining Local and Global Image Features for Object Class Recognition, *Proceedings of the 2005 IEEE Computer Society Conference on Computer Vision and Pattern Recognition*, Vol. 03, 2005, pp. 47.
[85] Takahiro Toyoda, Osamu Hasegawa, Random Field Model for Integration of Local Information and Global Information, *IEEE Transactions on Pattern Analysis and Machine Intelligence*, Vol. 30, 2008, pp. 1483-1489.
[86] J.A. Montoya-Zegarra, J. Beeck, N. Leite, R. Torres, A. Falcao, Combining Global with Local Texture Information for Image Retrieval Applications, *10th IEEE International Symposium on Multimedia*, 2008, pp. 148-153.
[87] M. Aly, P. Welinder, M. Munich, P. Perona, Automatic discovery of image families: Global vs. local features, *16th IEEE International Conference on Image Processing*, 2009, pp. 777-780.
[88] X. Zhuang, N. E. Mastorakis, The Local Fuzzy Fractal Dimension as a Feature of Local Complexity for Digital Images and Signals, *WSEAS transactions on Computers*, Vol. 4, Issue 11, November 2005, pp. 1459-1469.
[89] Michiharu Niimi, Hideki Noda and Eiji Kawaguchi, An image embedding in image by a complexity based region segmentation method, *Proceedings of 1997 International Conference on Image Processing*, Vol.3, 1997, pp. 74-77.
[90] Andrew B. Watson, Image Compression Using the Discrete Cosine Transform, *Mathematica Journal*, 4(1), 1994, pp. 81-88.
[91] Ahmed, N., T. Natarajan, and K. R. Rao, On image processing and a discrete cosine transform. *IEEE Transactions on Computers*, C-23(1), 1974, pp. 90-93.
[92] Wallace G., The JPEG still picture compression standard, *Communications of the ACM*, 34(4), 1991, pp. 30-44.
[93] Antonios Oikonomopoulos, Ioannis Patras, Maja Pantic, Spatiotemporal localization and categorization of human actions in unsegmented image sequences, *IEEE Transactions on Image Processing*, Vol. 20, No. 4, 2011, pp. 1126-1140.
[94] Kanglin Chen, Dirk A. Lorenz, Image sequence interpolation based on optical flow, segmentation, and optimal control, *IEEE Transactions on Image Processing*, Vol. 21, No. 3, 2012, pp. 1020-1030.
[95] Iulian Udroiu, Ioan Tache, Nicoleta Angelescu, Ion Caciula, Methods of measure and analyse of video quality of the image, *WSEAS Transactions on Signal Processing*, Vol. 5, No. 8, 2009, pp. 283-292.
[96] Radu Dobrescu, Matei Dobrescu, Dan Popescu, Parallel image and video processing on distributed computer systems, *WSEAS Transactions on Signal Processing*, Vol. 6, No. 3, 2010, pp. 123-132.
[97] Ingmar Lissner, Philipp Urban, Toward a unified color space for perception-based image processing, *IEEE Transactions on Image Processing*, Vol. 21, No. 3, 2012, pp. 1153-1168.
[98] David A. Kay, Alessandro Tomasi, Color image segmentation by the vector-valued allen-cahn phase-field model: A multigrid solution, *IEEE Transactions on Image Processing*, Vol. 18, No. 10, 2009, pp. 2330-2339.
[99] Zhengmao Ye, Habib Mohamadian, Yongmao Ye, Practical approaches on enhancement and segmentation of trimulus color image with information theory based quantitative measuring, *WSEAS Transactions on Signal Processing*, Vol. 4, No. 1, 2008, pp. 12-20.
[100] Keigo Hirakawa, Patrick J. Wolfe, Spatio-spectral color filter array design for optimal image recovery, *IEEE Transactions on Image Processing*, Vol. 17, No. 10, 2008, pp. 1876-1890.
[101] Athar Ali Moinuddin, Ekram Khan, Mohammed Ghanbari, Low complexity, efficient and embedded color image coding technique, *IEEE Transactions on Consumer Electronics*, Vol. 54, No. 2, 2008, pp. 787-794.
[102] Jae Young Choi, Yong Man Ro, Konstantinos N. Plataniotis, Color face recognition for degraded face images, *IEEE Transactions on Systems, Man, and Cybernetics, Part B*: *Cybernetics*, Vol. 39, No. 5, 2009, pp. 1217-1230.
[103] Saibabu Arigela, Vijayan K.A Asari, locally tuned nonlinear technique for color image enhancement, *WSEAS Transactions on Signal Processing*, Vol. 4, No. 8, 2008, pp. 514-519.

[104] P. A. Basford, P. M. Des, Algorithm to Compute the Eigenvalues/Functions of the Laplacian Operator with a Region Containing a Sharp Corner, *International Journal of Computer Mathematics*, Vol. 7, No. 4, 1979, pp. 339-350.
[105] Erhan Alparslan, Componentwise Edge Detection by Laplacian Operator Masks, *Signal Processing*, Vol. 2, No. 2, 1980, pp. 179-183.
[106] Fridrich Sloboda, Smooth and Sharp Laplacian Operators, *Computers and Artificial Intelligence*, Vol. 4, No. 2, 1985, pp. 153-162.
[107] Sonya A. Coleman, Bryan W. Scotney, Shanmugalingam Suganthan, Edge detecting for range data using laplacian operators, *IEEE Transactions on Image Processing*, Vol. 19, No. 11, 2010, pp. 2814-2824.

SUBJECT INDEX

Dr. Xiaodong Zhuang is Associate Professor at the Automation and Engineering College of Qingdao University (Qingdao, China).

He received his B.Sc. and M.Sc. from the Electronics and Engineering Department of Qingdao Ocean University (Qingdao, China) and His received his Ph.D. degree from the Computer Science Department of China Ocean University (Qingdao, China).

He is also a post-doctoral researcher under the supervision of Prof. Nikos E. Mastorakis and a researcher in the WSEAS Research Department (Greece). Also he has served as a visiting researcher in the Oceanic Remote Sensing Laboratory (ORSL) of the Chinese Education Ministry since 2006 and he served as a researcher in the "Professor Partnership Program" of Nvidia Corporation in 2010.

The research interest of Dr. Xiaodong Zhuang includes image segmentation and analysis, speech processing & recognition and parallel programming. He has been in charge of several research projects supported by WSEAS Research Department, Qingdao University, Nvidia Corporation and ORSL respectively. He has published more than 50 papers in journals and conferences and 3 books. He has served as a supervisor for master students of "Signal and Information Processing" in Qingdao University since 2006. He has been an active reviewer of several International Journals ("Artificial Intelligence in Medicine", Elsevier; "Journal of Qingdao University - Natural Science Edition"; "Computers in Biology and Medicine"; "Medical Engineering and Physics"; "Biomedical Signal Processing and Control" and "Neural Computing and Applications").

Prof. Dr. Nikos E. Mastorakis is Professor at the Technical University of Sofia, Bulgaria and also Professor at the Department of Computer Science at the Military Institutions of University Education (MIUE) - Hellenic Naval Academy, Greece.

He received his B.Sc. and M.Sc. in Electrical Engineering from the National Technical University of Athens, Greece and his Ph.D. in Electrical Engineering and Computer Science from the same university.

He also received his B.Sc. in Pure Mathematics from the National University of Athens, Greece. He served as special scientist on Computers and Electronics at the Hellenic Naval Academy and taught several courses in the Electrical and Computer Engineering Department of the National Technical University of Athens (1998-1994). He has also served as Visiting Professor at the University of Exeter, School of Engineering (UK, 1998) and visiting Professor at the Technical University of Sofia (Bulgaria, 2003-2004).

The Editor of over than 200 Books and the author of 5 books, Dr. Mastorakis has published more than 600 papers in international books, journals and conferences. An active reviewer of 26 International Journals and member of the Editorial Board of 13 International Journals and Editor of International Book Series, Member of the Editorial Board of "Advances in Computation: Theory and Practice" by NOVA), Dr. Mastorakis has received several awards for his academic studies and his scientific research. He is an active researcher in Applied Mathematics and Computer Science and he is the Editor-in-Chief in many International Journals. He has organized more than 30 International Conferences, 40 Special Sessions, 3 Workshops and has given many plenary lectures. He is also member of IEEE, New York Academy of Sciences, A.F. Communications & Electronics Association and member of the American Association for the Advancement of Science.

978-960-474-390-2